Master Thesis in Geographical Information Science nr 145

Mussels in deep water with climate change

Spatial distribution of mussel (*Mytilus galloprovincialis*) growth offshore in the French Mediterranean with respect to climate change scenario RCP 8.5 Long Term and Integrated Multi-Trophic Aquaculture (IMTA) using Dynamic Energy Budget (DEB) modelling

Victoria Persson

2022
Department of
Physical Geography and Ecosystem Science
Centre for Geographical Information Systems
Lund University
Sölvegatan 12
S-223 62 Lund
Sweden

Victoria Persson (2022). Mussels in deep water with climate change - Spatial distribution of mussel (*Mytilus galloprovincialis*) growth offshore in the French Mediterranean with respect to climate change scenario RCP 8.5 Long Term and Integrated Multi-Trophic Aquaculture (IMTA) using Dynamic Energy Budget (DEB) modelling
Master degree thesis, 30 credits in Master in Geographical Information Science (GIS)
Department of Physical Geography and Ecosystem Science, Lund University

Supervisors
Dr. Karin Hall
Professor at the Department of Physical Geography and Ecosystem Sciences
Lund University

Dr. Harry Lankreijer
Senior Lecturer at the Department of Physical Geography and Ecosystem Sciences
Lund University

Abstract

Mussel cultivation is a sustainable type of food production that may help mitigate the nutritional needs of a future world population of 10-12 billion in 2100. The demand for mussels on the French market is increasing but the production is saturated due to a lack of space for expanding the cultivation close to shore. This study looked at offshore possibilities for cultivating Mediterranean mussel *Mytilus galloprovincialis* to increase production. The Dynamic Energy Budget (DEB) theory was used in a Geographical Information System (GIS) to map out areas deeper than 30 m in the Mediterranean French Exclusive Economic Zone where temperature and food availability are suitable for mussel farming. The impact of future climate change scenario RCP 8.5 was investigated to estimate the sustainability of an offshore mussel farming operation in the French Mediterranean until the end of the 21st century. Since much of the Mediterranean is oligotrophic and food availability was suspected to be a limiting factor for growth, it was investigated whether waste from open pen fish farms would constitute enough mussel feed to sustain close-by mussel cultivation. The results indicated that the Gulf of Lion (GoL) was suitable for mussel farming every year 2011 - 2020 since the mean growth rate per mussel there ≥ 0.028 g / day, which is the estimated lower limit for mussel farming. The results also indicated that the eastern half of the GoL will experience less than optimal Sea Surface Temperatures (SSTs) in climate change scenario RCP 8.5 Long Term, leaving the western part of the GoL as the remaining sustainable option for mussel cultivation. Finally, the results indicated that incorporating mussel cultivation in an Integrated Multi-Tropic Aquaculture (IMTA) is a viable option in otherwise nutrient poor areas and will continue to be a viable option until at least the end of the 21st century, even in the event of climate change scenario RCP 8.5. The study is a first to use DEB-theory and GIS to map growth in the Mediterranean and for the Mediterranean mussel. It illustrates that DEB-modelling of growth over large areas is possible, which has major implications for aquaculture in general. It also emphasises the need of more research, notably regarding *i*) definition and calibration of DEB parameters for *M. galloprovincialis* in various environmental conditions and *ii*) acquirement of DEB parameter proxies to better adapt the DEB method to a GIS environment.

Résumé

La mytiliculture, ou la culture de moules, est un type de production de nourriture durable, et constitue un moyen de répondre aux besoins alimentaires d'une future population mondiale, qui devrait atteindre entre 10 et 12 milliards de personnes à la fin du siècle. La demande de moules sur le marché français augmente mais la production est saturée à cause d'un manque d'endroits près de la côte permettant d'étendre cette production. Cette étude considère les possibilités de cultiver la moule Méditerranéenne (*Mytilus galloprovincialis*) au large afin d'augmenter la production de moules en France. La théorie de Dynamic Energy Budget (DEB) est utilisée dans un Système d'Information Géographique (SIG) pour cartographier les régions de la zone économique exclusive (ZEE) de la France en Méditerranée, où les profondeurs excèdent 30 mètres et où la température ainsi que la disponibilité de la nourriture sont suffisantes pour soutenir l'élevage de moules. L'impact du changement climatique, selon le scénario RCP 8.5, est étudié pour estimer la durabilité d'une mytiliculture Méditerranéenne jusqu'à l'année 2100. Comme une grande partie de la Méditerranée est oligotrophe, nous

faisons l'hypothèse que la substance alimentaire est un facteur limitant pour la croissance des moules. Une enquête est ensuite réalisée pour élucider la capacité d'une pisciculture, c'est-à-dire une culture de poissons, à produire un apport de nutriments assez élevé pour soutenir une mytiliculture en sa proximité. Les résultats indiquent que le Golfe du Lion (GoL) est propice à la culture des moules pour chaque année sur la période 2011 - 2020. C'est-à-dire que la croissance moyenne par moule au GoL était ≥ 0,028 g / jour, ce qui est le minimum nécessaire estimé pour la culture des moules. Les résultats indiquent aussi que la moitié Est du GoL aura à partir de 2081 des températures de surface trop élevées pour être considérées optimales pour la culture des moules. A l'inverse, sur la moitié Ouest du GoL les températures de surface restent optimales jusqu'en 2100, ce qui en fait une zone géographique optimale et durable pour la culture des moules. Pour terminer, les résultats indiquent que cultiver des moules à proximité d'une pisciculture est une option viable. Dès à présent et jusqu'à la fin du 21ème siècle, qu'il sera selon les résultats possible de faire accroitre des moules dans des eaux qui ont sinon un taux en nutriments trop faible pour soutenir une croissance moyenne de 0,028 g / jour. Cette étude est la première à utiliser la théorie DEB dans un environnement SIG pour cartographier la croissance de la moule Méditerranéenne en Méditerranée. Elle montre qu'il est possible d'utiliser la théorie DEB pour modéliser la croissance des organismes sur des grands espaces, ce qui a des implications majeures pour l'aquaculture en générale. Des recherches complémentaires seraient bénéfiques, notamment concernant *i*) l'évaluation et la calibration des paramètres du modèle DEB pour *M. galloprovincialis* pour différentes conditions environnementales et *ii*) l'acquisition de proxys pour des paramètres du modèle DEB afin d'adapter la méthode à un environnement SIG.

Key Words

Geography, Geographical Information Systems, GIS, Physical Geography, Mediterranean, *Mytilus galloprovincialis*, Dynamic Energy Budget, DEB, growth rate, France, mussel cultivation, mussel farming, offshore, aquaculture, climate change, Integrated Multi-Trophic Aquaculture, IMTA.

Contents

Dictionary

Aquaculture	Farming of aquatic species
Bivalve	Aquatic mollusc with a shell that consists of two hinged parts
Detritus	Organic debris formed from the decay of organisms
Mariculture	Cultivation of saltwater species in seawater
Monoculture	Cultivation of one species independently of other cultivated species
Oligotrophic	Nutrient poor and clear waters
Phytoplankton	Drifting (and often microscopic) aquatic plants
Pisciculture	Fish farming
Polyculture	Cultivation of several species in proximity to one another

Abbreviations

C	Carbon
Chl *a*	Chlorophyll *a*
DEB	Dynamic Energy Budget
DOC	Detrital Organic Carbon
EEZ	Exclusive Economic Zone
GoL	Gulf of Lion
IFREMER	L'Institut Français de Recherche pour l'Exploitation de la Mer
J	Joules
IMTA	Integrated Multi-Trophic Aquaculture
N	Nitrogen
P	Phosphorus
POC	Particulate Organic Carbon
POM	Particulate Organic Matter
RINBIO	Le Réseau Intégrateurs Biologiques
RMSD	Root Mean Square Difference
SFG	Scope For Growth
SMCA	Spatial Multi Criteria Analysis

Figures

Tables

Equations

1. Introduction

The world's population will grow to be approximately 10.9 billion in 2100 (United Nations' Department of Economic and Social Affairs Population Division 2019) and global food supply will need to be adapted accordingly in an environmentally conscious manner (Godfray et al. 2010). Aquaculture is the farming of aquatic species and provides consumers with a reliable source of healthy (Institute of Medicine 2007), nutritious and affordable food that is available all months of the year (Rubino 2008). It offers expansion possibilities for the food industry without utilizing agricultural lands (Rubino 2011). Cultivating bivalves, such as mussels and oysters, has the additional advantage of having little impact on the environment it is cultivated in (Danovaro et al. 2004; FAO 2022). Although some environmental impact is present, such as faeces accumulating on the sea floor under the farms, the risk of increase in parasite populations, the use of boats and non-degradable net tubes used to thread mussels on cultivation lines (Tamburini et al. 2020), mussel cultivation inhibits major environmental advantages since it requires no direct input of food or chemicals (OSPAR 2009). Mussels need no antibiotics or fertilizers and bivalves counteract eutrophication by taking up phosphorus (P), nitrogen (N) and carbon (C) from the ocean (Bratt 2013). In addition, when farmed bivalves are of a native species and cultivated in suitable waters, the risk of introducing invasive species to an area is eliminated. There is generally less environmental impact from farmed molluscs than from alternative types of meat- or fish production, with regards to greenhouse gas emissions, land use, freshwater use and eutrophication potential per unit of protein (Tamburini et al. 2020; World Bank Data 2017).

Marine mussels are farmed in several countries around the world. Although the species vary, the farming methods remain similar in that they all provide a substrate for the mussels on which to grow in its natural environment. In India, the main species farmed are Green mussel (*Perna viridis*) and Brown mussel (*Perna indica*) (Department of Fisheries Government of Kerala 2021). A common farming method in the country is rack culture: growing the mussels on 1 meter long ropes that are tied to 25 m^2 racks kept upright by bamboo poles. Another type of farming is on-bottom culture, where the mussels are placed on the bottom of pens and left to grow until harvest. The Atlantic coast of France is known for its bouchot culture of the species *Mytilus edulis*, where the mussels are threaded on posts that are exposed to air at low tide but become submerged at high tide (FAO 2012). In Spain, the Galician Rìas are well known for their nutrient rich brackish waters, which are perfect for farming the blue mussel *Mytilus galloprovincialis* (FAO 2022). Mussels in the rìas are grown from rafts: floating wooden platforms of up to 500 m^2. From the rafts hang vertical lines on which the mussels are attached. Chilean farmers grow mussels of the species *Mytilus chilensis* on longlines, a contraption where major lines, 50-150 m long, are kept horizontally at the surface with buoys and held in place by anchors (FAO 2022). From each major line hang vertical lines for the mussels to grow on.

The importance of mussel cultivation varies as well. In many countries, such as China, mussel farming constitutes an important source of animal protein (FAO 2022). In India, it's a practice largely upheld by, and fundamental to, small-scale family enterprises (Parappurathu et al.

2021). In Sweden, research emphasise the environmental opportunities of mussel farming, not least as a means to counteract eutrophication (Haamer 1996; Lindahl et al. 2005; Kotta et al. 2020). With regards to expanding mussel production, France is a country of interest. The country is seeing an increase in its market demand for mussels (FAO 2020), an indication of which is the large difference between the country's import and export. France imported 45 000 metric tons of fresh mussels (*Mytilus spp.*) from other EU countries (notably Spain and the Netherlands) in 2018 and exported 3 390 metric tons the same year (mainly fresh mussels to Spain) (Chever et al. 2021). In addition, French mussels has a higher value on the European market, which is illustrated by their retail price (4.28 Euros / kg) being more than twice that of the same species cultivated in Italy or Spain (2.10 Euros / kg) (FAO 2021a). But the production's magnitude is stagnant since most of the country's mussel cultures are situated close to shore, where yields are saturated and farms cannot be expanded due to limited space (Prou and Goulletquer 2002).

According to the Food and Agriculture Organization of the United Nations, the only way to increase mussel production is to expand the production offshore (FAO 2021b). Whereas offshore energy production such as wind farms and oil platforms are functional and well established, offshore mussel cultivation is a younger field still in development. Open sea mussel farming is best conducted using longlines made for unprotected areas (Parappurathu et al. 2021; Cheney et al. 2010) but transitioning to offshore cultivation entail additional restraints such as higher hydrodynamic forces, concerns about environmental sustainability and spatial conflicts (Jansen et al. 2016; Troell et al. 2009). Farm structure parts may come loose in rough waters and constitute a threat to boats and wind turbines and offshore food production requires reliable and robust harvest methods, fully balanced flotation, effective infrastructure, avoidance of loss of mussels, low pollution, no excessive predation, low effect on birds and marine mammals, low biodiversity impact, and remote management. Production costs may also be higher offshore (OSPAR 2009).

Nonetheless, there are strong indications that the field has viability. Jansen et al. (2016) concludes that offshore aquaculture is feasible, and that mussel culture was the type of aquaculture that had the highest potential to be successful in the near future. Buck et al. (2010) confirmed the profitability of offshore suspended longline farms for mussels. Constructions that can withstand the offshore weather conditions and wave action are being developed, notably in the form of submerged longlines (Jansen et al. 2016). Other types of offshore aquaculture facilities (such as for fish farming) already exist and are constructed to withstand the forces of the oceans. For such farms, the risk of lost parts damaging other sea users exists but is small and the potential impacts insignificant when suitable anchorage is employed. Competition for space may open up opportunities for cooperation for mutual economic and ecological gains. OSPAR (2009) emphasized the potential for integrated offshore infrastructure incorporating wind turbines with longline mussel farms. Offshore sites tend to have more stable sea temperatures, better water exchange, less pollution and less risk of disease contamination than inshore sites, less user conflicts and less maintenance as the equipment is more robust (OSPAR 2009). In addition, growing mussels offshore may allow for more efficient feeding and faster growth (Ceccherelli and Rossi 1984; Barillé et al. 2020; Palmer et al. 2020).

Jansen et al. (2016) emphasized the need for governments and research institutes to act for the stimulation of further development of offshore mussel cultivation. More research is needed and finding areas suitable for offshore mussel production is crucial to the expansion of the sector (FAO 2021b). France has two major coastlines: the Atlantic coast, where *M. edulis* is farmed, and the Mediterranean coastline, where *M. galloprovincialis* is farmed. Several studies the last years have focused on offshore cultivation of bivalves in the Atlantic Ocean (Van der Veer et al. 2006; Barillé et al. 2020; Palmer et al. 2020). Much less is known about offshore mussel cultivation in the French Mediterranean Sea (Prou and Goulletquer 2002; FAO 2020), which includes the Gulf of Lion (GoL) in the northwest, the Corso-Ligurian Basin in the centre, the Ligurian Sea in the northeast and the Tyrrhenian Sea east of the Island of Corsica (Figure 1).

Figure 1: Map over the study area. The cities Marseille and Toulon are marked on the map since the former is the major city on the coast and a common land mark, and the latter marks the start of the French Riviera. The French Mediterranean mainland coast stretches from the Spanish border in the west and all the way to the Italian border in the east, with the coast between Toulon and Italy being the French Riviera. The island of Corsica is a single territorial collectivity in France, and as such it is a highly autonomous region. Its coastline is part of the French Mediterranean. The software used to create the map is ArcGIS Pro and the background map is from the United States Geological Survey (USGS) and provided by Esri.

M. galloprovincialis has been present in the Mediterranean for at least 18 000 years (Śmietanka et al. 2014) and fish farming was practiced here as early as in the Roman times (L. 2012). Although the Romans, in addition to consuming farmed fish, consumed oysters as well as mussels, the cultivation of bivalves in the Mediterranean likely evolved much later, in the 19th century, as a response to better transportation and new fishing techniques causing over-harvesting and vastly decreased wild populations (Bardot-Cambot and Forest 2013).

Today, onshore (i.e., in closed bays or close to shore) bivalve farming already exists in the area and several companies are in place. According to the French regional committee of bivalve farming in the Mediterranean (Comité Régional de la Conchyliculture de Méditerranée; CRCM), the cultivation of bivalves is actively ongoing in seven close to shore production zones along the French Mediterranean coast, out of which four, namely l'Etang de Diane, la Baie de Tamaris, l'Anse de Carteau, and La Pointe du Chichoulet, include the practice of mussel

farming (CRCM 2022) (Figure 2). Offshore oyster culture is present off the coast of Sète and in the Gruissan, and long line mussel farming at depths of up to 25 meters is present 30 minutes seawards off La Pointe du Chichoulet in the department of Aude.

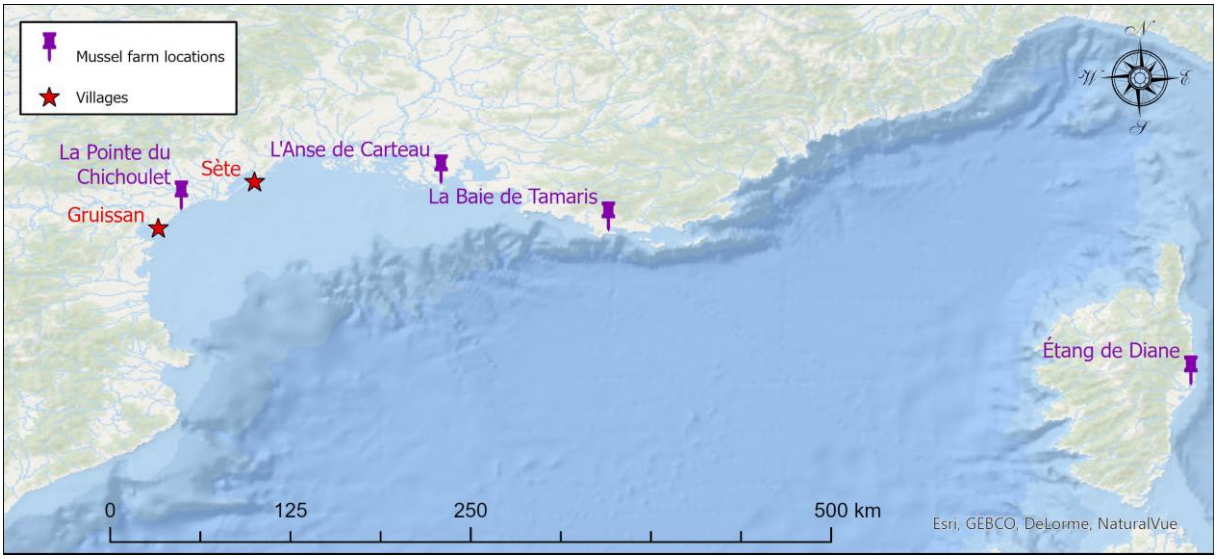

Figure 2: Mussel farm locations and locations of two villages important for oyster cultivation in the French Mediterranean Sea.

Most of the existing production areas are located in the GoL. The waters there are richer in nutrients compared to the open sea, mainly due to the shallow bathymetry which allows for stratification in the water column (Many et al. 2021). Stratification enables an overturn when density changes, which results in mixing of the sea water from the bottom to the surface. This overturn brings nutrients from deeper to shallower waters, where sunlight greets it and together, they create perfect conditions for primary production. Nutrients also enter the bay as runoff, notably from the Rhône River located slightly west of Marseille. East of GoL, along the French Riviera between Toulon and Italy, the ocean floor quickly falls to several hundred meters. Mixing of the water column and river runoff are not present is the same way as in the GoL and the waters are low in primary production.

The first and main question when planning to extend or develop mussel farming offshore is whether offshore conditions are adequate for mussel growth. According to Kooijman (2010), the theory of Dynamic Energy Budget (DEB) can be used to calculate mussel growth by applying species- and place specific parameters, and satellite data with Sea Surface Temperature (SST) and chl *a*, to the DEB equations. If an area is fit for mussel farming, then the mean growth rate of mussels is equal to or exceeds the growth rate needed to sustain mussel farming, i.e., for the mussels to grow fast enough for the production to be competitive on the European market. There are reasons to believe that to be the case since both temperature- and food availability are within the ranges required, at least in the GoL.

According to Jansen et al. (2009) and Anestis et al. (2010); The growth rate for *M. galloprovincialis* increases with surrounding water temperatures from 10.0 ˚C and up to at least 24 ˚C, a range that contains the Mediterranean median SST of 20 °C (Shaltout and Omstedt 2014). Regarding chl *a*, the Food and Agriculture Organisation (FAO) roughly estimates the

global minimum required for mussel cultivation to be 0.5 mg chl *a* / m^3 (FAO 2020). This would mean that parts of the French Mediterranean, notably the GoL, is composed of waters sufficiently nutritious for mussel cultivation. Hence, it may be hypothesized that offshore mussel growth will grow fast enough in the French Mediterranean waters that has the highest chl *a* levels.

Developing mussel farming to new areas require investments and need therefore be not only feasible but also sustainable, notably in the eye of climate change (Jansen et al. 2016). The Intergovernmental Panel on Climate Change (IPCC) scenario RCP 8.5 predicts that the median SST in the Mediterranean will increase to a maximum of 22.0 ˚C in the 21st century. The scenario induce thermal changes severe enough to necessitate investigation regarding their effects on mussel growth. If offshore cultivation of *M. galloprovincialis* in the French Mediterranean is sustainable, then climate change will result in unchanged or augmented mean and median mussel growth. There are reasons to believe that such cultivation is indeed sustainable since growth rate for *M. provincialis* increases within the span of climate change induced SST augmentation. The mean and median mussel growth in the French Mediterranean should hence increase with the predicted higher SSTs.

Most of the Mediterranean is oligotrophic. Therefore, some areas are likely to exhibit low potential mussel growth due to food scarcity. Nearby fish farms may provide food for mussels in a so called Integrated Multi-Trophic Aquaculture (IMTA) (Langan 2013). Additional beneficial synergy effects when combining several offshore activities include lower costs due to combined maintenance costs, logistics and use of space, and decreased ecosystem impact (Jansen et al. 2016). If the growth rate of mussels in an IMTA is equal to or exceeds the growth rate needed for the mussels to be farmed commercially, then a fish- and mussel based IMTA is a viable option for the French Mediterranean. Since chl *a* levels downstream from Mediterranean fish farms are known to exceed the FAO limit mentioned above (Modica et al. 2006) and since blue mussels are known to feed on waste from fish farms (Macdonald et al. 2011; Mazzola and Sarà 2001), it is a reasonable assumption that piscicultures may provide enough mussel food to sustain a nearby farm.

The objective of this study is to investigate whether mussel cultivation in offshore Mediterranean French waters is *i*) feasible and *ii*) sustainable in the eye of climate change over the present century, as well as *iii*) whether *M. galloprovincialis* can be farmed in proximity to a fish farm to substitute for otherwise nutrient poor waters. The questions are analysed in a Geographical Information System (GIS) and its use in GIS environments evaluated. The resulting insights in the future for offshore mussel cultivation are meant to be used as a basis for political decisions and investments within the aquaculture sector.

2. Background

2.1. Mytilus galloprovincialis

As the name inclines, the Mediterranean mussel (*M. galloprovincialis*) (seen in Figure 3) is native to the Mediterranean and cultured around its borders in Tunisia, Algeria, Morocco, Spain, France, Italy, the Balkan, Greece, Bulgaria and Turkey (FAO 2021b). The species is also cultured outside of the Mediterranean on the Atlantic coast of Spain as well as in Ukraine, Russia, South Africa and China, which is the largest producer.

Figure 3: Mussels of species Mytilus galloprovincialis. Photograph provided by the French mussel farming company Les Viviers de Carteau.

The species is a type of blue mussel (Prou and Goulletquer 2002), similar and closely related to *M. edulis* but withstands higher temperatures better (Gosling 1984; Śmietanka et al. 2014). Laboratory experiments has shown that the respiration rate for *M. galloprovincialis* increases with surrounding water temperatures from 10 ˚C to 27 ˚C, followed by a drastic drop in respiration rate until no respiration is observed at temperatures above 31 ˚C (Jansen et al. 2009). Further experiments has shown that the species' Scope For Growth (SFG) increases when surrounding water temperatures increased form 18 ˚C to 24 ˚C, followed by a decrease in SGF for surrounding temperatures of 26 ˚C and 28 ˚C (Anestis et al. 2010). The critical heart rate temperature (above which cardiac function collapses) for the species has been shown to be 27 ˚C for mussels acclimated to a surrounding water temperature of 14 ˚C, and 31 ˚C for mussels acclimated to 21 ˚C (Lockwood and Somero 2011). Mortality due to high temperature in *M. galloprovincialis* has been shown to be close to zero in surrounding temperatures of less than 26 ˚C, followed by an increase in mortality up to 30 ˚C, where 80 % of the mussels died within 15 days (Anestis et al. 2007).

The mussel starts its life cycle as pelagic larvae that settles when it finds an appropriate area (Cattaneo-Vietti et al. 2016). Once settled, the larvae metamorphoses into a small mussel and developpes byssus threads with which the mussel can attach to a hard substrate and withstands the increasing impact from currents as the mussel grows.

Mussels are filter feeders, primarily targeting phytoplankton in the water column but also capable of eating other types of organic matter such as detritus (Mazzola and Sarà 2001; Bearham et al. 2020; Willer and Aldridge 2017). Both living (e.g., phytoplankton) and non-living (detritus) organic matter that are not dissolved (exact size definitions vary depending on study and is often dependent on the type of filter used for analysis) in the sea water make up its Particulate Organic Matter (POM). A common way of measuring POM is in Particulate Organic

Carbon (POC), which translates to the mass weight of carbon in POM. A common way of quantifying phytoplankton is to translate it to its chlorophyll *a* (chl *a*) contents since chl *a* is fast and easy to measure either in situ with a chlorophyll meter or remotely by satellite. Detritus can be quantified using Detrital Organic Carbon (DOC), which is the difference between POC and live carbon and can be approximated to the difference between POC and chl *a* (Ribes et al. 1999).

Detritus in the Mediterranean Sea originates mainly from rivers, notably Rhône (Higueras et al. 2014) but also from other parts of land, from primary production in the sea, and from waste from animals such as fish and marine mammals. Although POC may be transported faster horizontally than laterally (Alonso-González et al. 2009), the detritus will eventually fall to the bottom in the absence of mixing of the water column. Therefore, and as shown by Bearham et al. (2020), detritus is likely to be a more important food source for mussels close to shore (where it is available) rather than offshore, where the mussels become dependent on phytoplankton.

Whereas river runoff brings nutrients for plankton to grow and feed mussel populations, the large amount of inorganic debris likely hinders efficient feeding. Ceccherelli and Rossi (1984) investigated abundance, growth, survival and production of *M. galloprovincialis* on the Adriatic coast in Italy over three years (1977-179) and found that, while growth and production benefited from abundant food, inorganic debris decreased the mussels' capacity to take up nutrients and caused heavy mortality. Sarà et al. (1998) studied mussels (*M. galloprovincialis*) placed in nets suspended at depths between 5 and 15 meters in the in the open waters of the southern Mediterranean Sea and found that, when the inorganic matter in food particles increased, the mussels compensated by adapting their filtering behaviour to maintain a constant absorption rate of organic matter. Barillé et al. (2020) assessed the feasibility of offshore production of oysters at two spots in Bourgneuf Bay on the French Atlantic coast and found the bivalves to grow significantly faster offshore compared to in an intertidal area, in terms of both length and weight. Palmer et al. (2020) used remote sensing to model oyster growth in Bourgneuf Bay and found offshore growth to be up to twice as fast compared to intertidal growth. Both authors concluded that the more important offshore growth was likely due to lower concentrations of inorganic particulate matter, which allows for more efficient filter feeding. It is reasonable to believe that, since mussels prefer smaller particles, such an adaptation would increase the cost of filtration and decrease digestion efficiency.

2.2. Mussel Farming

Cultivating mussels starts with obtaining young individuals, called spat (Cattaneo-Vietti et al. 2016). Spat can either be harvested from the sea bottom, reared in tanks or collected by deploying lines in the sea that the mussel larvae settle on. In the Mediterranean, *M. galloprovincialis* spat is collected from rocky shores or shallow harbours (Barnabé and Doumenge 2001). A type of net tubes, or socks, are used to attach the spat to lines in a procedure called seeding. The lines are set out in the water for the spat to grow and kept close to the surface with a system of floating buoys (Figure 4). Once the mussels develop byssus threads and attach themselves to the lines, the net tubes are no longer needed and eventually disintegrates partially to give the mussels more space to grow.

Figure 4: Close to shore cultivation of M. galloprovincialis in the French Mediterranean. Photograph provided by the non-profit organization Cépralmar (www.cepralmar.org).

When the mussels have reached a length of 4-5cm (normally after 5-6 months), a procedure called thinning is often undertaken to avoid clumping of mussels and to ensure an even mussel size (FAO 2021b). Mussels that clump together are more at risk of falling off the cultivation lines when exposed to rough weather. In addition, allowing the mussels to grow evenly facilitates harvest since more mussels are ready for harvest at the same time. When thinning, the mussel farmers separate the mussels from the lines, sort them by size and reseed them in new socks. Thinning is repeated when needed until the mussels reach a market size of 8-10 cm in length and are harvested. When growth is rapid, the mussels obtain their market size 3 months after thinning but it is common for growth to be slower and for the mussels stay submerged for up to 8 months after thinning.

2.3. Spatial Multi-Criteria Evaluation (SMCA)

Offshore as well as close to shore, site selection is a critical initial step when initiating mussel farming since bivalve growth can vary greatly depending on site characteristics (Bratt 2013; Palmer et al. 2020). Site selection modelling is an efficient tool to narrow down a testing area to the most suited sites (Tammi and Kalliola 2014). Spatial multi-criteria evaluation (SMCA) is a site selection modelling commonly used for aquaculture and coastal management (Barillé et al. 2020). It is an efficient method, but its results are highly dependent on the quality of the input data and the importance weighting of the data sets (Tammi and Kalliola 2014). A type of site selection model that requires less subjective input is species distribution models (SDMs) (Falconer et al. 2016). Whereas SMCA methods use the scientific literature and stakeholder opinions to choose input data, SDM methods examine the conditions at existing farm sites and use the resulting parameters to extrapolate potential sites elsewhere. The latter method is thus

dependent on the number and dispersion of existing farm sites for their results. In areas with a high number of study sites with similar characteristics, such as the study of shrimp cultivation in Vietnam by Falconer et al. (2016), SDMs can be a preferable model. Indeed, although the study concluded that both SDMs and SMCAs are fit for modelling suitable aquaculture sites, the authors recommended a SDM approach for similar research projects. However, the authors had useable data from almost 200 farms in proximity and with very similar characteristics to their disposal. In situations where the available sample sites are few and/or their area characteristics varied, such as offshore in the French Mediterranean, a SMCA approach is preferrable.

2.4. Dynamic Energy Budget (DEB)

A typical SMCA model is based on social, environmental, and biological (i.e., growth) constraints. Mussel growth is the most fundamental constraint since aquaculture can only be conducted where conditions are favourable for the growth of the cultivated species. Food availability (Ceccherelli and Rossi 1984; Page and Hubbard 1987; Sarà et al. 1998; Filgueira et al. 2011) and ambient temperature (Anestis et al. 2007; Sarà et al. 2011a; Montalto et al. 2017; Lockwood and Somero 2011; Kroeker et al. 2014; Keskin et al. 2020; Jansen et al. 2009) are drivers for mussel growth. Dynamic Energy Budget (DEB) is a method used to test the potential growth of organisms based on surrounding food availability and temperature. It was first described by Kooijman (1986), updated and ameliorated for decades and republished in 2010 (Kooijman 2010).

Several studies have successfully used the method to model bivalve growth. Van Haren and Kooijman (1993) successfully described growth, among other parameters, of *M. edulis* by applying DEB parameters from laboratory measurements on field situations and comparing the results with field data. Casas and Bacher (2006) modelled blue mussel (*M. galloprovincialis*) growth in two bays and by one island on the French Mediterranean shoreline and obtained results that corresponded well with in situ measurements. Rosland et al. (2009) used the DEB model to simulate growth for *M. edulis* in Norwegian waters and obtained results that corresponded well with in situ observations. Filgueira et al. (2011) compared two methods to estimate growth, namely the DEB model and Scope For Growth (SFG) and found both able to successfully reproduce mussel (*M. edulis*) growth. Handa et al. (2011) modelled the growth of *M. edulis* of the coast of Norway using DEB theory and found good coherence between modelled and observed growth in two out of three mussel farms. Alunno-Bruscia et al. (2011) successfully modelled growth for both spat and adult stages of oyster *Crassostrea gigas* over time and at several different sites. Larsen et al. (2014) compared in situ growth of *M. edulis* with growth modelled using DEB, SFG and bioenergetic growth model, and found that the DEB model produced the best predictions. Other examples include Van der Veer et al. (2006), Troost et al. (2010), Saraiva et al. (2012), Hatzonikolakis et al. (2017), Palmer et al. (2020) and Fuentes-Santos et al. (2021). In addition, the Institute for Health and Consumer Protection at the European Commission Joint Research Centre, as well as the French State authorities, apply DEB theory and *M. galloprovincialis* growth, among other parameters, to predict and monitor the concentration of contaminants such as heavy metals in the water column (Zaldívar 2008).

The DEB method is designed to be species-specific as well as site-specific but not all parameters exist for all species, sometimes forcing researchers to use approximate values. Casas and Bacher (2006) modelled the growth of *M. galloprovincialis* but used some parameters for *M. edulis* due to a contemporary lack of species-specific parameters for *M. galloprovincialis*. The authors concluded that their model could benefit from validation with parameters specific to *M. galloprovincialis*. A decade later, Hatzonikolakis et al. (2017) calibrated and validated new DEB parameters specific for *M. galloprovincialis*. The study was conducted in the Aegean Sea, which is separated from French Mediterranean waters by the two peninsulas Italy and Greece. The two sea areas are hence geographically separate from each other and cannot be considered the same site.

To the knowledge of the author, no study so far has used species- and site-specific parameters in the DEB method to model potential sites for offshore farming of *M. galloprovincialis* in the French Mediterranean Sea. Using site-specific temperature and chlorophyll values for the French Mediterranean, as well as the species-specific parameters from Hatzonikolakis et al. (2017) for *M. galloprovincialis*, should give better results than using parameters specific for *M. edulis*, as was done by Casas and Bacher (2006). In addition, whereas several studies have investigated mussel growth at a small number of spots, there is a lack of research that investigate the mussel growth potential of a large continuous area. Geographical Information Systems (GIS) is a set of tools suitable for such analyses.

2.5. Climate Change

The stability and credibility of environmental research increases when potential effects of climate change are included. The importance of including effects of climate change in aquaculture planning is emphasised by the General Fisheries Commission for the Mediterranean, in their aim "to assess the vulnerability of aquaculture to climate change and to map risks" (FAO 2018).

The 2021 Sixth Assessment Report from IPCC states that the mean global SST in 2010-2019 have increased about 0.8 ˚C compared to the average in 1850-1900 and that SST is likely to continue to increase for the rest of this century (IPCC 2021b). The report describes five likely future scenarios, or Shared Socioeconomic Pathways (SSPs), that the world may take for the rest of this century: SSP5-8.5 is a scenario where GHG emissions are very high and CO2 emissions will double by 2050, scenario SSP3-7.0 have high GHG emissions and CO2 doubles by 2100, SSP2-4.5 have intermediate GHG emissions and CO2 that remain constant until 2050, for SSP1-2.6 the GHG emissions are low and CO2 decline to zero after 2050 to subsequently fall to negative values, and finally SSP1-1.9 where GHG emissions are very low and CO2 decline to zero around 2050 whereafter negative values follow.

The SSPs describe the broad socioeconomic trends that are predicted to lead to certain levels of greenhouse gases and other types of radiative forcing that may impact global climate (for example volcanic eruptions). Representative Concentration Pathways (RCPs) describe similar scenarios but without including any socioeconomic factors. The two are related and complement each other but whereas SSPs are useful to plan for climate change mitigation,

RCPs are useful to describe what a certain scenario entails for the environment. There are four RCP scenarios: RCP 2.6, RCP 4.5, RCP 6.0 and RCP 8.5, representing a global mean radiative forcing of 2.6, 4.5, 6.0 and 8.5 W/m^2, respectively, at the end of the 21st century (IPCC 2021b).

Regional predictions of SST in the Mediterranean for RCP 4.5 and RCP 8.5 are based on the CORDEX Mediterranean dataset and available online via the IPCC WGI Interactive Atlas, a supporting tool to the Assessment Report (IPCC 2021a). According to IPCC scenario RCP 4.5, the Mediterranean SST is predicted to increase with a median of 0.8 ˚C in the near term (2021-2040), 1.3 ˚C in the medium term (2041-2060) and 1.9 ˚C in the long term (2081-2100), resulting in median temperatures of 19.7 ˚C, 20.1 ˚C and 20.8 ˚C, respectively. Scenario RCP 8.5 predicts the SST increase to be 0.8 ˚C in the near term, 1.3 ˚C in the medium term and 3 ˚C in the long term), resulting in median temperatures of 19.8 ˚C, 20.4 ˚C and 22.0 ˚C, respectively.

The distribution of SST change is uneven over the territory, an issue accounted for when utilising rasters rather than spatial averages. Rasters can be thought of as grids where each square in the grid constitutes a cell that can be filled with data, such as a number or text. For SST rasters, the SST is the data that fills the raster, with one SST per cell. The SST in question may be an estimated mean for the cell or an SST that has been measured at a point located somewhere within the cell. In that way, a raster is a good way of presenting the change of SST over an area. By using several rasters, where each raster represents a specific period of time (such as a day or a month), is it possible to also analyse and visualise evolution over time.

To the knowledge of the author, there are currently no openly available raster data predicting spatial and temporal distribution or levels of chl *a* for RCP 8.5 Long Term in the French Mediterranean. Therefore, the DEB model was not used to model prospective growth rates in the climate change scenario. Instead, chl *a* and SST were investigated individually and an assessment of area suitability for mussel cultivation conducted based on the combined results.

2.5.1. SST

For the mussels to grow fast enough to be farmable, the number of days that the temperatures are within the optimal, less than optimal, and deadly ranges for SST is highly relevant. The DEB model does not take into account that the mussel's life sustaining systems cannot withstand temperatures above 31 °C, at which time the mussel dies. Therefore, temperatures above said threshold need to be mapped separately and areas concerned excluded from potential farming sites. Where the SST doesn't kill the mussels, higher temperatures may decrease the mussel's growth rate and cause losses of cultivatable areas in that way.

2.5.2. Chl a

According to Macias et al. (2015), chl a is likely to decrease in the West Mediterranean and increase in the East Mediterranean at the end of this century. The study area is in the West Mediterranean. However, the decrease is strongest in the southern part of the West Mediterranean, close to the Gibraltar Straight, whereas there is little to no evidence of chl *a* levels changing at all in French waters, which are located in the northern parts of the West Mediterranean.

2.6. Integrated Multi-Trophic Aquaculture (IMTA)

The other environmental variable used in this study is primary production. Macias et al. (2015) analysed the primary production in the Mediterranean and its evolution in four different climate change simulations based on IPCC scenarios RCP 4.5 and RCP 8.5. They concluded that, for RCP 8.5, chl *a* is likely to decrease in the West Mediterranean and increase in the East Mediterranean at the end of this century. The study area is in the West Mediterranean. However, the decrease is strongest in the southern part of the West Mediterranean, close to the Gibraltar Straight, whereas there is little to no evidence of mean chl *a* levels changing at all in French waters, which are located in the northern parts of the West Mediterranean. Further studies that analyse the impact of climate change on primary production in the Mediterranean are expected but currently lacking. However, the analysis made by Macias et al. (2015) was in depth and through. Hence, based on the indications available in scientific literature, there is no support to consider primary production a factor dependent on climate change in the study area for the 21st century.

Nevertheless, primary production remains a topic of interest. Since the Mediterranean is oligotrophic, mussels grown offshore risk having their growth limited by food supply. The chl *a* levels in the study area are often as low as 0.02 mg / m^3 (Figure 13), to be compared to the 0.5 mg / m^3 that is recommended by the United Nations Food and Agriculture Organization (FAO). Offshore cultures also do not have access to the same POC levels as onshore cultures have. Therefore, access to food may limit growth offshore.

Although feed pellets are an alternative to enable mussel farming in areas that are not inherently nutrient rich enough to sustain mussel growth (Willer and Aldridge 2017), this approach is not recommended since it would eliminate one of the major arguments for mussel cultivation as an environmentally friendly means of food production, namely the absence of additives.

However, Integrated Multi-Trophic Aquaculture (IMTA) is a possible solution. In an IMTA, several species are farmed together to either increase production, mitigate environmental impact, or both (Troell et al. 2009). A combination of two or more types of species are commonly used: high trophic species such as fish or shrimp, filter feeders such as bivalves, and detritus eaters such as sea cucumbers. The excess feed and faeces from the high trophic species are distributed to the surrounding water as dissolved nutrients or suspended POC. Algae feed off the nutrients and are subsequently eaten by the filter feeders, that also feed off the POC. Detritus from high trophic species and filter feeders fall to the bottom and are taken care of by detritus eaters.

Peharda et al. (2007) demonstrated that areas not optimal for mussel farming can sustain mussel cultivation if integrated with finfish aquaculture. Modica et al. (2006) analysed the chl *a* carbon (chl *a* C) levels 1000 meters downstream from a Mediterranean fish farm and found an average of 28.9 mg C / m^3 (31.8 mg C / m^3 in spring and 26 mg C / m^3 in summer), to be compared with an average of 0.5 mg C / m^3 upstream from the same fish farm. Assuming a chl *a* : C ratio of 50 (Hatzonikolakis et al. 2017), this translates to 0.578 mg chl *a* / m^3 downstream form the fish farm, which is above the FAO limit of 0.5 mg chl *a* / m^3.

Several studies have shown the capability of blue mussels to use pisciculture waste as a food source. Mazzola and Sarà (2001) used stable carbon isotope analysis to show that mussels eat food and faeces discarded from nearby fish farms. Macdonald et al. (2011) showed that blue mussels (*M. edulis*) are capable of capturing and absorbing salmon fish food. Willer and Aldridge (2017) used Micro-CT images of microparticles in mussel guts to demonstrate that blue mussels filter out and digest microalgal pellets of sizes up to 150 µm in length from the surrounding water. Montalto et al. (2017) studied ingestion rates and assimilation efficiencies of *M. galloprovincialis* when fed three different diets (i.e., seagrass, phytoplankton and pellets) in a controlled laboratory environment and found positive mussel growth for all three diets.

The mussels also seem to grow better. Handa et al. (2012) showed that *M. edulis* grows faster and maintains a higher tissue content during winter when placed closer to a salmon culture. Troell et al. (2009) studied Atlantic salmon, kelps and blue mussels (*Mytilus edulis*) that were reared together at several IMTA sites in the Bay of Fundy on the east coast of Canada. The authors reported that growth rates of kelps and mussels cultured in proximity to fish farms have been 46 % and 50 % higher, respectively, than at control sites. Peharda et al. (2007) studied growth of mussels at 0 m, 60 m and 700 m distance from a finfish aquaculture in the eastern Adriatic Sea and found that the mussels grew best at 60 m from the pisciculture (mean growth 23.46 mm compared to 18.26 mm at 0 m and 19.24 mm at 700 m). Sarà et al. (2009) found that mussels (*M. galloprovincialis*) cultivated at an impact site close to fin fish farm cages in the south Tyrrhenian Sea (close to Sicily) grew more in both length and weight compared to mussels farmed at a control site far from the pisciculture sites.

There are positive environental aspects with farming mussels close to a marine pisciculture. As concluded by Dauda et al. (2019), it is important to develop efficient waste management for pisciculture so that the environmental impact is minimised, not least in face of increased pisciculture worldwide. Pisciculture increases N, P and chl *a* at a small scale (Mazzola and Sarà 2001) as well as large scale, as seen by Sarà et al. (2011b) when analysing longterm trends in N, P and chl *a* with respect to the presence of pisciculture in the Southern Tyrrehnian Sea. Mussel cultivations help mitigate that environmental impact (Dauda et al. 2019).

Finally, mussel farming as a part of IMTA has the potential to increase profits for existing aquaculturers. Approximately 2500 tonnes of fish, mainly bass, bream and meagre (FAO 2012), are produced in the French Mediteranean marine pisciculture each year (Préfecture de la région Provence-Alpes-Côte d'Azur 2015; French Ministry of Ecology 2013). According to Dauda et al. (2020), a ton of fish generates an average of 0.8 kg of nitrogen and 0.1 kg of phosphorus. For 2500 tonnes of fish, that would mean 2000 kg N and 250 kg P. Mazzola and Sarà (2001) found an average weight ratio between C and N in the water of the piscicultures they studied to be 23. If we assume that to be the average for French Mediterranean pisciculture, then that would mean a C content of 46 000 kg. No record is found of the N, P or C contents in *M. galloprovincialis* but Arnott and Vanni (1996) analyzed the concentration of the three in zebra mussels and found that the mussel body (shell and tissue) is comprised by approximately 0.05 % P, 1 % N and 14 % C. If we assume a similar composition in *M. galloprovincialis*, then the waste from 2500 tonnes of fish containts enough P to produce 500 tonnes mussels, enough N

to produce 200 tonnes mussels and enough C to produce ca 329 tonnes mussels. The N is thus the limiting factor and the potential mussel production from the waste of 2500 tonnes of fish is 200 tonnes, to be compared to the 8000 to 10 000 tonnes that is produced in the Mediterranean anually (French Ministry of Ecology 2013).

The consumer pays 4.28 Euros per kg (FAO 2021a) and the profit is about 25 % of that (FAO 2021b). Hence 200 tonnes of mussels sell for ca 856 000 Euros, of which 214 000 Euros is producer profit.

3. Methods

3.1. The DEB method

3.1.1. Background and theory

The DEB method was introduced by Kooijman (1986) and explained in detail in (Kooijman 2010). It is a theory and a mathematical model that describes the growth of organisms. The theory states that energy enters the organism via food (Figure 5). Part of the energy is allocated to the organism's soma structure, which is composed by all cells that are not reproductive cells, and the rest of the energy is directed to the reproductive system. The energy in respective compartment is used primarily to maintain the existing structures and the rest of the energy is used for growth and reproduction.

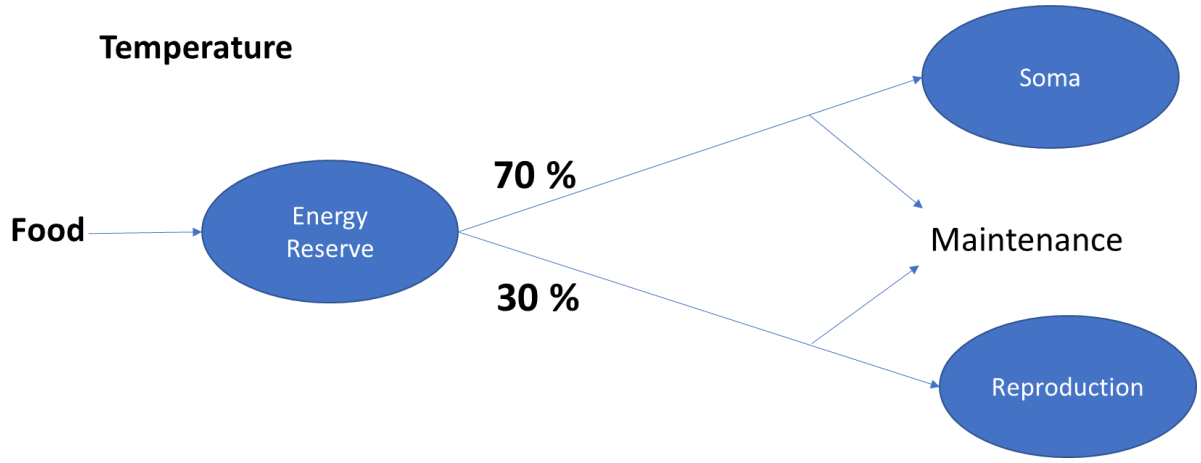

Figure 5: Illustration of the fundamental concepts in DEB theory. Energy enters an organism as food and is stored in an energy reserve. From there, 70 % of the energy is allocated to the soma and 30 % to the reproductive system. The energy for each entity is first used for maintenance and remaining energy is used for growth.

The DEB calculations are based on the initial volume of the organism's soma (V), its initial energy reserves (E), its initial energy for maintenance and reproduction (R), food availability (X), a food uptake constant (X_k), the surrounding temperature (T), the percentage of E used for reproductive purposes (1-κ), and the remaining percentage used for maintenance and growth of the soma (κ).

The method is valid for all organisms but particularly useful for animals since their energy intake is easier to calculate. A number of parameters (some not mentioned above), such as κ, volume specific maintenance costs and energy content of reserves, are species-specific and necessary for growth calculations. Van der Veer et al. (2006) measured several of those parameters for *M. edulis*. The parameters were tested for *M. galloprovincialis* and additional parameters, such as X_k, were defined for the French Mediterranean by Casas and Bacher (2006). All parameters were tested, and two parameters (E and R) previously calibrated for *M. edulis* were recalibrated for *M. galloprovincialis* by Hatzonikolakis et al. (2017).

The remaining undefined parameters vital to this study are V, X and T. Two different V can be used for model calculations: one for juvenile individuals (V_p) and one for mature ones (V_{min}). In the present study, only mature individuals are considered and their soma volume is referred

to as V. X is translatable to the amount of phytoplankton carbon (Phyto-C) present in the water, a measure derived from the proxy chlorophyll *a*. Parameter T in this case is SST since offshore farmed mussels are constantly submerged in waters from the surface and down.

3.1.2. Initial Mussel Weight

According to the DEB-model, the weight (W) in grams (g) of a mussel can be estimated from its soma volume (V) in centimetres (cm) according to Equation 1 below.

$$W = d * \left(V + \frac{E}{[E_G]}\right) + \frac{R}{\mu_E}$$

Equation 1: Mussel weight

Where E is the energy content of the energy reserve and given in Joules (J), R is the energy content of the reproductive organs and also had the unit J, d is specific density and has a value of 1.0 g / cm^3 (Kooijman 2010), $[E_G]$ is the volume specific cost of growth and has a value of 1900 J / cm^3 (Van der Veer et al. 2006), and μ_E is the energy content of reserves and has a value of 6750 J / g (Casas and Bacher 2006). E and R can be estimated from V according to Equation 2 and Equation 3 below (Hatzonikolakis et al. 2017).

$$E = \frac{V}{cm^3} * 300 * 0.7\,J$$

Equation 2: Energy reserve

$$R = \frac{V}{cm^3} * 300 * 0.3\,J$$

Equation 3: Energy content of reproductive organs

Another DEB-equation (Equation 4) converts mussel length (L) in cm to its V in cm^3 and vice versa using a shape coefficient (δ_m), which does not have a unit.

$$L = \frac{V^{1/3}}{\delta_m} \rightarrow V = (L * \delta_m)^3$$

Equation 4: Length to Volume

Several values for δ_m have been proposed in scientific literature. Van Haren and Kooijman (1993) found a δ_m for *M. edulis* of 0.333 with a standard deviation of 0.097 by analysing Wadden Sea mussel data from Borchardt (1985) and Pieters et al. (1979). Van der Veer et al. (2006) proposed a δ_m of 0.287 ± 0.090 for *M. edulis* based on the author's field- and laboratory data from the western Dutch Wadden Sea. Casas and Bacher (2006) used four data sets of *M. galloprovincialis* from the French Mediterranean as well as an algorithm based on the simplex method to calibrate δ_m and found 0.250 to be the best fit. The present study used the value 0.250 for δ_m since it was calibrated using *M. galloprovincialis* at French Mediterranean sites whereas other values for δ_m were found using *M. edulis*. However, the unused values of δ_m have the benefit of having been obtained from mussel measurements rather than from data calibration and it can therefore be argued that they are to be considered more correct. To assess the impact

of the different values for δ_m, they are included in the sensitivity analysis discussed in a later section.

Initial mussel weight for the present study was calculated based on an initial mussel length of 5.0 cm. This length was used for two reasons. First, it is the initial length of the mussels used in the model validation. The DEB model is complicated to apply to mussels at different maturity levels (i.e., juvenile vs. adult) in a GIS environment. One model is needed for juveniles and a completely different model is necessary for adults. Whereas it would be interesting to model all the mussels' life stages, it is not within the scope of the present study due to limitations in in situ observations for mussels smaller than 5.0 cm. Modelling mussels of a smaller size would thus imply uncertainty regarding the model accuracy or, alternatively, require several months work of field work that are not applicable to the study time frame.

Second, 4-5 cm is the length the mussels usually have when mussel farmers thin the mussel cultivation ropes, which is the procedure of reattaching the mussels to the ropes for the last time before harvest a few months later (FAO 2021b). It is about half the length of the full-grown mussel and a good initial length for predicting post-thinning mussel growth offshore. The estimated growth rate is then to be compared only with the required post-thinning growth rate. Since the growth rate is specific to post-thinning, and since adequate post-thinning growth rates accompany adequate pre-thinning growth rates in e.g., Galicia (FAO 2021b), it is assumed that a sufficient growth rate between thinning and harvest is equally an indication of sufficient growth rate between seeding and thinning, and that mussel farming is suitable where post-thinning growth rates are high enough.

This leads us to conclude that a mussel with a shell length of 5.0 cm weighs ~2.195 g (Equation 5). The initial V is 1.953125 cm^3(Equation 6), the initial E is 410.16 J (Equation 7) and the initial value for R is 175.78 J (Equation 8).

$$W_{Start} = 1\frac{g}{cm^3} * \left((5\ cm * 0.25)^3 + \frac{\frac{(5\ cm*0.25)^3}{cm^3}*300*0.7\ J}{1900\frac{J}{cm^3}}\right) + \frac{\frac{(5\ cm*0.25)^3}{cm^3}*300*0.3\ J}{6750\frac{J}{g}} = {\sim}2.195\ g$$

Equation 5: Initial weight

$$V_{Start} = (L * \delta_m)^3 = (5\ cm * 0.25)^3 = 1.953125\ cm^3$$

Equation 6: Initial volume

$$E_{Start} = \frac{V_{Start}}{cm^3} * 300 * 0.7\ J = 410.16\ J$$

Equation 7: Initial energy reserve

$$R_{Start} = \frac{V_{Start}}{cm^3} * 300 * 0.3\ J = 175.78\ J$$

Equation 8: Initial energy content of reproductive organs

3.1.3. Modelled Mussel Growth

The growth rate of a mussel (dW/dt), measured in g / day, can also be derived from Equation 1, by inserting the change in E over time (dE/dt), measured in J / day, the change in V over time (dV/dt), measured in cm^3 / day, and the change in R over time (dR/dt), measured in J / day, in the equation instead of E, V and R (Equation 9).

$$\frac{dW}{dt} = d * \left(\frac{dV}{dt} + \frac{(\frac{dE}{dt})}{[E_G]} \right) + \frac{(\frac{dR}{dt})}{\mu_E}$$

Equation 9: Growth rate

Change in E over time (dE/dt) is calculated by subtracting the energy utilization rate ($\dot{p}_c$), with unit J / day, from the assimilation energy rate ($\dot{p}_a$), with unit J / day (Equation 10).

$$\frac{dE}{dt} = \dot{p}_a - \dot{p}_c$$

Equation 10: Change in energy reserve over time

Change in somatic volume over time (dV/dt) is calculated by Equation 11.

$$\frac{dV}{dt} = \frac{\kappa * \dot{p}_c - [\dot{p}_m] * V}{[E_G]}$$

Equation 11: Change in volume over time

Change in R over time (dR/dt) is calculated by Equation 12.

$$\frac{dR}{dt} = (1 - \kappa) * \dot{p}_c - \left(\frac{1 - \kappa}{\kappa} \right) * V_p * [\dot{p}_M]$$

Equation 12: Change in energy content of reproductive organs over time

The assimilation energy rate ($\dot{p}_a$) is calculated by Equation 13, where $\dot{p}_{Am}$ is the maximum surface area-specific assimilation rate and has a value of 147.6 J / cm * day (Van der Veer et al. 2006), *f* is the functional response function and has no unit (Equation 14) and *k*(T) is the temperature dependence, which also lacks unit (Equation 15).

$$\dot{p}_a = \{\dot{p}_{Am}\} * f * k(T) * V^{2/3}$$

Equation 13: The assimilation energy rate

The functional response function (*f*) is a mussel's food uptake given a certain food density (Holling 1959). It has a value between 0 and 1 and is calculated by dividing the concentration of available food (X), with unit mg C / m^3, with X plus the half saturation coefficient (X_k), also with unit mg C / m^3.

$$f = \frac{X}{X + X_k}$$

Equation 14: The functional response

Food sources for mussels are carbon from phytoplankton (Phyto-C), unit mg C / m^3, and particulate organic carbon (POC) , unit mg C / m^3. Only Phyto-C was considered in the present study since its focus is on offshore areas where the POC-concentrations are low compared to Phyto-C, and since Hatzonikolakis et al. (2017) found that POC contributed little or not at all to mussel growth at two sites in the Aegean Sea. Following Hatzonikolakis et al. (2017), a mean ratio of 50 : 1 was assumed for Phyto-C : chl *a* (Malone and Chervin 1979; Geider and Platt 1986; Kormas et al. 2002).

The half saturation coefficient (X_k) is the amount of food where food uptake is at half its maximum value. X_k represents the physiological response of the mussel to its environment. Its variations depend on genes as well as on environmental conditions, and as such is site specific. It likely varies due to the different compositions of phytoplankton at different sites, which translates to varying ratios of chl *a* and Phyto-C depending on phytoplankton species and their mutual magnitudes in the water (Alunno-Bruscia et al. 2011). The value for X_k is expected to be higher in areas with more primary production (Hatzonikolakis et al. 2017). Hatzonikolakis et al. (2017) found the values 28 mg C / m^3 and 36 mg C / m^3 for the relatively nutrient poor Maliakos gulf and Thermaikos gulf, respectively. The two areas are located in the Greek part of the Aegean Sea in the Eastern Mediterranean. Casas and Bacher (2006) concluded that 194 mg C / m^3 was sufficiently correct to use in both nutrient rich areas Lazaret and Port-Cros located close to Toulon on the French Mediterranean coast.

The present study used an initial value of 194 C / m^3 for X_k since it was derived from *M. galloprovincialis* in the French Mediterranean. The parameter was nonetheless assessed in the sensitivity analysis discussed in a later section since, While Port-Cros and Baie du Lazaret are geographically relatively close to some of the sites for collection of RINBO data, the X_k may be expected to be different there compared to sites further east or west since the primary production varies along the coastline. To the west of Port-Cros and Baie du Lazaret, in the GoL, the primary production is higher. In sharp contrast are the oligotrophic waters east of Port-Cros and Baie du Lazaret, i.e., off the French Riviera. In addition, X_k is the most commonly calibrated DEB parameter. Casas and Bacher (2006), Hatzonikolakis et al. (2017) and Filgueira et al. (2011) all calibrated X_k. Rosland et al. (2009) used four datasets from laboratory experiments to calibrate X_k. Larsen et al. (2014) tested and compared the DEB method to similar models and concluded that it relied on the calibration of the X_k.

The temperature dependence [k(T)] indicates how the ambient temperature (in our case SST) affects food uptake and energy assimilation. Theoretically, the closer the mussel is to its optimum temperature, the more efficiently it can filter feed and turn that food into energy. The temperature dependence is dependent on the Arrhenius temperature (T_A), the reference temperature (T_I), the lower boundary of tolerance range (T_L), the upper boundary of tolerance range (T_H), the Arrhenius temperature for rate of decrease at lower boundary (T_{AL}) and the Arrhenius temperature for rate of decrease at upper boundary (T_{AH}) according to Equation 15.

$$k(T) = \frac{exp\left(\frac{T_A}{T_I} - \frac{T_A}{T}\right)}{1 + exp\left(\frac{T_{AL}}{T} - \frac{T_{AL}}{T_L}\right) + exp\left(\frac{T_{AH}}{T_H} - \frac{T_{AH}}{T}\right)}$$

Equation 15: The temperature dependence

The values for T_A, T_I, T_L, T_H, T_{AL} and T_{AH} were measured for *M. edulis* by Van der Veer et al. (2006) and their values are 5800 K, 293 K, 275 K, 296 K, 45430K, and 31376 K, respectively.

Since *M. galloprovincialis* is known to withstand higher temperatures than *M. edulis*, and since the DEB parameters are based on *M. edulis*, it is reasonable to believe that at least one of the temperature parameters from Van der Veer et al. (2006), notably T_H, are not optimal when modelling *M. galloprovincialis* in the Mediterranean. The value of 303 K has been suggested by the DEB Laboratory portal Add-my-Pet (Kooijman et al. 2022). However, the value is not supported by evidence published in a scientific article and is therefore considered unreliable. Due to the uncertainties regarding T_H, the parameter was included in the sensitivity analysis discussed in a later section.

The energy utilization rate ($\dot{p}_c$) is the amount of energy used to feed and turn the food into energy. It is calculated according to Equation 16, where $[E_m]$ is the maximum energy density with value 2190 J / cm^3 (Van der Veer et al. 2006) and [E], with unit J / cm^3, is the amount of energy reserves per volume unit (Equation 17).

$$\dot{p}_c = \frac{[E]}{[E_G] + \kappa * [E]} * \left(\frac{[E_G] * \dot{p}_{Am} * k(T) * V^{2/3}}{[E_m]} + [\dot{p}_M] * V\right)$$

Equation 16: The energy utilization rate

$$[E] = \frac{E}{V}$$

Equation 17: Energy reserves per volume unit

The fraction of utilised energy spent on maintenance and growth (κ), which lacks unit, is 0.7, meaning that 70% of the incoming energy (E) is allocated to the soma structure maintenance and growth and 30% is allocated to the reproductive cells (Kooijman 2010). The energy is first used for maintenance and remaining energy is used for growth. The maintenance costs $[\dot{p}_M]$, unit J / cm^3 * day, is calculated according to Equation 18, where $[\dot{p}_M]_m$ is the volume specific maintenance cost with a value of 24 J / cm^3 * day (Van der Veer et al. 2006).

$$[\dot{p}_M] = k(T) * [\dot{p}_M]_m$$

Equation 18: The maintenance cost

Finally, V_p is the soma volume at the start of reproductive age and has a value of 0.06 cm^3 (Van der Veer et al. 2006). All parameters, constants and equations are presented in Appendix A (

Table A 1; Table A 2; Table A 3).

The equations were tested for errors by comparing it to a model set up in an workbook in software Microsoft Excel version 2204 (Microsoft Corporation 2021a), where one sheet was designated to initial values, one to parameters and one to equations. An identical result (20 decimals were controlled for) was required from the Excel spreadsheets and the DEB equation to exclude suspicion of error.

3.2. Data

3.2.1. Study Area

The area of interest for the base- and climate change scenarios was the offshore waters in the French Exclusive Economic Zone (EEZ). There are several definitions as to what is considered "offshore." According to French fishing laws, commercial fishing is considered offshore if the fishing trips last longer than 96 hours (IFREMER 2011). Other definitions, such as offshore fishing being more than 12 nautical miles from the shoreline, are sometimes preferred by professionals within the French fishing industry (IFREMER 2011). With regards to mussel farms, depth is more important than distance from shore since other types of farming may be considered in shallower waters. Froehlich et al. (2017) conducted a comprehensive study of offshore aquaculture literature and found that the shallowest points of offshore aquaculture farms were located at a mean depth of 28.9 m ± 9.2 m, indicating that offshore farms are generally located in waters deeper than 30 m. In addition, 30 m is often considered the limit between onshore and offshore fishing, with shallower waters being shallow subtidal habitat. Therefore, waters deeper than 30 m is a reasonable definition of offshore.

A shapefile for the EEZs of the world was obtained from the Flanders Marine Institute (2019). The data set is covered by Creative Commons license and is intended for educational- and research purposes (Creative Commons 2022). The shapefile had the coordinate system WGS 84 (EPSG:4326) and were opened in software ArcGIS Pro 2.7.3, manufactured by Esri Inc. located in Redlands, California, the United States of America (Esri Inc. 2022). All polygons were deleted except for the French EEZ, which was exploded into the Atlantic EEZ and the Mediterranean EEZ, of which only the Mediterranean EEZ was kept.

Bathymetry data were obtained from the European Marine Observation and Data Network (EMODnet) (European Commission 2022). The EMODnet Bathymetry Viewing and Download service is built and maintained by GGS Geo Consultancy and partners on behalf of the European Commission and coordinated by the Marine Information Service. Four tiles were downloaded (E4, E5, F4 and F5) as ESRI ASCII files and opened in ArcGIS Pro. The cell size was 1/8 arc minute (ca 230 m) and the coordinate system WGS 84 (EPSG:4326). Once opened in ArcGIS Pro, the four tiles were merged using Geoprocessing tool "Mosaic", and their coordinate system defined.

The resulting raster was clipped to the extent of the Mediterranean EEZ polygon and then reclassified, using Geoprocessing Spatial Analyst tool "Reclassify", into two values: 0 for depths shallower than 30 m and 1 for depths deeper than 30 m. The raster was then converted to a polygon shapefile using Geoprocessing tool "Raster to Polygon". All polygons with value 1 were merged using the Modify Features Merge function, and remaining polygons were deleted. The resulting polygon is presented in Figure 6.

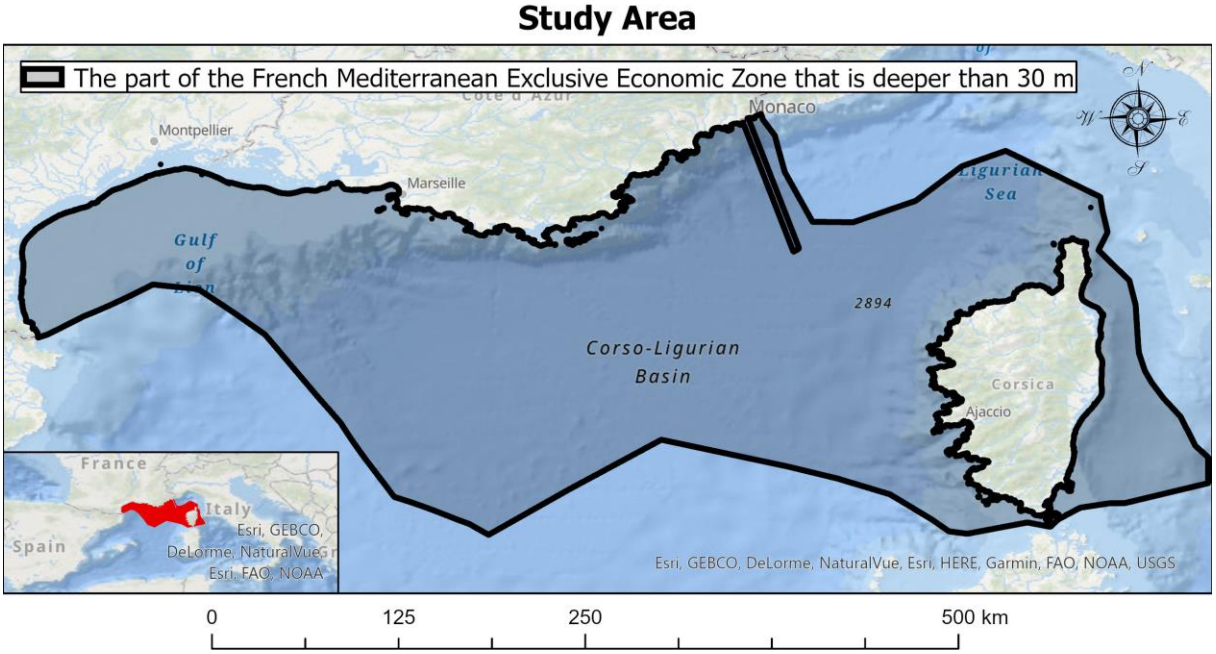

Figure 6: Polygon shapefile of the study area: the part of the French Mediterranean Exclusive Economic Zone that is deeper than 30 m.

For the calibration and validation, the area surveyed was expanded to bounding box 44.63° north, 2.54° west, 12.91° east and 40.98° south, to encompass as many sample spots as possible.

3.2.2. Sea Surface Temperature

3.2.2.1. The European Union's Earth Observation Programme Copernicus

For historical growth as well as for the in situ validation, SST rasters were obtained from the European Union Earth observation programme Copernicus. The data series used was the Mediterranean Sea and Black Sea Surface Temperature NRT with product identifier SST_MED_SST_L4_NRT_OBSERVATIONS_010_004_c, coordinate system WGS 84, a cell size of 0.01°, a temporal resolution of 1 day, and bounding box 44.63° north, 2.54° west, 12.91° east and 40.98° south (Copernicus 2021a). Once downloaded as NetCDF-files (*.nc), the data were imported to ArcGIS Pro. The geoprocessing tool "Make NetCDF Raster Layer" was used for the import. The resulting files were multiband rasters where each band consisted of a raster layer with the SST values for one day.

3.2.2.1.1. Historical Growth

The dates downloaded for the historical growth were January 1st 2011 – December 31st 2020, resulting in 3652 bands. Due to the large size of a file with that quantity of bands, the data were downloaded by year. The extent of the SST rasters, as well as mean values for 2011 - 2020, for bounding box 44.63° north, 2.54° west, 12.91° east and 40.98° south, are shown in Figure 7.

Mean values for 2011 - 2020 in the study area, i.e., offshore in the French Mediterranean EEZ, are shown in Figure 8. Variability of the mean SST for the study area is presented in Figure 9 and Figure 10.

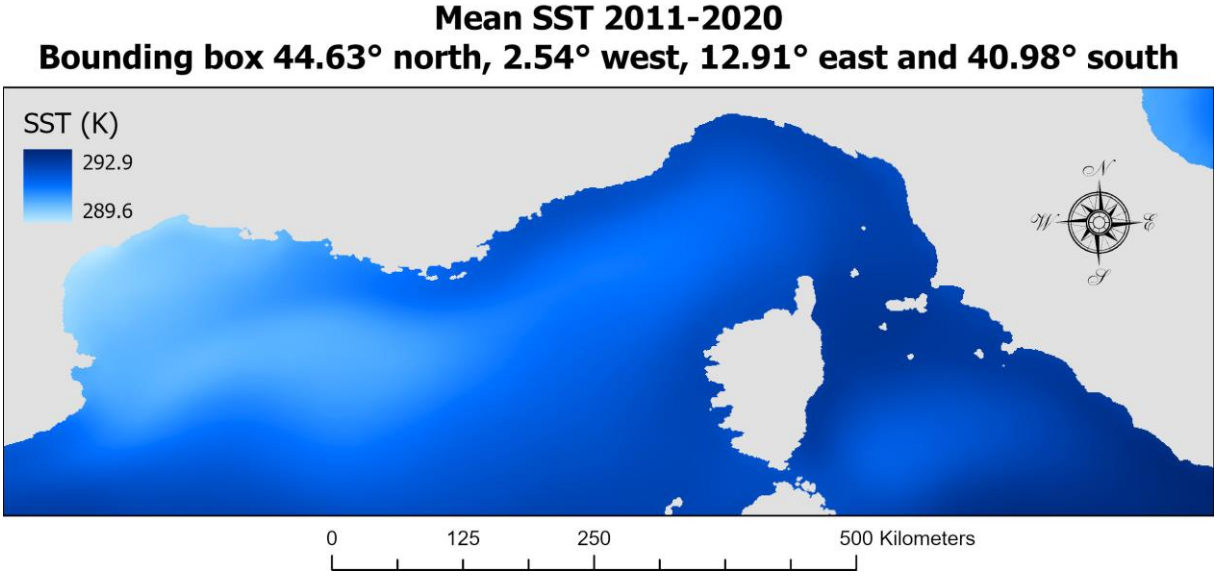

Figure 7: Mean SST for years 2011 - 2020, bounding box 44.63° north, 2.54° west, 12.91° east and 40.98° south, modelled using data from the European Union Earth observation programme Copernicus. Surface waters are coldest in the northwest of the studied area, namely in the Gulf of Lion. Surface waters are also cold offshore in the Ligurian and Tyrrhenian Seas but warmer close to shore on the French Riviera, along the coast of Italy and between Italy and Corsica.

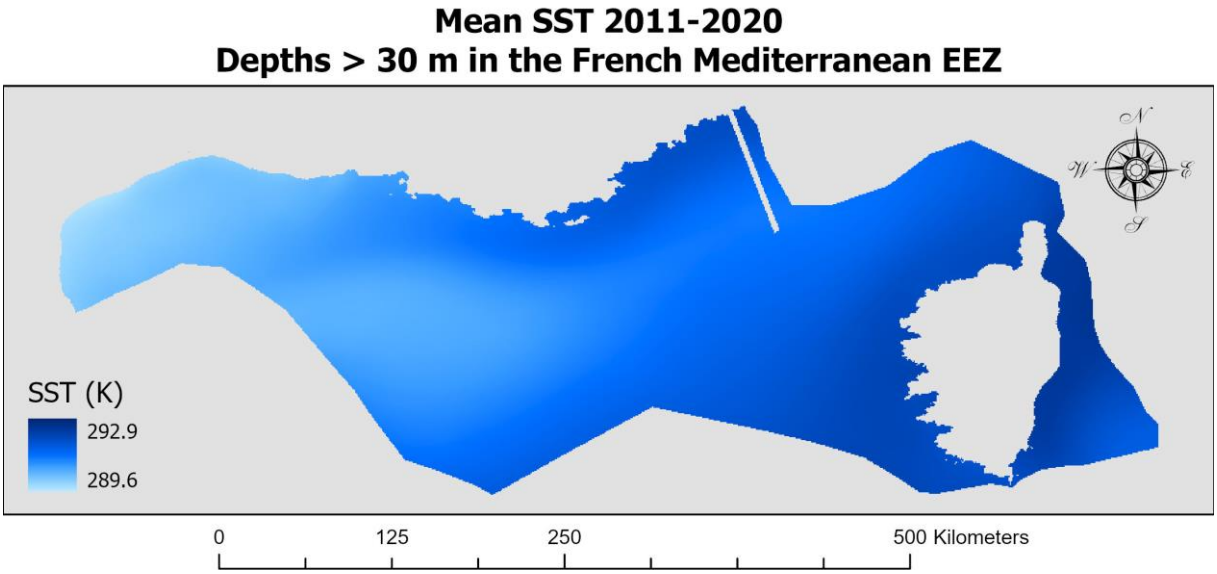

Figure 8: Mean SST for years 2011 - 2020, offshore in the French Mediterranean EEZ, modelled using data from the European programme Copernicus.

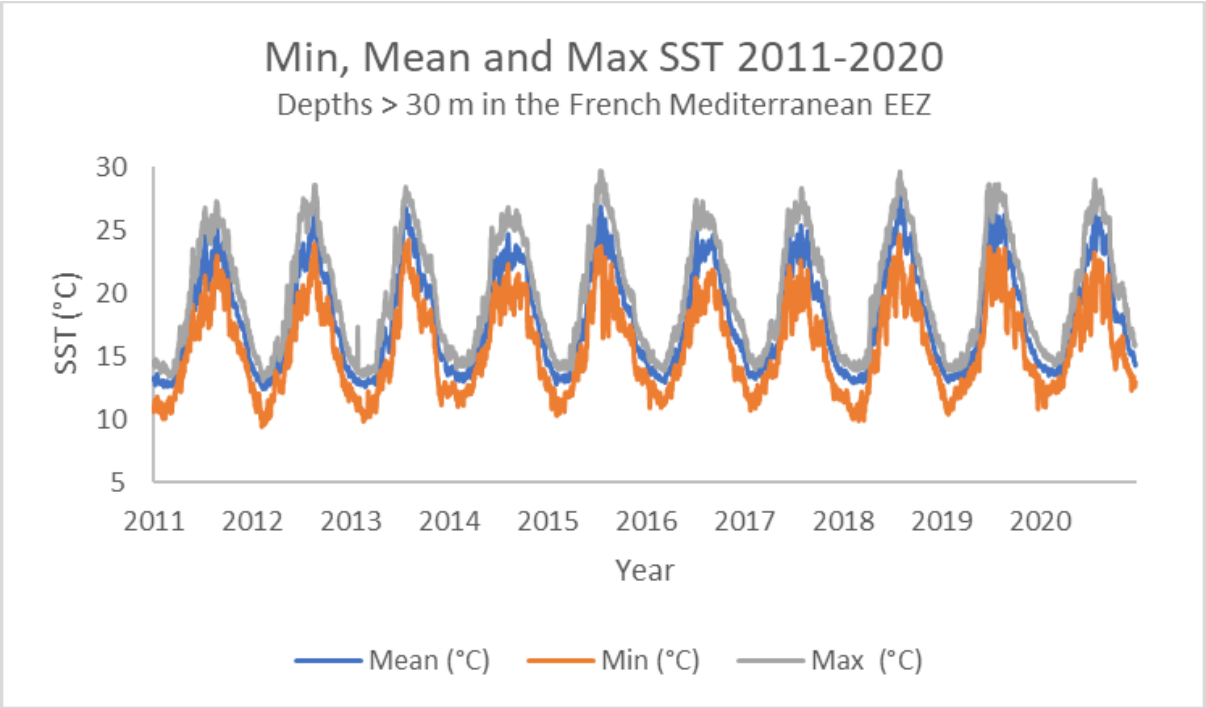

Figure 9: Variability of the daily min, mean and max SST for years 2011 - 2020 offshore in the French Mediterranean EEZ. All data points are presented in one curve starting Jan 1st 2011 and ending December 31st 2020.

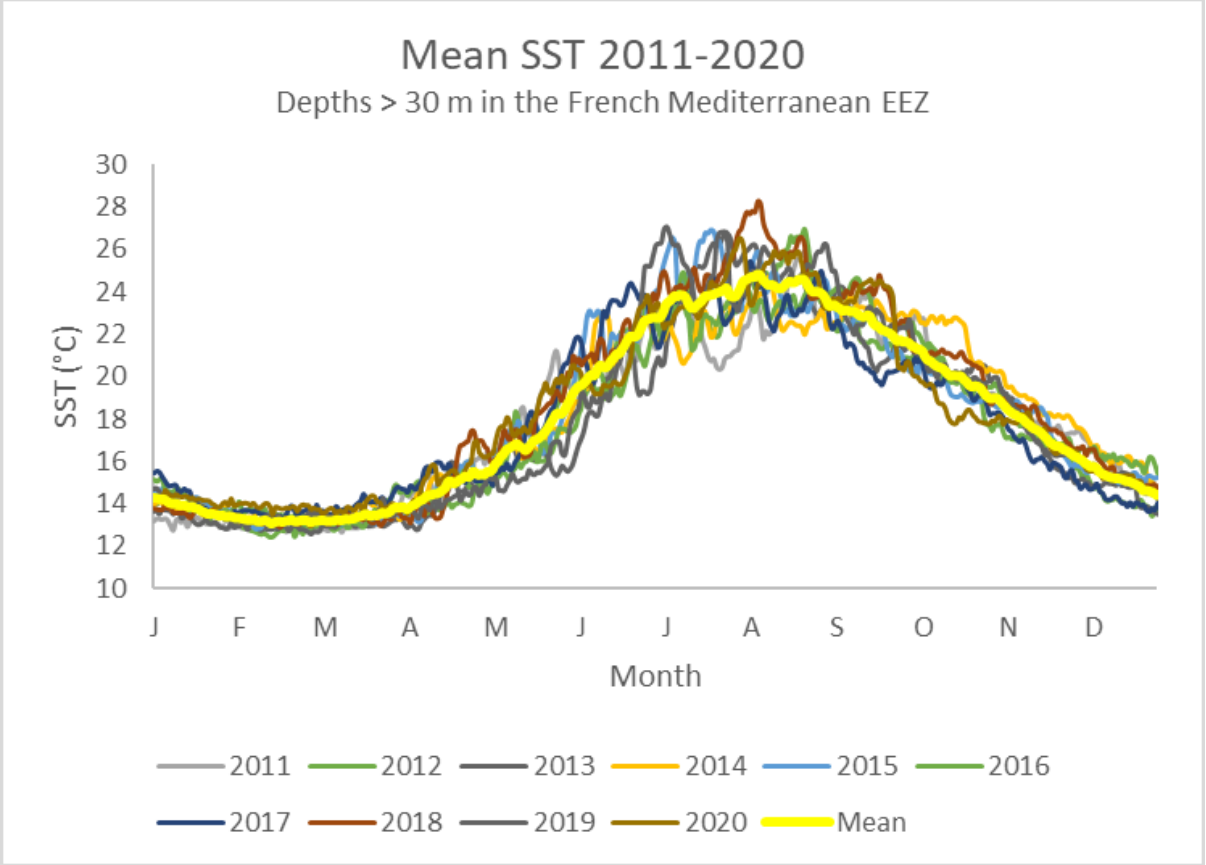

Figure 10: Variability of the daily mean SST for years 2011 - 2020 offshore in the French Mediterranean EEZ. Data points are presented in ten curves, one per year, each starting Jan 1st and ending December 31st.

3.2.2.1.2. Calibration and Validation

The model was calibrated using observations of mussel growth at different sample spots. The mussels at each spot were submerged approximately 3 months, however the exact number of days varied. The dates downloaded for the calibration and validation corresponds to the dates that the mussels observed at each sample spot were submerged. For season 2015, the dates were Jan 1st 2015 – July 31st 2015 since no mussels were placed in the water before January 1st and no mussels were collected after July 31st. The dates downloaded for the in situ validation for season 2018 were December 30th 2017 – December 31st 2017 and January 1st 2018 – July 31st 2018 since no mussels were placed in the water before December 30th 2017 and no mussels collected after July 31st 2018. Even though the dates overlap with those used to model historical growth, original downloads were made to download rasters from the dates specific to model calibration and validation. The result was three multiband raster files including 212, 2 and 212 bands respectively, where each band represented the daily SST value (Figure 11). For the rasters with 212 bands, band 1 represented January 1st, band 2 represented January 2nd, and so on to band 212 which represented July 31st. For the raster with two bands, band 1 represented December 30th 2017 and band 2 December 31st 2017.

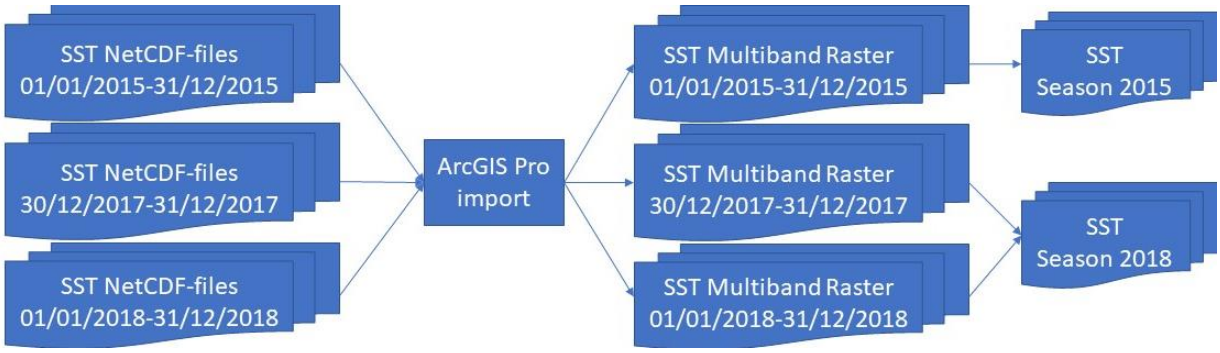

Figure 11: Workflow to obtain SST multiband rasters for in situ validation of mussel growth data.

3.2.2.2. The Intergovernmental Panel on Climate Change

3.2.2.2.1. Climate Change Scenario

The SST data available for different IPCC climate change scenarios were rasters with a spatial resolution of 0.44° (i.e., cells are about 200 times larger than the cells in rasters with historical chl *a* and SST data) and a temporal resolution of one month, representing the prospective monthly mean. Two types of raster data were available: expected SSTs and expected SST increase. Using the IPCC rasters for expected SSTs entail two drawbacks. First, the coarse resolution is unhelpful when searching to locate areas for mussel cultivation, considering that a mussel farm is no more than a few hundred meters across and thus hundreds of them would fit into one raster cell sized 0.44 ° x 0.44 °. Secondly, the coarse temporal resolution excludes important day by day variation.

An alternative, allowing a finer spatial resolution and day by day variation, is to add the mean monthly increase in SST predicted for scenario RCP 8.5 Long Term to daily raster data for the corresponding month of historical SST rasters (Figure 12). This alternative results in a climate change prediction with a spatial resolution of 1 km and a temporal resolution of 1 day (same as the historical data).

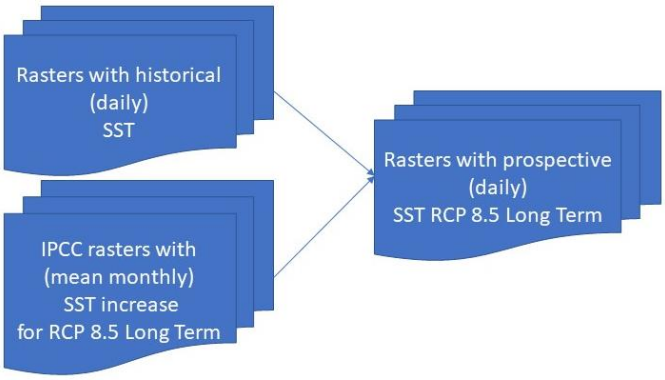

Figure 12: Workflow for creating rasters with predicted daily SSTs for climate change scenario RCP 8.5 Long Term.

The IPCC raster data for mean monthly SST increase in climate change scenario RCP 8.5 Long Term (i.e., for period 2081-2100) were obtained from a CORDEX Mediterranean annual dataset with baseline 1995-2014 (i.e., it is the increase since 1995-2014), made available online by the IPCC Working Group I Interactive Atlas (IPCC 2021a). The raster used was for climate change scenario RCP 8.5 Long Term i.e., prediction for years 2081-2100. The CORDEX dataset uses a rotated coordinate system and a spatial resolution of 0.44°. CORDEX data can be used freely for educational and research purposes (Cordex 2021).

Rasters were downloaded as TIFF-files and imported to ArcGIS Pro, resulting in singleband rasters, representing the mean SST increase values for one month each. Each SST increase raster was added to all corresponding individual rasters with historical SST data using Geoprocessing tool "Raster Calculator." For example, the SST increase raster for January 2014 was added to the 31 individual rasters representing historical SST values from January 1st – January 31st 2014. The result was daily rasters with prospective SSTs for the month of January during the warmest year of climate change scenario RCP 8.5 Long Term.

3.2.3. Chlorophyll a

3.2.3.1. The European Union's Earth Observation Programme Copernicus

Rasters with chl *a* values were obtained from the European Union's Earth observation programme Copernicus. The data series used was the Mediterranean Sea Daily Reprocessed Surface Chlorophyll Concentration from Multi Satellite observations with product identifier OCEANCOLOUR_MED_CHL_L4_REP_OBSERVATIONS_009_078, coordinate system WGS 84, a cell size of 1 km, and bounding box 44.63° north, 2.54° west, 12.91° east and 40.98° south (Copernicus 2021b). Once downloaded as NetCDF-files (*.nc), the data were imported to ArcGIS Pro. The resulting files were multiband rasters where each band consisted of a raster layer with the values for one temporal resolution (i.e., one day).

3.2.3.1.1. Historical Growth

The dates used for historical growth were January 01st 2011 – December 31st 2020. Mean values for the entire period for bounding box 44.63° north, 2.54° west, 12.91° east and 40.98° south are presented in Figure 13. Mean values for 2011 - 2020 in the study area, i.e., offshore in the

French Mediterranean EEZ, are presented in Figure 14. Variability of the minimum, mean and maximum SST for the study area is presented in Figure 15, Figure 16, Figure 17 and Figure 18.

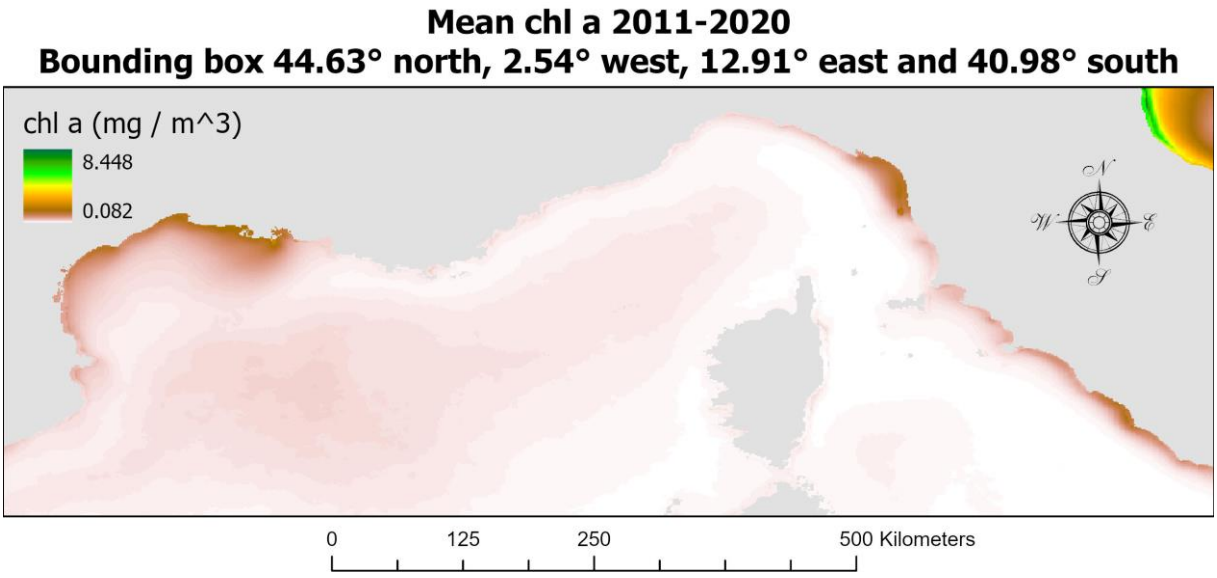

Figure 13: Mean chl a for years 2011 - 2020, for bounding box 44.63° north, 2.54° west, 12.91° east and 40.98° south. Modelled in ArcGIS Pro using raster data from the European Union Earth observation programme Copernicus. The predominantly nutrient poor Mediterranean Sea is characterized by low levels of chl a in the open ocean and a few areas with higher chl a close to shore where rivers and water column mixing add nutrients to the surface waters and enable more primary production.

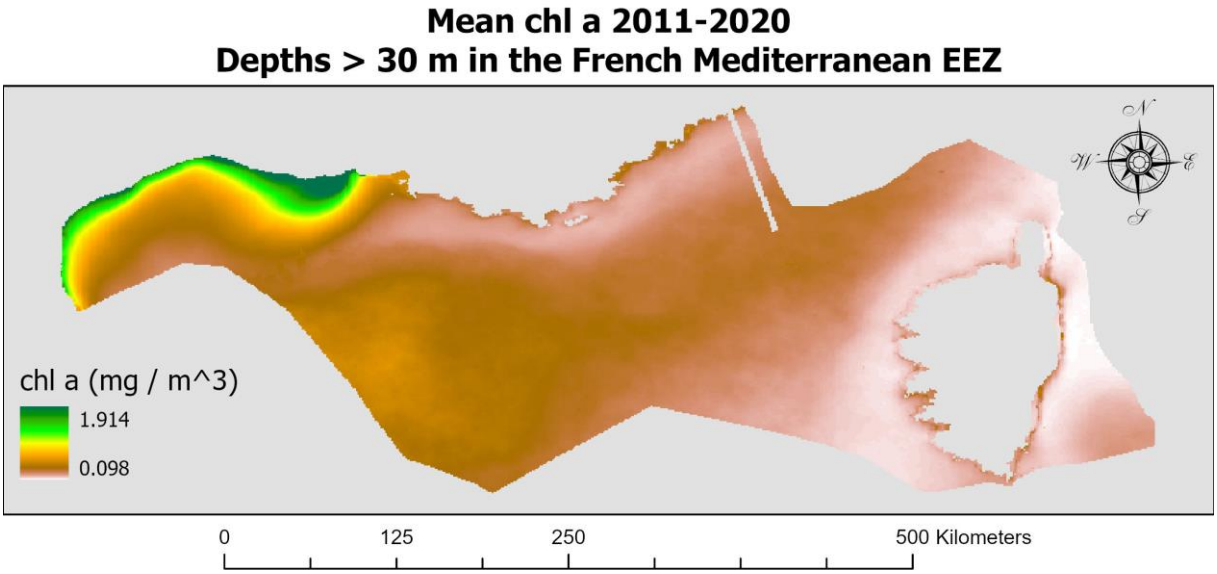

Figure 14: Mean chl a for years 2011 - 2020 offshore in the French Mediterranean EEZ. Modelled in ArcGIS Pro using raster data from Copernicus. The bulk of the waters richest in nutrients in the study area are located in the GoL.

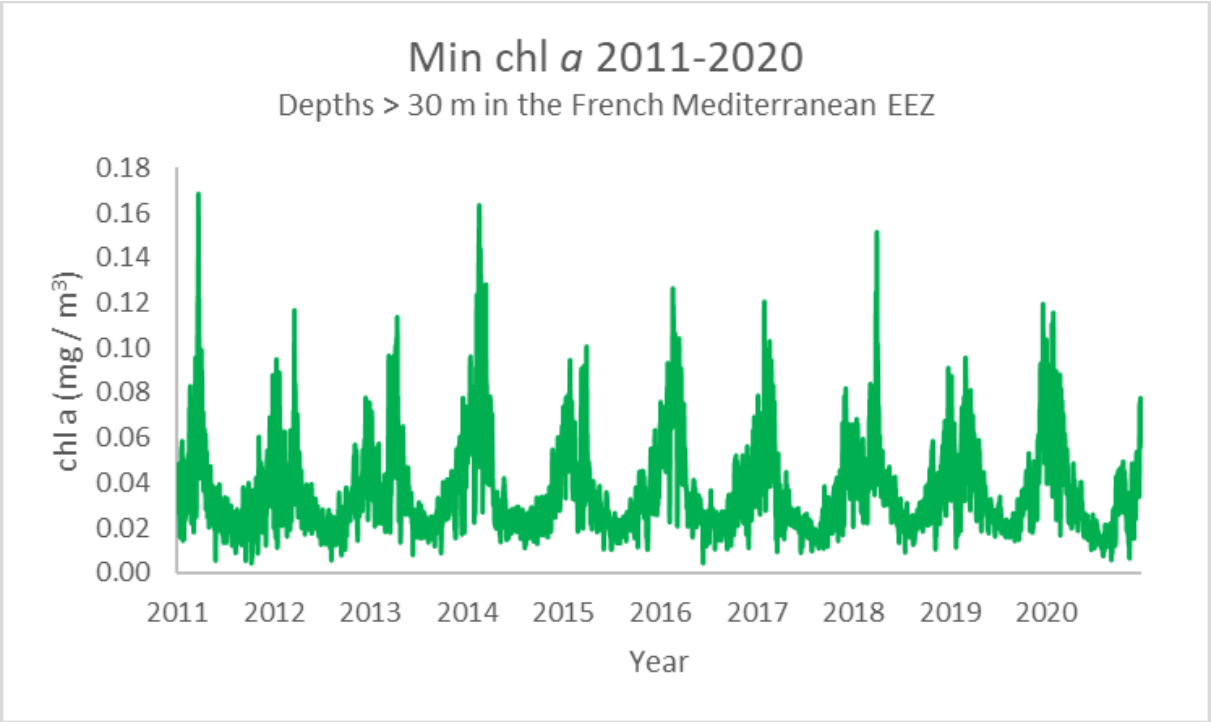

Figure 15: Variability of the daily minimum chl a for years 2011 - 2020 offshore in the French Mediterranean EEZ. All data points are presented in one curve starting Jan 1st 2011 and ending December 31st 2020.

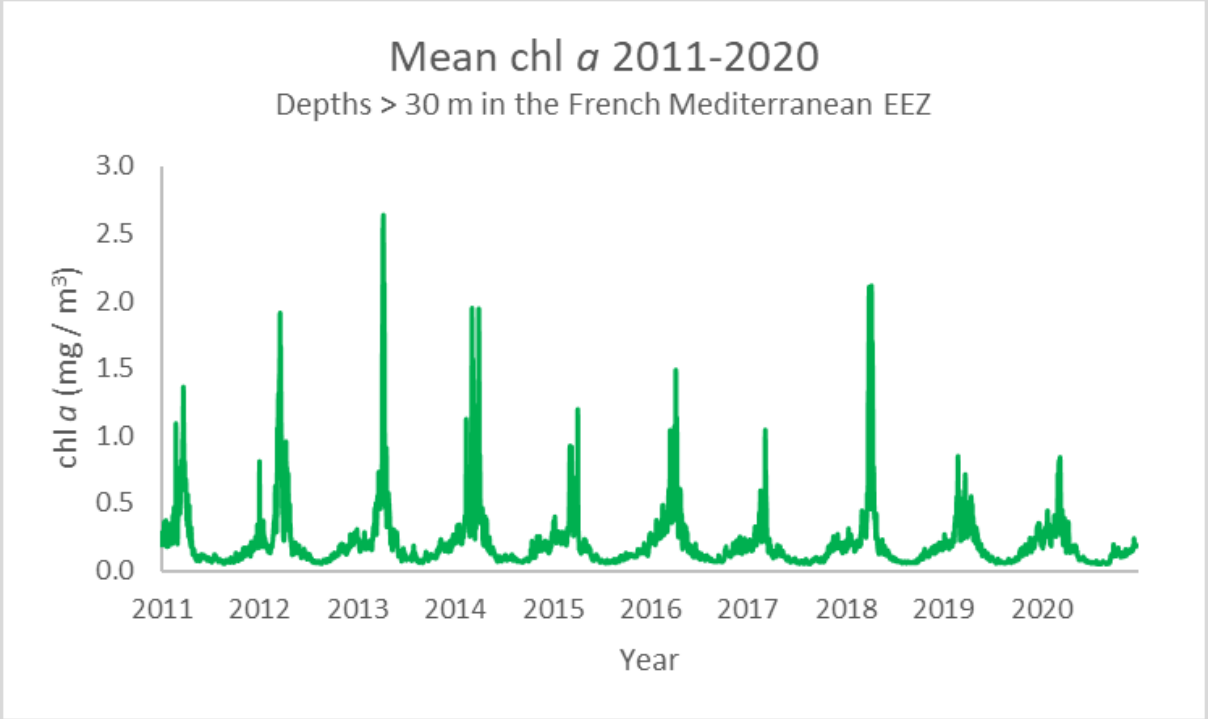

Figure 16: Variability of the daily mean chl a for years 2011 - 2020 offshore in the French Mediterranean EEZ. All data points are presented in one curve starting Jan 1st 2011 and ending December 31st 2020.

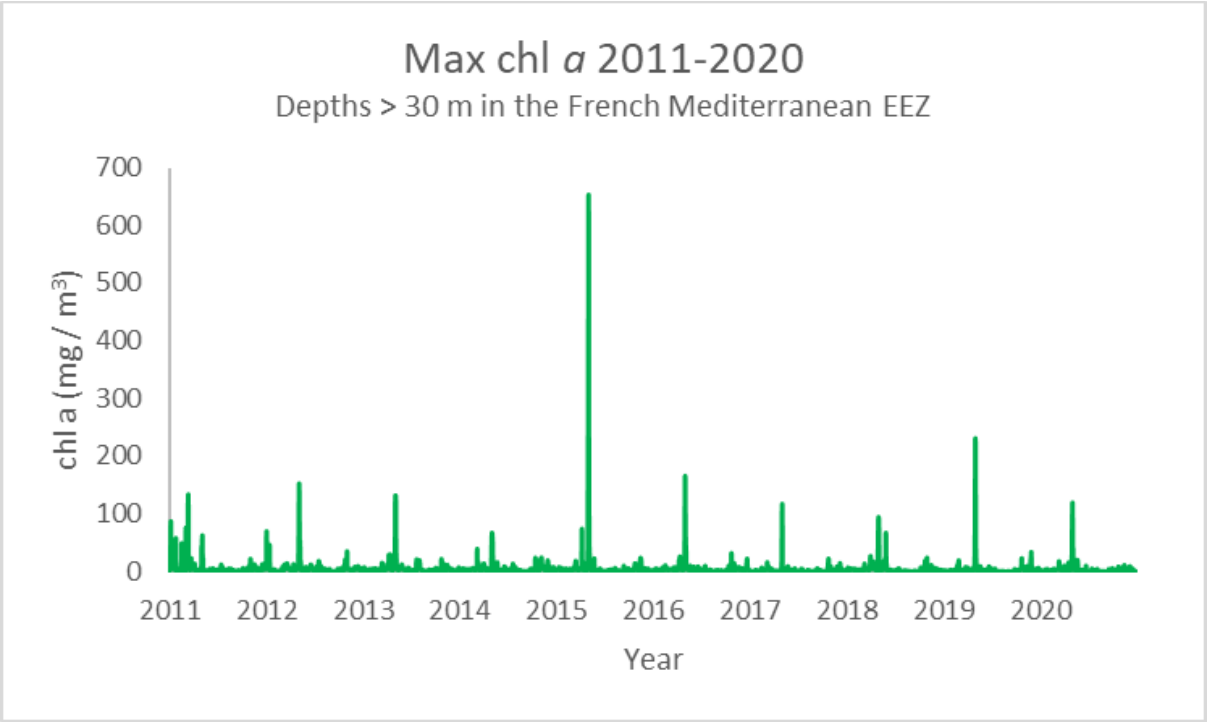

Figure 17: Variability of the daily maximum chl a for years 2011 - 2020 offshore in the French Mediterranean EEZ. All data points are presented in one curve starting Jan 1st 2011 and ending December 31st 2020.

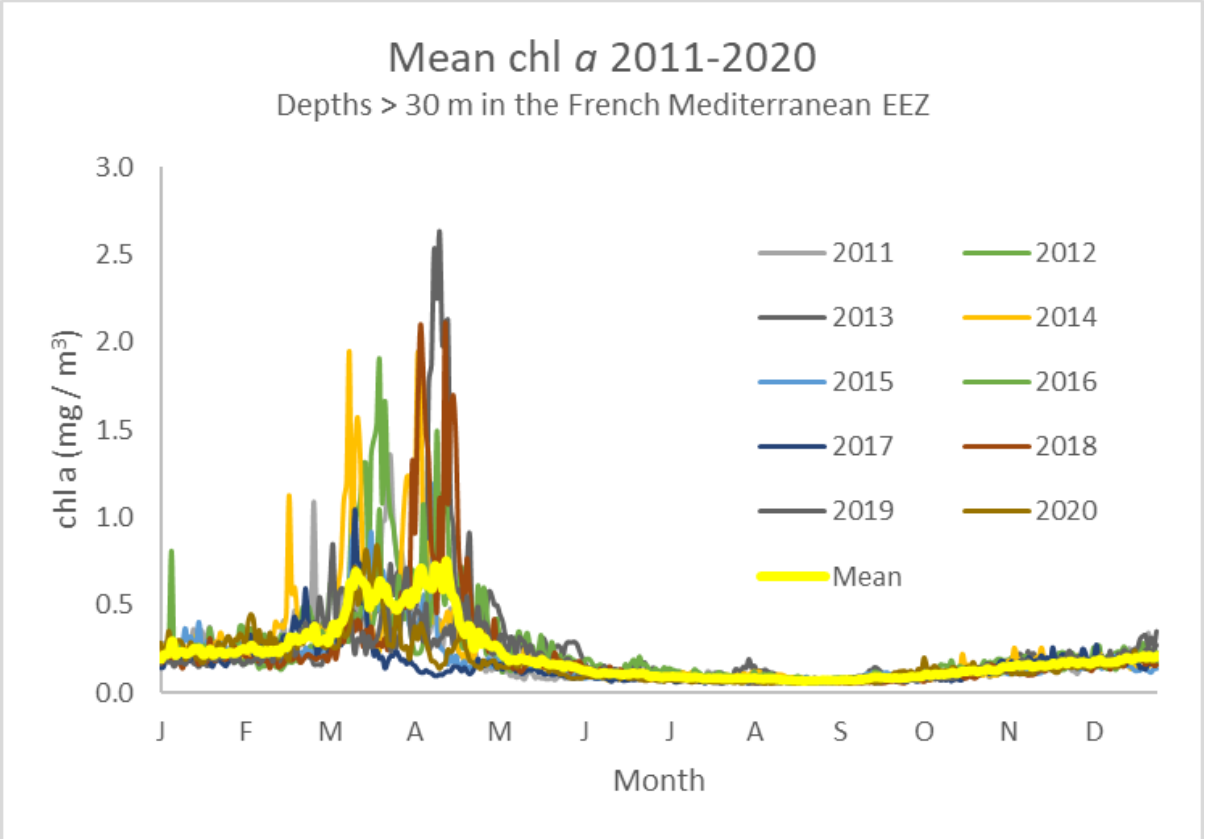

Figure 18: Variability of the daily mean chl a for years 2011 - 2020 offshore in the French Mediterranean EEZ. Data points are presented in ten curves, one per year, each starting Jan 1st and ending December 31st.

3.2.3.1.2. Climate Change Scenario

Historical data were used for the climate change scenario as well. However, more dates were used since the dataset for the climate change scenario included all available complete years (i.e., years where data for all dates were present), for a total period ranging from January 1st 1998 to December 31st 2020.

3.2.3.1.3. Calibration and Validation

The dates used for the calibration and validation were January 1st 2015 – July 31st 2015, December 30th 2017 – December 31st 2017 and January 1st 2018 – July 31st 2018, resulting in three multiband rasters with 212 bands, 2 bands and 212 bands, respectively (Figure 19).

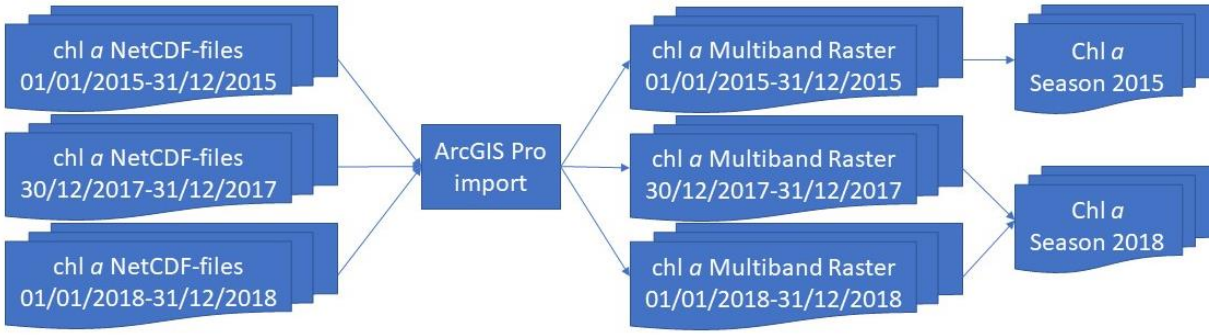

Figure 19: Workflow to obtain chl a multiband rasters for in situ validation of mussel growth data. The data was downloaded from Copernicus as NetCDF-files and imported to ArcGIS Pro using Geoprocessing tool "Make NetCDF Raster Layer." Resulting multiband rasters constituted chl a raster data for the two growing seasons 2015 and 2018.

3.3. Model Assessment

Important decisions are based on GIS models; hence the model's certainty level must be assessed (Crosetto and Tarantola 2010). The accuracy and precision of the model are vital tools for ameliorating the model as well as for correct interpretation of the results and efficient implementation of subsequent measures.

A model's accuracy is best assessed by comparing the modelled results with what is considered to be true values, such as Ground Control Points (GCP). The less difference between the two, the more accurate the model is considered to be. GCPs are often collected and measured specifically for a research project to make sure that the data fulfils the necessary requirements for the project. However, this process is time consuming. A more time- and cost efficient alternative is to use data already collected and made freely available, such as the in situ growth measurements observations made by the French oceanic institute IFREMER. A total of 42 observations were used for modelling in ArcGIS Pro and 75 for modelling in Excel. The modelled values were compared to the measured values using scatter plots.

The model was considered highly accurate if the modelled growth corresponded at least 90 % to the measured growth, meaning that the resulting graph's R^2 be at least 0.9, the slope between 0.9 and 1.1, and the intercept of the y-axis between -0.1 and 0.1. The model was considered accurate if the two corresponded at least 70 % ($R^2 \geq 0.7$, slope 0.7-1.3, intercept -0.3-0.3), sufficiently accurate if they corresponded at least 50 % ($R^2 \geq 0.5$, slope 0.5-1.5, intercept -0.5-

0.5), and inaccurate if they corresponded less than 50 % ($R^2 < 0.5$, slope < 0.5 or >1.5, intercept <-0.5 to >0.5).

As outlined by Crosetto and Tarantola (2010) in their recommendations to the European Union regarding assessment of geographical data, a Sensitivity Analysis (SA) is to be executed when the model's accuracy is insufficient. An SA is used to assess a model's precision by investigating how the uncertainty of input factors affect the model's output. It may also identify one or several variables for which the model is sensitive, as a means to decide what parameters to calibrate. There are different types of SA. Some, such as the Monte-Carlo (MC) method, analyse the change in output caused by the combined potential errors of all input factors (Crosetto and Tarantola 2010). The MC is an efficient model recommended by the Joint Research Centre at the European Commission (European Commission Joint Research Centre 2022; Crosetto and Tarantola 2010). However, it is a time consuming method that requires programming in R. A type of SA that is more time efficient is the One At a Time (OAT) analysis. It analyses the potential change in output caused by one input factor at a time and provides an insight into the uncertainty of the model. The parameter or parameters that causes the largest change in output is then calibrated and the model accuracy assessed anew.

3.3.1. Accuracy

3.3.1.1. Measured Growth

The French oceanographic institution l'Institut Français de Recherche pour l'Exploitation de la Mer (IFREMER) has gathered mussel growth data from between 70 and 120 sample spots in the French Mediterranean every few years for the past two decades (exact years are 1996, 1998, 2000, 2003, 2006, 2009, 2012, 2015 and 2018) as a part of their project Le Réseau INtégrateurs BIOlogiques (RINBIO) (Bouchoucha et al. 2021).

For the data relevant to the present study, mussels of the species *M. galloprovincialis* were placed in the water by the science agency Bureau d'études BIOLITTORAL in Nantes. Nets containing 2.5 kg homogenous mussels, 50 mm in length, were submerged at each sample spot for approximately three months. At deep-water sample spots, weights and buoys were used to submerge the mussel nets at a depth of 15 m.

After approximately three months in the water, the mussels were collected by hand by the IFREMER laboratories Laboratoire Environnement Ressources Languedoc Roussillon (LERLR) and Laboratoire Environnement Ressources Provence Alpes Côte d'Azur (LERPAC).

The samples were analysed by the IFREMER laboratories LERPAC, Laboratoire d'Etude des Résidus et Contaminants dans les Aliments (LABERCA) and Laboratoire Biogéochimie des Contaminants Métalliques (LBCM). The number of mussels in each sample was recorded and the mussel tissue was mechanically extracted from the shells by hand. Dry weight was measured after lyophilisation (i.e., freeze drying) of the mussel tissue from all mussels in the sample. Dry matter was measured by weighing the mussel tissue before and after lyophilisation, then dividing the dry weight with the wet weight.

The resulting data has been made available to the public via IFREMER's online and open access database Quadrige[2] and its corresponding web interface Surval (IFREMER 2021). The data was downloaded as a CSV-file and processed in Excel (Figure 20). Sampling spot, longitude, latitude, sampling date (i.e., the day the mussels were collected from the sea), number of individuals in each sample, dry weight (i.e., the weight in grams of the dry mussel tissue), duration (i.e., start date, end date and total amount of days that the mussels spent in water at the sample spot) and dry matter (i.e., percentage of dry weight in the sample before lyophilisation) were obtained for each sample. When there were two values for dry matter, a mean was taken from the two and used in the calculations. In addition, the following calculations were executed:

$$Mean\ dry\ weight = \frac{Sample\ dry\ weight}{Number\ of\ individuals\ in\ sample}$$

Equation 19: Mean dry weight

$$Mean\ wet\ weight = \frac{Mean\ dry\ weight}{Dry\ matter}$$

Equation 20: Mean wet weight

$$Start\ weight = 2.195\ g^{*}$$

Equation 21: Start weight in grams

$$Measured\ growth = Mean\ wet\ weight - Start\ weight$$

Equation 22: Measured growth

$$Measured\ mean\ growth = \frac{Measured\ growth}{Duration}$$

Equation 23: Measured mean growth

* *See 3.1.2.* Initial Mussel Weight.

Only data from seasons 2015 and 2018 were used in the DEB method validation since no other seasons contained values for duration. There were 77 sample spots that included duration in 2015 and 96 sample spots that included duration in 2018, comprising a total of 172 sample spots. Since several spots were sampled during both seasons, data from 2015 were handled separately from data from 2018 when processed in ArcGIS Pro. The data was imported to ArcGIS Pro with the function "Add x, y point data to the map," using the latitude and longitude of the RINBIO data to create point features (Figure 20).

Figure 20: Flowchart depicting the process of obtaining a point shapefile with measured mussel growth. Data downloaded from IFREMER's Surval database were used together with the soma weight of a 5 cm long mussel and DEB theory equations to calculate how much the mussels at each sample spot surveyed in the RINBIO project had grown during their submersion period (approximately three months). A point shapefile was created with a point for each sample spot and an attribute table with the measured growth at each spot.

3.3.1.2. Modelled Growth

3.3.1.2.1. Growth modelled in ArcGIS Pro

For the modelled growth of the accuracy assessment, chl *a*- and SST data from the RINBIO timeline were used as input variables in the DEB method (Figure 21) to model daily growth. This was done in ArcGIS Pro using the geoprocessing tool "Raster Calculator." The resulting files were three multiband rasters with daily growth: one with 212 bands for growth on dates January 1st 2015 – July 31st 2015, one with 2 bands for growth on dates December 30th 2017 – December 31st 2017 and one with 212 bands for growth on dates January 1st 2018 – July 31st 2018.

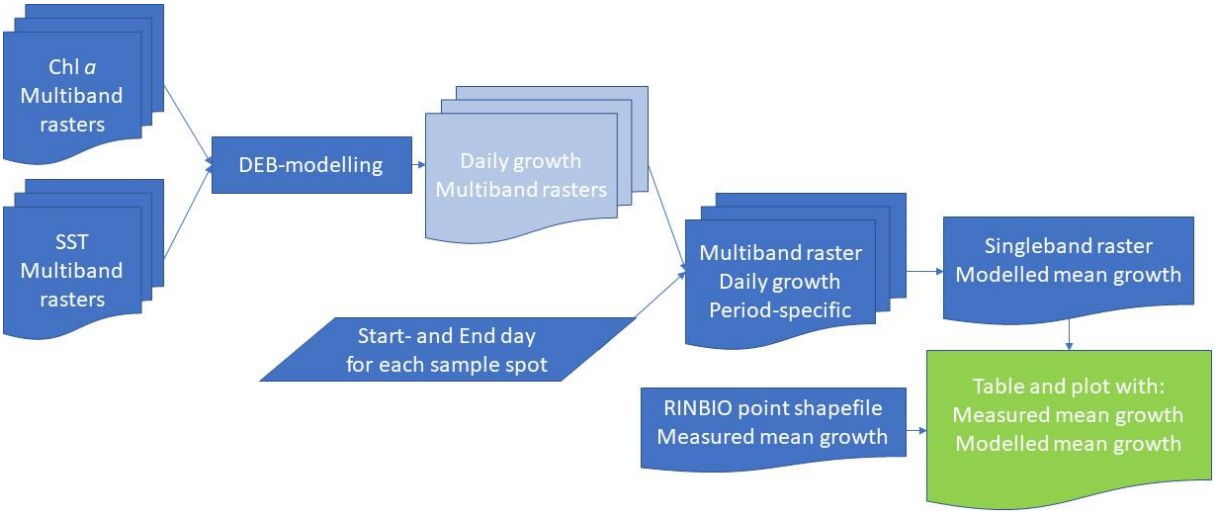

Figure 21: Flowchart depicting the work process in ArcGIS Pro to create an attribute table with Measured and Modelled mean RINBIO mussel growth (file marked in green). Chl a- and SST data were used as input parameters in a DEB equation executed in ArcGIS Pro to obtain multiband rasters with daily growth (lighter blue). For each RINBIO sample spot, the rasters for the days that the mussels were submerged were aggregated and a singleband raster with cell means obtained. Each raster thus represented the mean modelled growth during a particular submersion period. The mean modelled growth for each sample spot was extracted to a point shapefile with the sample spots and measured mean growth. The resulting shapefile contained one point for each sample spot and an attribute table including mean measured growth and mean modelled growth.

Many RINBIO sample spots were located close to shore and most fell outside of the area covered by the raster with modelled growth. At these sites, no growth value could be calculated, and they were therefore not used in the validation of the DEB method. A total of 27 sample spots were usable, 16 of which were sampled in 2015 and 26 in 2018. Hence, a combined total of 42 observations contained data used for the DEB method validation for values modelled in ArcGIS Pro.

The mussels measured had spent different amounts of time in the water at different sample spots, most likely since it is difficult to place or retrieve mussels from all sites in one day and the process had to be spread out over several days. Because of this, different periods of modelled growth had to be used depending on sample spot. The RINBIO data downloaded from Surval included both retrieval date and duration. Hence, it was possible to discern what days the mussels had been in the water at each spot.

First, multiband rasters with daily growth were created for all the time periods needed (Figure 21). The raster function "Extract Bands" was used to retrieve the correct days for each sample

spot and season. The result was one multiband raster per observation, where each band contained growth values for one day in the submersion period specific to the observation in question. The procedure was repeated until all observations had corresponding multiband rasters for correct submersion periods. Observations with identical time periods shared rasters.

Secondly, single-band rasters with mean growth were created for all time periods. The raster function "Cell Statistics" was used on each multiband raster to calculate the mean value (NoData excluded) for each cell. The resulting files were single rasters (one for each submersion period) containing modelled mean daily mussel growth.

Finally, mean growth from all single-band rasters were added to the RINBIO point shapefile created for measured values. The geoprocessing tool "Extract Multi Values to Points" was used to extract the values from all the single submersion period rasters and add them to the attribute table of the RINBIO point layer.

The resulting attribute table was exported as a CSV-file and imported to Excel for further processing. In Excel, the growth value for each observation was saved and remaining values were discarded. The process was executed with data from one sample season at a time (i.e., 2015 and 2017-2018 separately), and the resulting tables were then joined.

Modelled mean growth was compared to measured mean growth by plotting the values against each other with the measured data on the x-axis and the modelled data on the y-axis. Similarly, modelled growth was calculated by multiplying modelled mean growth with duration (Equation 24) and was then compared to measured growth in a scatter plot.

$$Modelled\ growth = modelled\ mean\ growth * duration$$

Equation 24: Modelled growth

3.3.1.2.2. Growth modelled in Excel

When growth was modelled in ArcGIS Pro, the resulting raster was positioned slightly differently than both the chl *a*-raster and the SST raster. Because of this, some of the RINBIO spots positioned within both chl *a*- and SST rasters fell outside of the growth raster. To obtain more data for modelled growth that was comparable to the measured growth at RINBIO spots, the growth was modelled a second time in a slightly different way as described below.

Sample spot number, longitude and latitude for all 173 RINBIO observations were composed into a table in Excel. The file was saved as a comma delimited CVS-file and imported to ArcGIS Pro as a table. The table was used in the geoprocessing tool "XY Table To Point" to create a point shapefile. A copy was made of the point shapefile. The original was designated data for season 2015 whereas the copy was designated data for season 2018. The geoprocessing tool "Extract Multi Values to Points" was used to add daily values for chl *a* and SST to the corresponding point shapefile. The resulting attribute tables were exported as CVS-files and opened in Excel, where modelled growth was calculated.

A total of 75 observations had data for both chl *a* and SST, of which 27 were from 2015 and 48 from 2018. The growth at each spot was calculated for the days that the mussels had been in the water at that specific spot. The initial values for W, V, E and R remained as specified in Equation 5, Equation 6, Equation 7 and Equation 8. Growth for the following days was calculated based on the values for W, V, E and R from the day before.

Total growth for each spot was obtained by subtracting the initial W from the final W. The modelled growth was then compared to the measured growth in a scatter plot with measured growth on the x-axis and modelled growth on the y-axis.

3.3.2. Precision

The chl *a*- *a*nd SST data that was processed in Excel and used for the DEB method validation were also used for the OAT analysis (Figure 22). By changing one DEB method parameter or constant at a time, and observing the change in output, the DEB method's model sensitivity could be assessed.

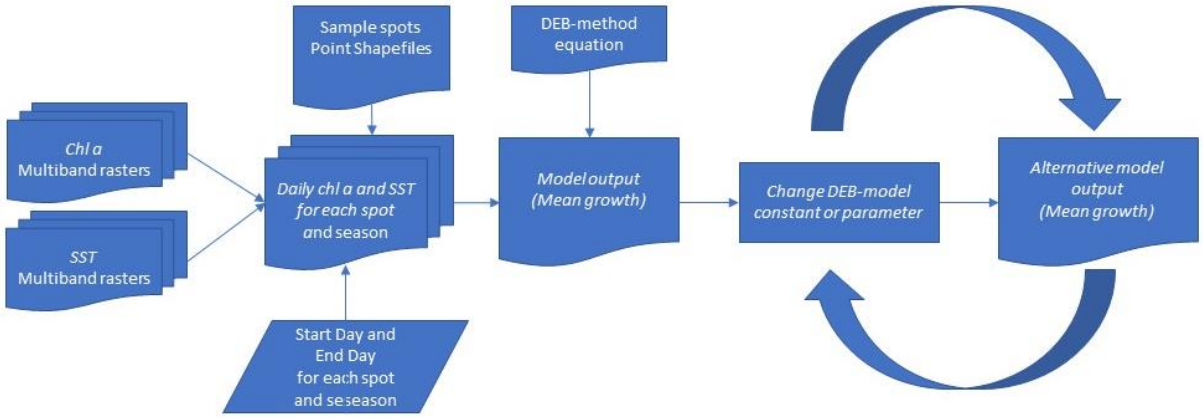

Figure 22: Workflow for the OAT-analysis. Chl a- and SST rasters were used to model DEB growth for each RINBIO observation. One DEB parameter at a time was changed and the subsequent change in output noted.

The input values that were deemed important to investigate due to known potential errors were the upper boundary of the tolerance range (T_H), the half saturation coefficient (X_k), the shape coefficient (δ_m), chl *a*, SST and the volume-specific maintenance cost ($[\dot{p}_M]_m$) (Table 1).

As mentioned in section, 3.1.3. Modelled Mussel Growth, a value of 303 K has been suggested for T_H and was therefore assessed in the sensitivity analysis.

As mentioned in section, 3.1.3. Modelled Mussel Growth, values as low as 28 mg C / m^3 and as high as 194 mg C / m^3 have been proposed for X_k. The higher value is used as initial value in the DEB equation. The impact of using the lower value was assessed in the sensitivity analysis.

As mentioned in section 3.1.2. Initial Mussel Weight, the values 0.333 and 0.287 have been proposed for δ_m in the literature as well as the value 0.250 used in the base model, climate

change scenarios and in situ validation of the present study. The impact of using the higher of the two former values was assessed in the sensitivity analysis.

The Root Mean Square Difference (RMSD) for each value in the original SST rasters is 0.408. To analyse the change caused by the SST RMSD, 0.408 was first added and then subtracted to all SST values and the output assessed. The same procedure, but with a RMSD of 0.266, was undergone for chl *a*. Resulting SST and chl *a* values < 0 were adjusted to 0.

In the present study as well as in Hatzonikolakis et al. (2017) and Casas and Bacher (2006), $[\dot{p}_M]_m$ is treated as a constant and set to 24 J/cm^3*day. However, $[\dot{p}_M]_m$ does change with temperature and Van der Veer et al. (2006) showed that, for species *M. edulis*, $[\dot{p}_M]_m$ takes the value of 13 at 10 °C and the value 26 at 20 °C. Therefore, the values 12 and 26 were assessed for $[\dot{p}_M]_m$.

Table 1 : Input values for the input factors used in the OAT analysis. Baseline values (mean values for parameters chl a and SST, and best value for T_H, $[\dot{p}_M]_m$, δ_m, and X_k) are indicated by a blue background.

Parameter	Best value or mean	Lowest value	Highest value
T_H (K)	296	296	303
X_k (mg C / m^3)	194	28	194
δ_m (no unit)	0.250	0.250	0.333
SST (K)	291.57	291.16	291.98
chl *a* (mg/m^3)	0.53	0.26	0.79
$[\dot{p}_M]_m$ (J / [day*cm^3])	24	12	26

For each parameter change, average values over all spots were calculated for measured growth, for growth considering starvation and for growth not considering starvation. The results, in the form of absolute change from baseline, were presented in a bar chart and is presented in the result section.

Scatter plots were created to visualise the relationship between measured and modelled growth for each parameter change. The impact on said relationship was considered positive if output R^2 increased, the gradient moved closer to 1 and the intercept of the y-axis moved closer to the origin, compared to the baseline values. The impact was considered negative if output R^2 decreased, the gradient moved further away from 1 and the intercept of the y-axis moved further away from the origin. A mix of the two scenarios was considered an ambiguous impact and very small changes (< 0.01) in R^2, gradient and/or intercept were considered negligible impacts.

The parameter found to cause the most precision loss was calibrated and validated as described in the respective sections below.

3.3.3. Calibration

3.3.3.1. Primary Calibration

The 75 GPCs from RINBIO were listed in Excel and, using the Excel function RAND, randomly assigned numbers between 0.0000 and 1.0000. The GCPs assigned numbers < 0.5 were used for calibration of the parameter chosen using the OAT-analysis and remaining GCPs were used for validation, resulting in 48 calibration GCPs and 27 validation GCPs. As seen in Figure 23 and Figure 24, the calibration GCPs were spread out over the study area in a similar manner as the validation GCPs. Calibration GCPs were slightly more present in the central parts of GoL and on the north-eastern coast of Corsica, whereas validation GCPs were present closer to Spain and around Marseille.

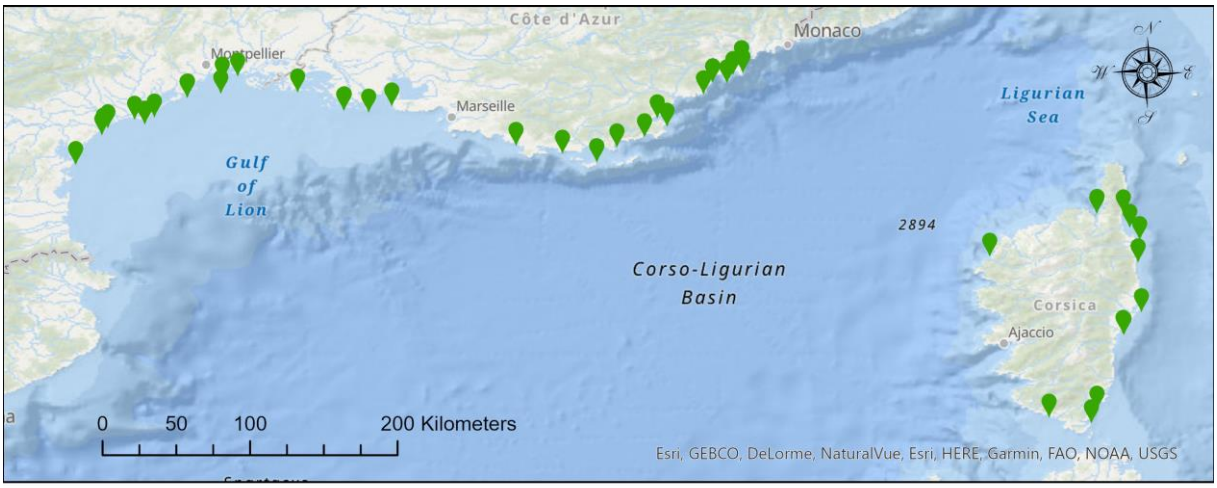

Figure 23: Locations of the 48 Ground Control Points (GCPs) used for calibration.

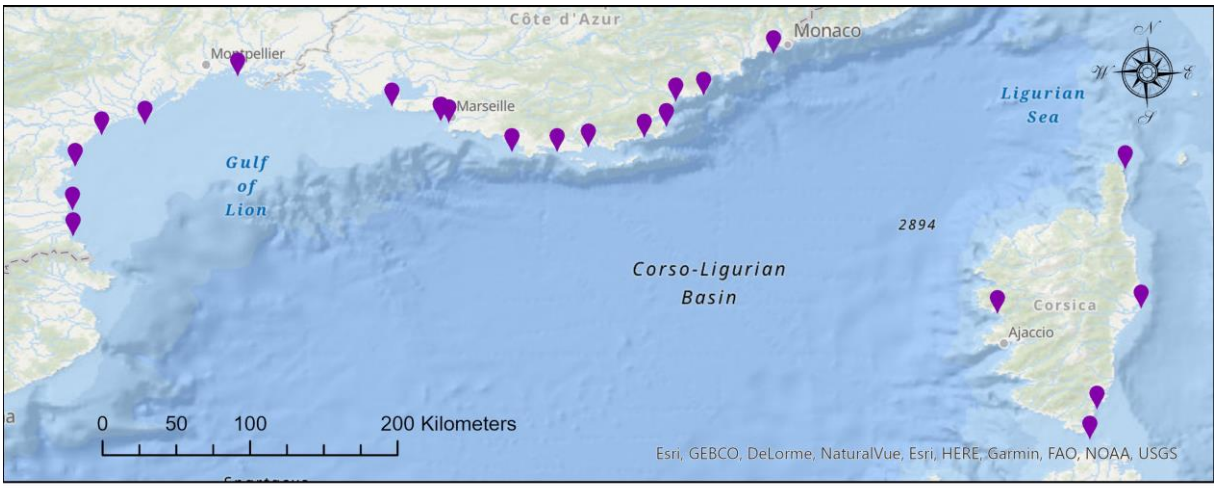

Figure 24: Locations of the 27 Ground Control Points (GCPs) used for validation.

The impact of X_k on model accuracy was investigated using the calibration GCPs. Measured values for the calibration GCPs were compared to the corresponding modelled values and graphed against each other with measured values on the x-axis and modelled values on the y-axis. The resulting values for R^2, slope and intercept of the y-axis were then graphed as a

function of different values for X_k. The X_k that resulted in the highest model accuracy was used for validation.

3.3.3.2. Primary Calibration

To further exclude risk of error attributed to the selection of GCPs, an alternative calibration was executed. For the alternative calibration, the 75 GCPs were once again listed in Excel and randomly assigned numbers between 0.0000 and 1.0000. This time, the 38 GCPs assigned the lowest numbers were used for calibration. The results of the two calibrations were then compared. If the value chosen for the parameter in question did not differ more than 10 % between the two calibrations, as indicated in Equation 25, then the value from the original calibration was considered correct and kept for validation.

$$\frac{Result\ of\ original\ calibration - Result\ of\ alternative\ calibration}{Result\ of\ original\ calibration}$$

Equation 25 : Difference between calibrations

3.3.4. Validation

The validation GCPs were used to validate the calibrated and adjusted DEB equation. Measured growth for each GCP (x-axis) was graphed against growth modelled with the calibrated and adjusted DEB model (y-axis). The model was validated if the validation values for R^2, slope and intercept erred no more than 0.3, respectively, from the calibration values.

3.3.5. Re-evaluation

A second OAT-analysis with the remaining parameters was performed on the adjusted DEB model to assess whether to calibrate additional parameters.

3.4. Definition of Areas Eligible for Mussel Cultivation

It is assumed that, in order for a mussel farm to be competitive on the European market, it needs to produce mussels at the same speed as, or faster than, its competitors. The current time requirement for growing *M. galloprovincialis* in Europe is 8-14 months, of which 3 - 8 months are the allotted frame for the mussels to grow from 5 cm to 8 cm in length (FAO 2021b). The minimum market size of 8 cm in length corresponds, according to Equation 5, to a tissue weight of 8.991 g per mussel, meaning that the mussel would need to grow at least 6.796 g after thinning and before harvest. For rapid growth, such that the mussels can be harvested 3 months after thinning, a mean growth of 0.076 g / day and mussel is needed. The common growth time of 8 months after thinning would require a mean growth of 0.028 g / day and mussel. An area can thus be considered eligible for mussel cultivation if the mean mussel growth is equal to or exceeds 0.028 g / day and mussel (hereafter referred to at 0.028 g / day).

As seen in Figure 25, larger mussels grow faster than smaller ones in optimal conditions, at least for mussels between 5 and 8 cm in length. This means that a 5 cm mussel that grows one day, even if it is ever so little, will simultaneously increase its growth rate capacity. The DEB model calculates growth based on an initial mussel length of 5 cm. Whereas it is technically

possible for the size parameters to be adjusted each day based on the growth rate the day before, limitations in skill and time hampered that option. Instead, a more conservative method was applied.

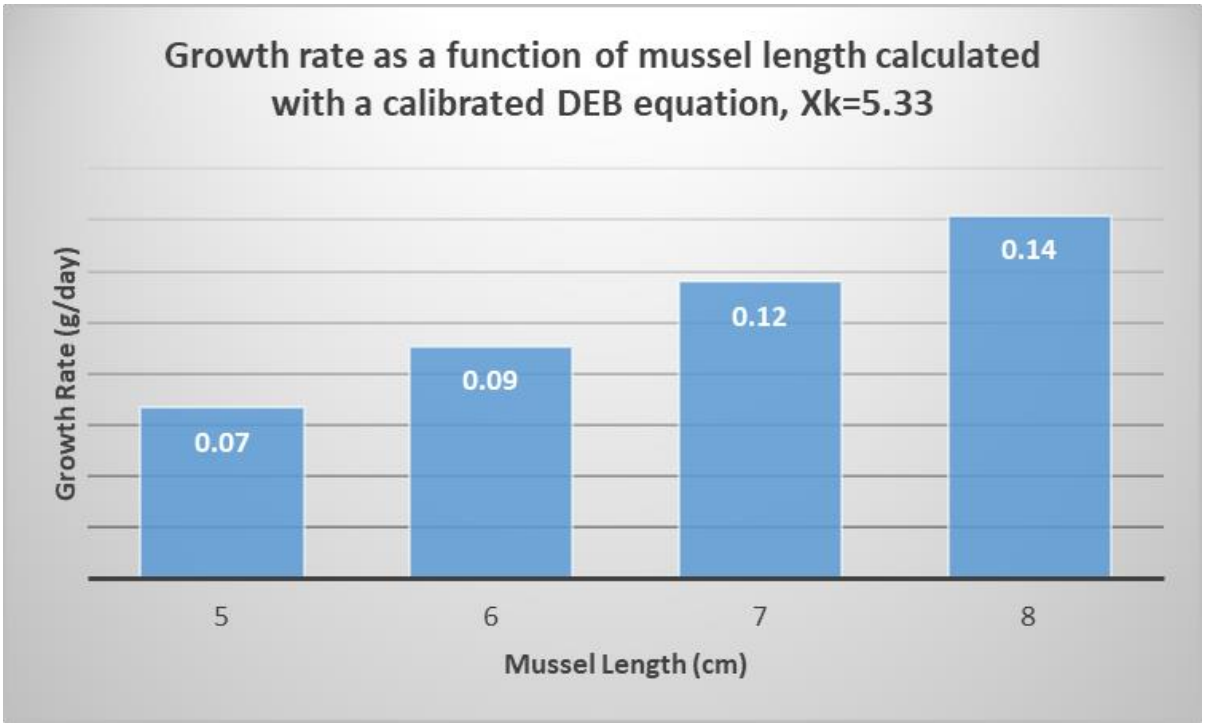

Figure 25: Growth rate as a function of mussel length. Between the lengths of 5 and 8 cm, larger mussels grow faster.

The mussels are harvested when they reach a length of 8 cm. This means that the modelled mussels are assumed to be in the water from the time that they are 5 cm in length and until they reach 8 cm. Growth rate was therefore calculated for each day using constant initial mussel lengths of 5 and 8 cm, respectively. Using the model with a constant mussel length of 5 cm depicts very well what day of the year a 5 cm mussel grows the fastest and what day it grows the least. It will, however, underestimate the true summed growth of a mussel over the entire year. Similarly, modelling mussel growth with an initial length of 8 cm is bound to result in overestimations. The true value lies somewhere in between. Daily growth of 8 cm mussels was modeled to provide a measure of maximum potential mussel growth. Since the objective was to map optimal mussel cultivation areas, however, only the areas suitable for 5 cm mussels were proposed as cultivation grounds.

For matters of clarification, it is important to mention that mussel growth fluctuates during the year and that it is possible to choose a time period with high growth to shorten the span of the post-thinning period (from 5 cm to harvesting). However, this would not necessarily be advantageous for mussel farmers since the entire growth period can span over more than a year and the mussels are in the water all year round. Hence, choosing a period with rapid growth for 5 cm mussels would result in less rapid growth for the mussels during earlier life stages. Since mussels tend to grow faster as they get larger, at least until they reach their size limit, it may well be in the interest of farmers to focus on fattening mussel spat (i.e., 2 cm long mussels)

during the periods with faster growth. In addition, mussels are eaten all year round, harvested all year round, and farmers benefit from the possibility of providing their goods to the market all year round. Therefore, the assumed growth period is all year (as opposed to a few months of the year) and the areas suitable for mussel cultivation are those areas that exhibit adequate mean yearly growth rates (as opposed to mean growth rates of i.e., the months with the highest growth).

3.5. Historical Growth

The multiband SST- and chl *a* rasters with daily values for 2011 - 2020 were used as input variables in the DEB equation and executed using Geoprocessing tool "Raster Calculator" in ArcGIS Pro to obtain multiband daily growth rate rasters for the decade.

The mean growth rate was modelled for visualization purposes for each year 2011 - 2020 for 5 and 8 cm mussels, respectively, and presented as maps. To investigate yearly variability in viable cultivation areas, the resulting rasters were reclassified into "suitable" and "unsuitable" areas for mussel farming and were also presented as maps. Cells with a mean yearly growth rate < 0.028 g / day were considered unsuitable and cells with a mean yearly growth rate ≥ 0.028 g / day were considered suitable.

Finally, the suitability for the entire time period 2011 - 2020 was visualized in one map. All yearly maps of suitable and unsuitable areas were juxtaposed, maps for 5 cm mussels as well as maps for 8 cm mussels. Cells that were suitable for mussel growth in every yearly map were considered suitable for the entire time period 2011 - 2020. Cells that were unsuitable for mussel growth in every yearly map were considered unsuitable for the entire time period 2011 - 2020. Cells that were sometimes suitable and sometimes unsuitable in yearly maps were considered potentially suitable for the entire time period 2011 - 2020.

3.6. Climate Change Scenarios

Suitability for mussel farming for future climate change scenario RCP 8.5 Long Term was assessed by investigating chl *a* and SST, individually.

3.6.1. SST

Growth rate as a function of SST at a stable optimal chl *a* of 80 mg chl *a* / m^3 was investigated for 5 and 8 cm mussels, respectively. This was done by calculating the growth rate at different SSTs and presenting the results as curves in a graph, as well as in a table depicting what SSTs resulted in a growth rate of ≥ 0.028 g.

The year during the IPCC reference period with the highest mean SST was found and used as baseline for modelling SSTs in scenario RCP 8.5 Long Term.

The prospective daily SSTs for RCP 8.5 Long Term were used to calculate mean monthly prospective SST and presented in maps, one for each month. The mean prospective SST for the entire year was also calculated and presented in a separate map.

The rasters with prospective SSTs for RCP 8.5 Long Term were reclassified so that all SSTs < 31 °C were given the value 0 and SSTs ≥ 31°C were given the value 1. The rasters were then juxtaposed and the values for each cell summed, resulting in a map depicting the number of days during the warmest year of RCP 8.5 Long Term that the SST is predicted to be ≥ 31 °C.

The number of days with less than optimal SSTs (< 5 °C and > 27 - < 31 °C) was modelled for RCP 8.5 Long Term. It was done in two ways: per month and per year. The rasters with prospective SSTs for RCP 8.5 Long Term were reclassified so that all SSTs < 5 °C and > 27 - < 31 °C were given the value 0 and SSTs 5 - 27 °C were given the value 1. The rasters were then juxtaposed according to time period (i.e., month or year) and the values for each cell summed, resulting in maps depicting the number of days during the warmest year of RCP 8.5 Long Term that the prospective SST is less than optimal.

In line with the objective of finding suitable farming areas without including potentially unsuitable ones, a conservative estimation of viable areas was made such that only areas whose prospective SSTs are exclusively within the optimal SST range may be considered for mussel cultivation.

1.1.1. Chl a

Growth rate as a function of chl a at a stable optimal SST of 292.15 K (19 °C) was investigated for 5 and 8 cm mussels, respectively, and the results presented in a graph, as well as in a table depicting what levels of chl *a* resulted in a growth rate of ≥ 0.028 g.

For reasons of clarity and visualization, all available high quality chl *a* data from the region, stretching from year 1998 to 2020, was utilized to map the mean number of days per year when chl *a* levels exceeded the concentration needed for a growth of at least 0.028 g / day.

3.7. IMTA Scenario

To test whether mussel cultivation as a part of IMTA is feasible, it was investigated whether locating a mussel cultivation close to a fish culture would sustain the mussels enough to grow at least 0.028 g / day.

The DEB model was used to test if a Phyto-C level of 28.9 mg C / m^3 (corresponding to 0.578 mg chl *a* / m^3) is enough to sustain a mussel growth of 0.028 g / day, since Modica et al. (2006) showed that the mean Phyto-C downstream of a Mediterranean fish pen was 31.8 mg C / m^3 in the spring and 26.0 mg C / m^3 in the summer, the mean of which is 28.9 mg C / m^3.

A constant chl *a* of 0.578 mg / m^3 was used together with SSTs rasters from years 2011 - 2020 to model mussel growth in an IMTA scenario. The resulting map was analysed to assess what areas, if any, are eligible for mussel cultivation as part of an IMTA. Areas where modelled growth was equal to or exceeded 0.028 g / day were considered capable of sustaining mussel cultivation as part of an IMTA whereas areas where growth was less than 0.028 g / day were not considered capable of sustaining mussel cultivation as part of an IMTA.

3.8. Combined Scenarios

3.8.1. Historical Growth and Climate Change

When considering locations for developing offshore mussel farms, it is imperative to limit propositions to areas that are both viable at the moment (as judged by historical data form the last decade) and that will continue to be viable for the foreseeable future, which currently stretches to the end of the 21st century.

The areas proposed in the present study comprise those locations that *i*) were considered suitable for cultivation during period 2011 - 2020 and *ii*) are expected to stay within the range for optimal SST for another 80 years, even for the climate change predictions with the largest temperature change (i.e., RCP 8.5 Long Term).

The raster depicting suitable areas 2011 - 2020 was used as a mask to clip the raster depicting suitable areas for scenario RCP 8.5 Long Term, resulting in a map depicting only areas that both were suitable 2011 - 2020 and also are predicted to be suitable in scenario RCP 8.5 Long Term.

3.8.2. IMTA and Climate Change

The impact of climate change on the possibility to farm mussels in an IMTA was investigated by modelling mussel growth using a constant chl *a* level of 0.578 and the daily prospective SST rasters for climate change scenario RCP 8.5 Long Term.

Monthly and yearly mean prospective growth for an IMTA scenario on climate change scenario RCP 8.5 Long Term were calculated and presented in maps. The resulting rasters were then reclassified to suitable (i.e., growth rate $\geq$ 0.028 g / day) and unsuitable (i.e., growth rate $<$ 0.028 g / day) and the results were once again presented in maps.

3.9. Growth Rate Variability in the Optimal Zone

To better understand and visualize the growth pattern in the optimal growth zone, the growth rate variability in the optimal zone was graphed for the entire period 2011 - 2020 for 5- and 8 cm mussels, respectively. The mean growth rate for each day and mussel size in the study area was extracted from the data sets to text (*.TXT) files using the ArcGIS Pro Geoprocessing tool "Band Collection Statistics." A small amount of formatting was needed in software Notepad (Microsoft Corporation 2021b) before the data could be correctly imported to Excel.

In addition, each year was graphed independently and presented together with other years to show the monthly variability. For correct comparison between loop years and non-loop years, data for February 29th was excluded from years dividable by 4 (i.e., 2012, 2016 and 2020).

4. Results

4.1. Model Assessment

4.1.1. Accuracy

4.1.1.1. Growth modelled in ArcGIS Pro

The results from the in situ validation with growth modelled in ArcGIS Pro are presented in the scatterplots in Figure 26. The R^2 for the comparison between measured and modelled mean growth is 0.5907 and the R^2 for the comparison between measured and modelled growth is 0.4131.The gradient is 0.4933 for measured vs. modelled mean growth and 0.4584 for measured vs. modelled growth. The intercept of the y-axis is -0.0218 for measured vs. modelled mean growth and -1.89 for measured vs. modelled growth. Hence, the modelled growth did not fall within 50 % of the measured growth modelled in ArcGIS Pro and the baseline model was not considered sufficiently accurate.

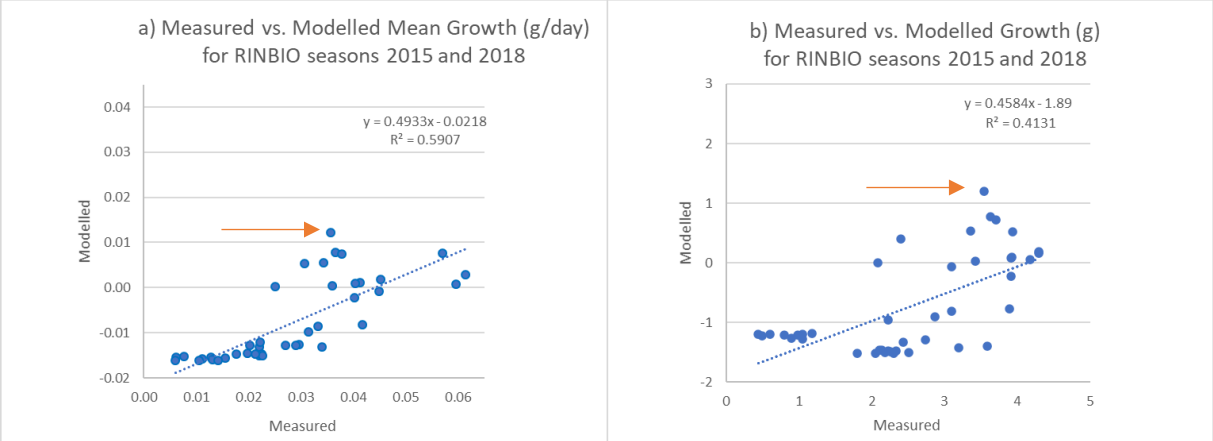

Figure 26: Scatter plots comparing measured growth and measured mean growth to modelled growth and modelled mean growth, respectively, with modelling done in ArcGIS Pro. The plots include 42 points, each representing a comparison between modelled and measured growth or mean growth. Measured growth is the growth observed in the mussels sampled at one sample spot during either 2015 or 2018. The plots thus include observations from both years. Measured mean growth is the measured growth divided by the number of days the mussels were in the water, a value that varies between observations. Modelled mean growth is the mean daily weight increase that a mussel is predicted to have, according to the DEB method, when being submerged at a sample spot for a certain time. Ex: The points marked with orange arrows has a modelled mean growth of 0.01219 g / day and a measured mean growth of 0.03574 g / day. The mussels for this observation were submerged at sample spot 38094019 (Port-Saint-Louis-du-Rhône) for 99 days. They were put in the water on April 5th2018 and collected on July 13th 2018. The measured growth is calculated by measuring the mussels before and after submersion. The modelled growth for this observation is the growth calculated from chl a- and SST data using DEB-model calculations for spot 38094019 during the period April 5th 2018 - July 13th 2018.

4.1.1.2. Growth modelled in Excel

The results from the in situ validation with growth modelled in Excel are presented in the scatterplots in Figure 27. The R^2 for the comparison between measured and modelled growth is 0.3923, the gradient is 0.2737 and the intercept of the y-axis is -1.4059. Hence, the modelled growth did not fall within 50 % of the measured growth modelled in Excel and the baseline model was not considered sufficiently accurate.

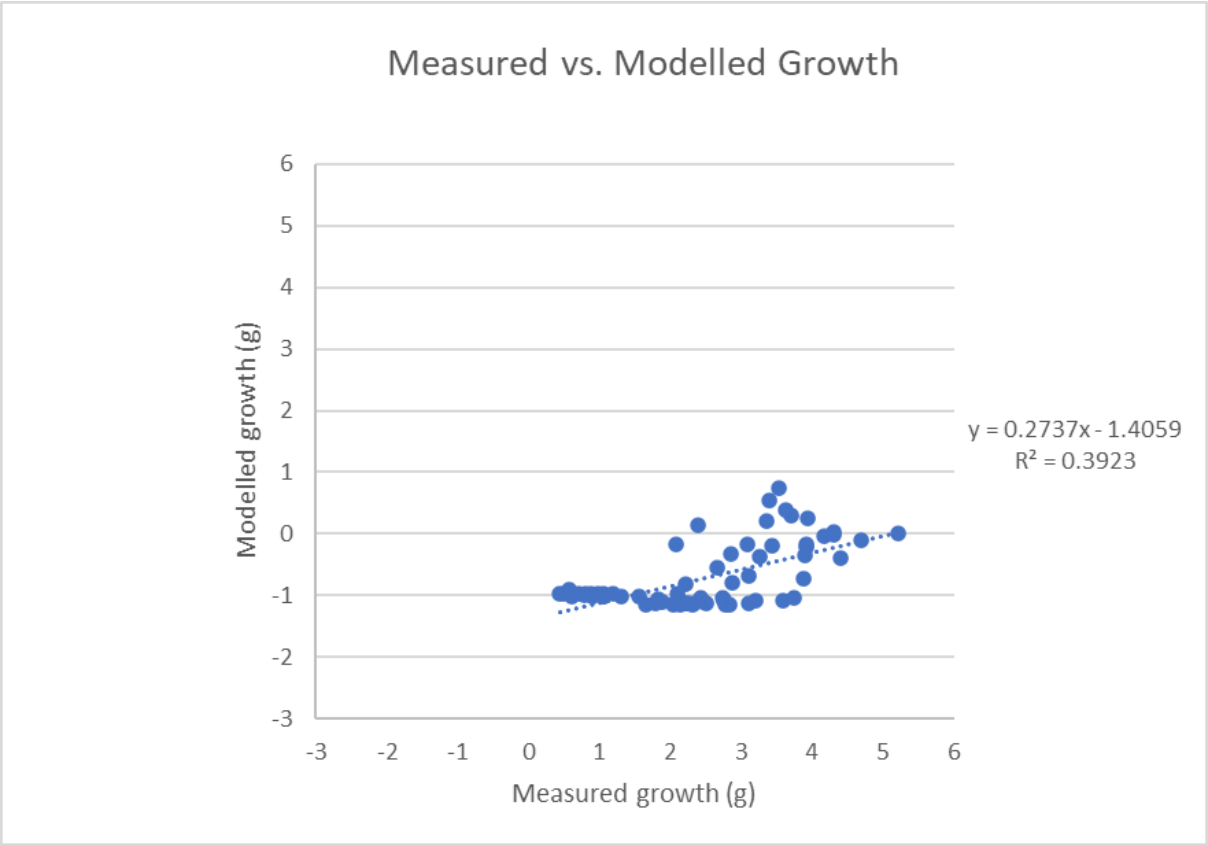

Figure 27: Scatter plot comparing measured growth to growth modelled in Excel. A total of 75 comparisons of measured vs. modelled growth from seasons 2015 and 2018 are depicted in the plot, with each comparison represented by a point.

4.1.2. Precision

The total range of change in output for modelled growth varies from 0.0092 g for SST to 1.2918 g for X_k (Figure 28). Additional values are 1.2524 g for δ_m, 0.6486 g for $[\dot{p}_M]_m$, 0.4140 g for chl *a* and 0.1751 for T_H.

This is to be compared to the total range of growth modelled in excel, where the difference between the lowest and the highest modelled growth is 1.9058 g. Growth modelled in Excel varies between -1.1548 g and 0.7510 g with a mean of -0.7409 (Figure 27).

It is also to be compared to the absolute difference between measured growth and growth modelled in Excel, which varies between 1.4178 g and 5.1915 g with a mean of 3.1706 g.

The only parameter that has an impact on the output for measured growth is δ_m (2.9924 g). Mean measured growth for a δ_m of 0.333 is -0.5627 g, to be compared with the baseline value of 2.4297 g for a δ_m of 0.250 (Figure 29).

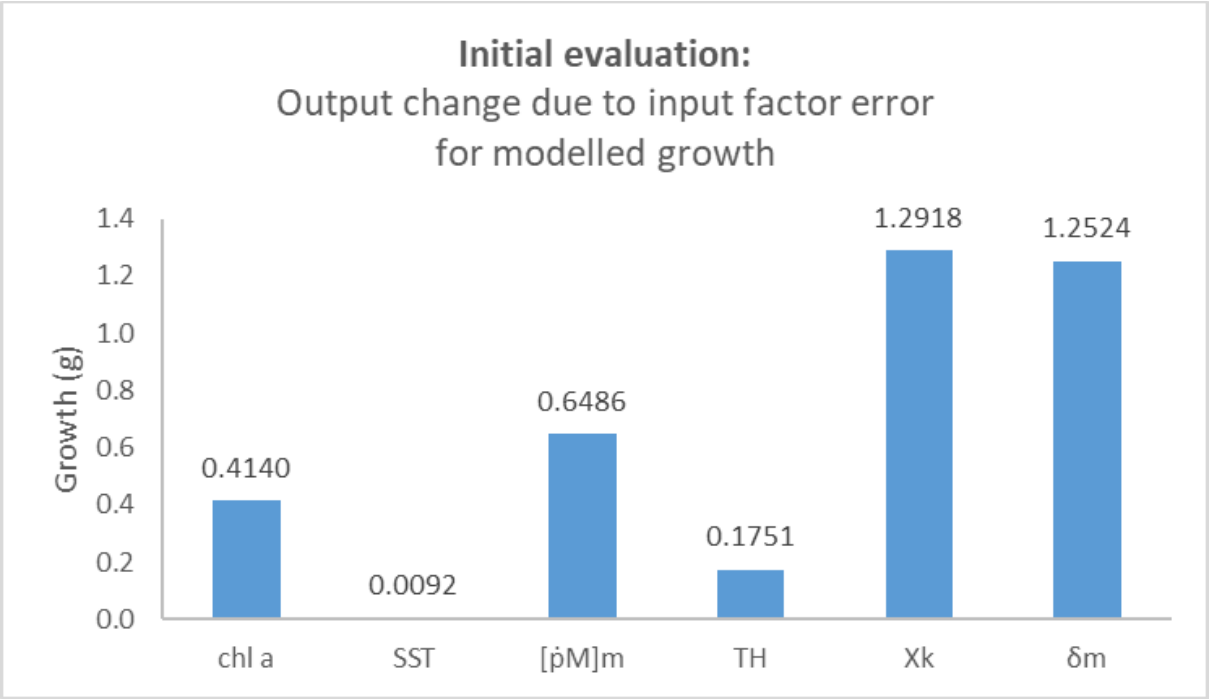

Figure 28: OAT-analysis results for DEB-model variables and constants presented as a column chart with the maximum absolute output change for each input factor. The output considered is modelled growth.

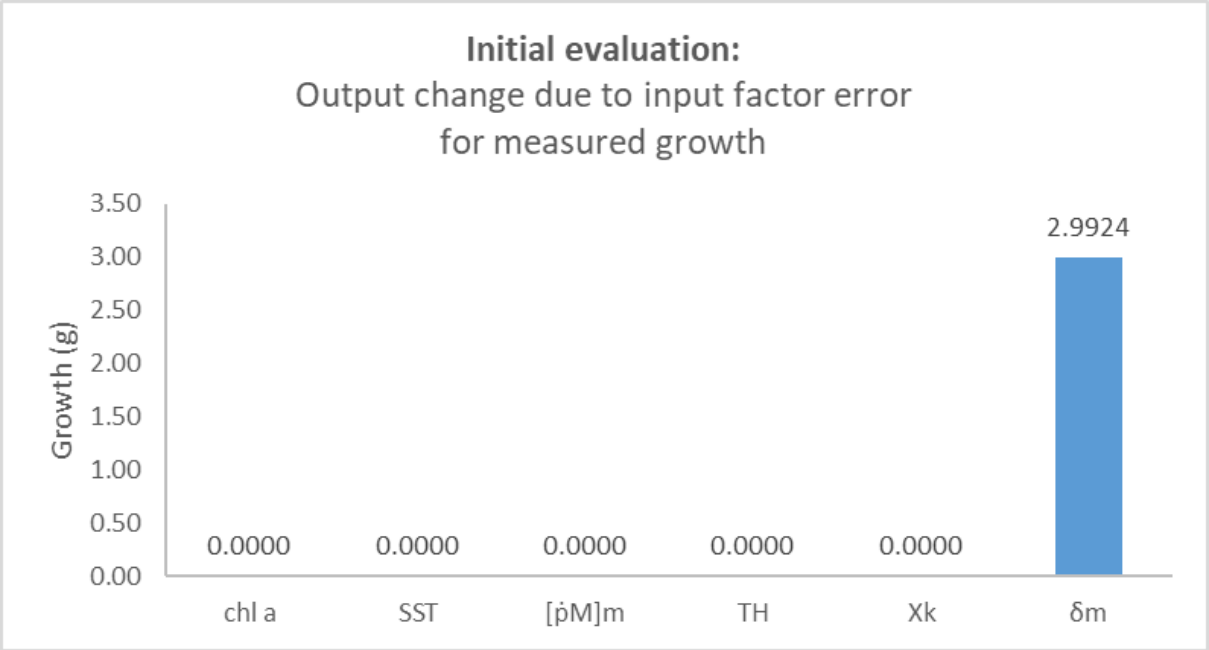

Figure 29: OAT-analysis results for DEB-model variables and constants presented as a column chart with the maximum absolute output change for each input factor. The output considered is measured growth, which is impacted since DEB theory is used to estimate initial mussel wet weight from mussel length.

The relationships between measured and modelled growth for the OAT-analysis parameter changes are presented in Figure 30. Output values are compared to the output values for growth modelled in Excel: 0.3923 for the R^2, 0.2737 for the slope and -1.4059 for the intercept.

The lowest values for T_H and δ_m, as well as the highest value for X_k are the same as in the baseline equation and using them thus causes no change output. Using the highest value for T_H worsens R^2 (to 0.3536), improves the slope (to 0.3171) and worsens the intercept (to -1.6864).

Using the highest value for δ_m worsens the R^2 (to 0.3582), improves the slope (to 0.4621) and worsens the intercept (to -1.7333). Using the lowest value for X_k improves the R^2 (to 0.5314) and the slope (to 0.8888) but worsens the intercept (to -1.6086).

Subtracting one RMSD from all chl *a* values worsens the R^2 (to 0.3338), the slope (to 0.2320) and the intercept (to -1.4604). Adding one RMSD to all chl *a* values improves the R^2 (to 0.4110), worsens the slope (to 0.2648) and improves the intercept (to -1.1260).

Subtracting one RMSD from all SST values slightly improves the R^2 (to 0.3883), slightly worsens the slope (to 0.2733) and slightly worsens the intercept (to -1.4090). Adding one RMSD to all SST values slightly improves the R^2 (to 0.3963), slightly worsens the slope (to 0.2736) and slightly improves the intercept (to -1.4005).

Using the lowest value for $[\dot{p}_M]_m$ improves the R^2 (to 0.4435), the slope (to 0.3534) and the intercept (to -1.0283). Using the highest value for $[\dot{p}_M]_m$ worsens the R^2 (to 0.3848), the slope (to 0.2625) and the intercept (to -1.4559).

To summarise, ambiguous impact on measured vs. modelled growth was found when using the highest values for T_H and δ_m, when using the lowest value for X_k and when one RMDS was added to chl *a* values. Negative impact was found when one RMDS was subtracted from chl *a* values and when using the highest value for $[\dot{p}_M]_m$. Negligible impact was found when one RMSD was added to or subtracted from SST values. Positive impact was found when using the lowest value for $[\dot{p}_M]_m$.

When comparing the results for δ_m and X_k, the change in the latter results in a better R^2, a better gradient and a better intercept than the former. In addition, the highest change in output in modelled growth was for X_k. Therefore, X_k was the parameter chosen for calibration.

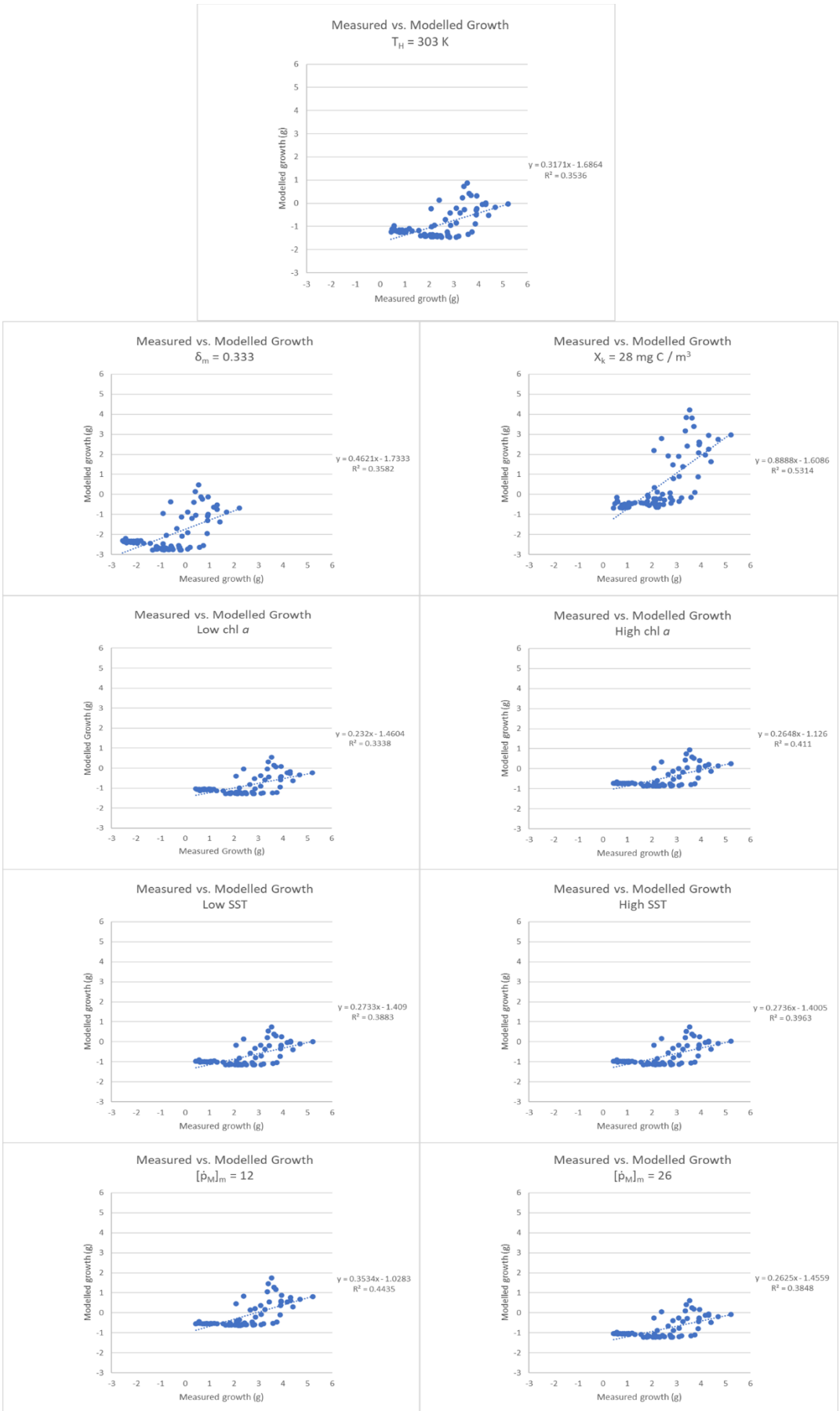

Figure 30 : Scatter plots of the relationship between measured (x-axis) and modelled growth (y-axis) for different values of parameters δ_m, X_k, chl a, SST and $[\dot{p}_M]_m$.

4.1.3. Calibration

4.1.3.1. Primary Calibration

The values for R^2, slope and intercept of the y-axis as functions of X_k for the original calibration with 48 GCPs are presented in Figure 31. The R^2 value increases from below 0.2 at an X_k close to 0, to just over 0.7 at an X_k of 2. For X_k values above 2, the R^2 value decreases very slightly and stays close to 0.7. The value for the curve representing the slope increases from below zero to just above 1.2 for X_k values between close to 0 and 10. The Intercept decreases from just above 5 for an X_k of close to 0 to just below 0.2 for an X_k of 10.

Above values of 2, the X_k only had a minor impact on R^2. Hence, the R^2 did not play a large role in deciding what X_k to use when adjusting the DEB equation. The main choice was between calibrating the model for a slope value of 1, an intercept value of 0, or a compromise between the two. An intercept value of 0 was deemed more important, which was reflected by the X_k value used when adjusting the DEB equation.

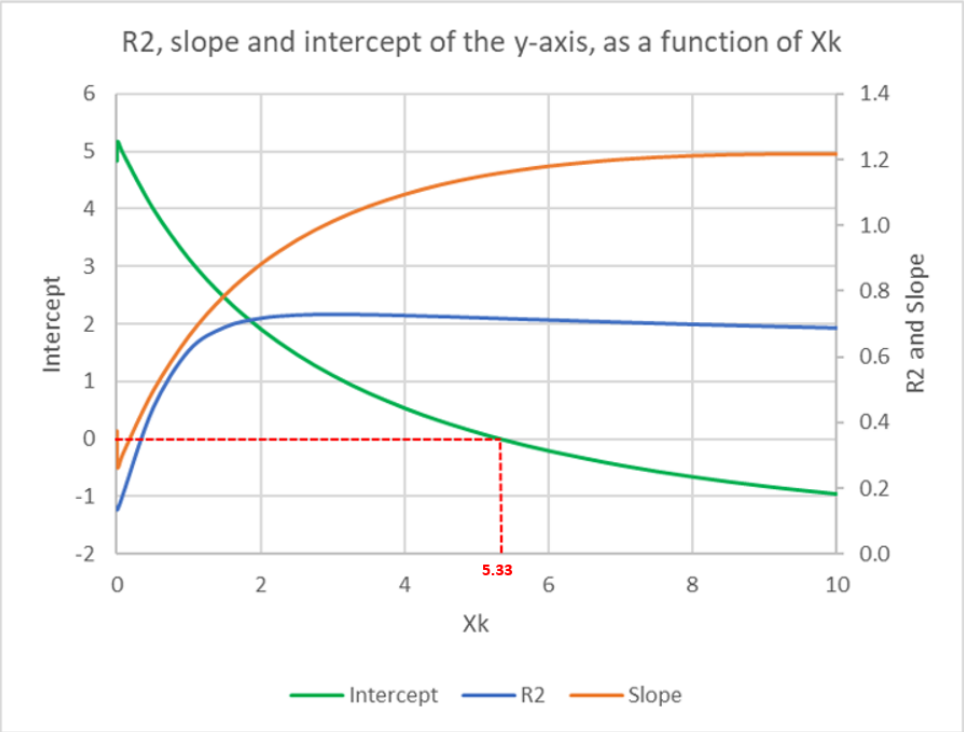

Figure 31: R^2, slope and intercept as a function of X_k for the 48 GCPs used for the original calibration.

An X_k value of 5.33, corresponding to a value of 0.0041 for the intercept of the y-axis, was used for adjusting the DEB equation, resulting in an R^2 of 0.716 and a slope of 1.1602 (Figure 32).

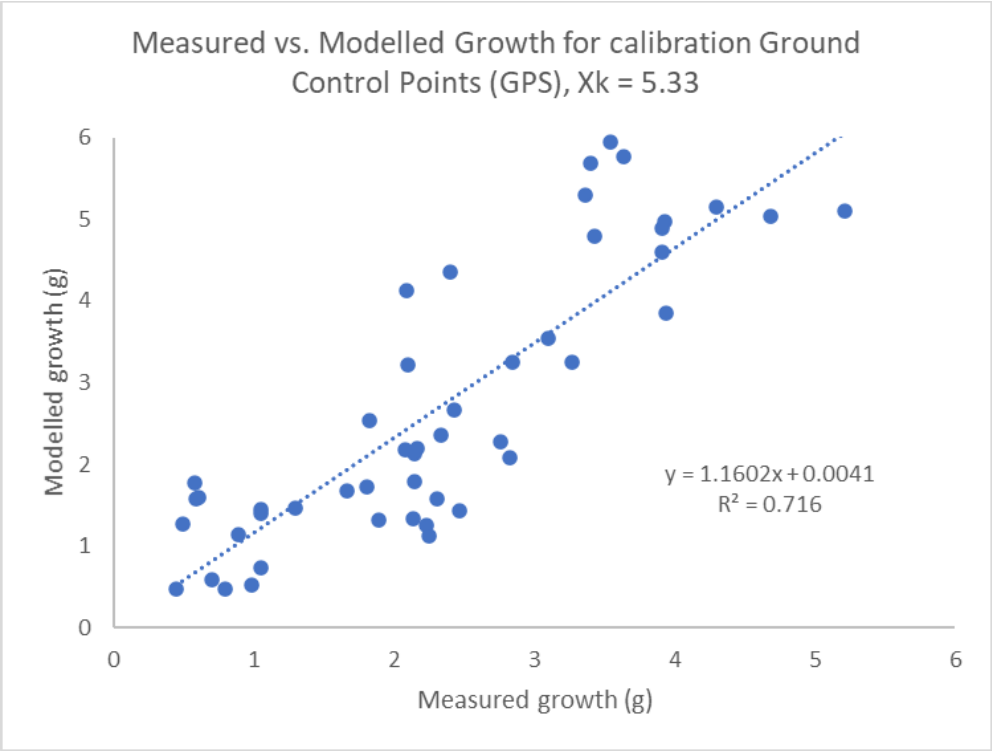

Figure 32: Measured vs. modelled growth for calibration Ground Control Points (GCPs).

4.1.3.2. Alternative Calibration

The alternative calibration resulted in a corresponding X_k value of 5.11 (Figure 33), or 4 % less than the result from the original calibration. Hence, the value of 5.33 from the original calibration was kept for validation.

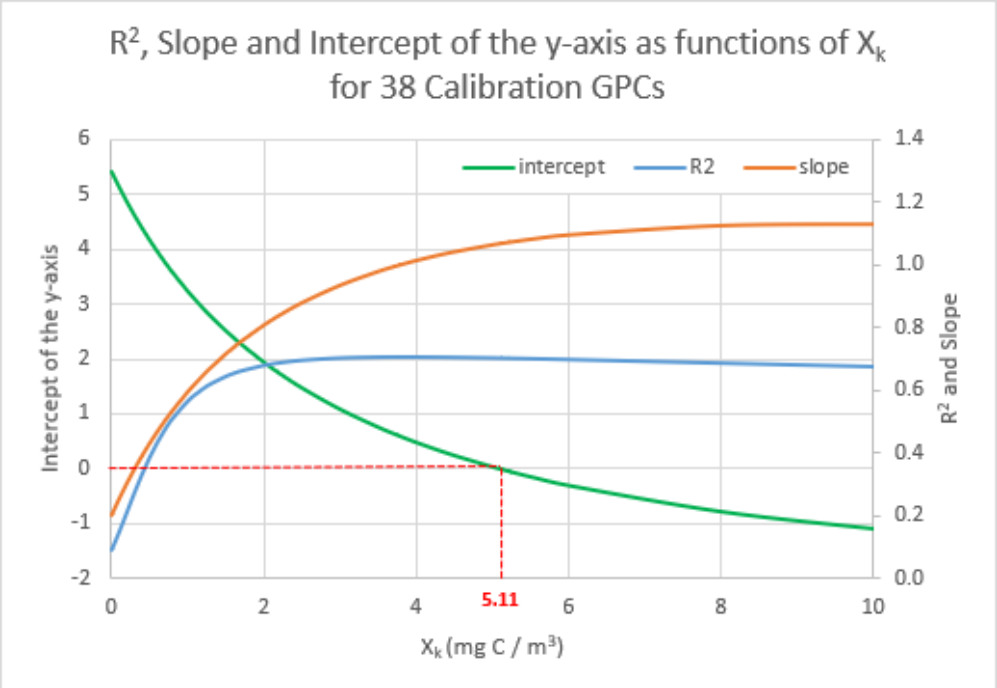

Figure 33: R^2, slope and intercept as functions of X_k for the 38 GCPs used for the alternative calibration.

4.1.4. Validation

Measured values (x-axis) vs. values modelled with the adjusted DEB equation (y-axis) for the 27 validation GCPs are presented in Figure 34. The R^2 value for the curve is 0.5735, the slope 0.8658 and the intercept 0.1642. That corresponds to a 0.143 lower R^2 value, a 0.29 lower slope and a 0.1601 higher intercept compared to the calibration. Hence, the calibration was validated.

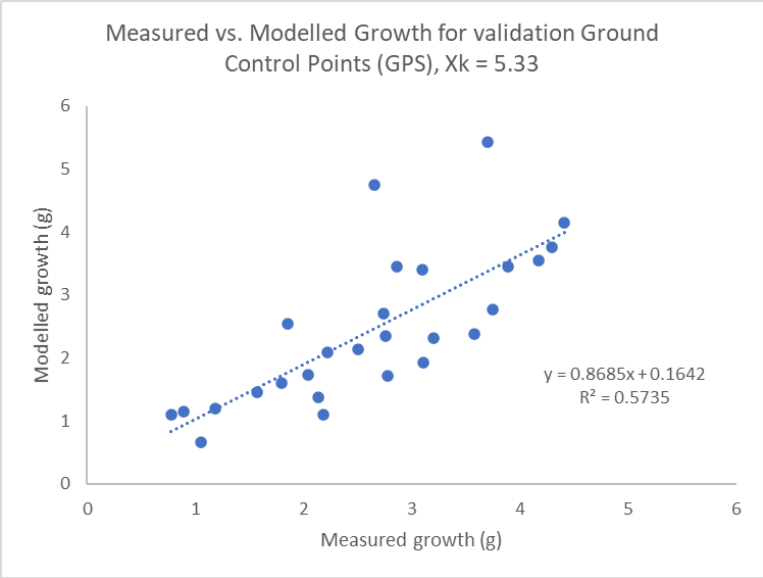

Figure 34: Measured vs. modelled growth for validation Ground Control Points (GCPs).

4.1.5. Re-evaluation

The adjusted DEB model was evaluated by an accuracy assessment modelled in Excel (Figure 35). The resulting R^2 was 0.6414, the slope 1.042 and the intercept of the y-axis 0.0721. The model was hence sufficiently accurate.

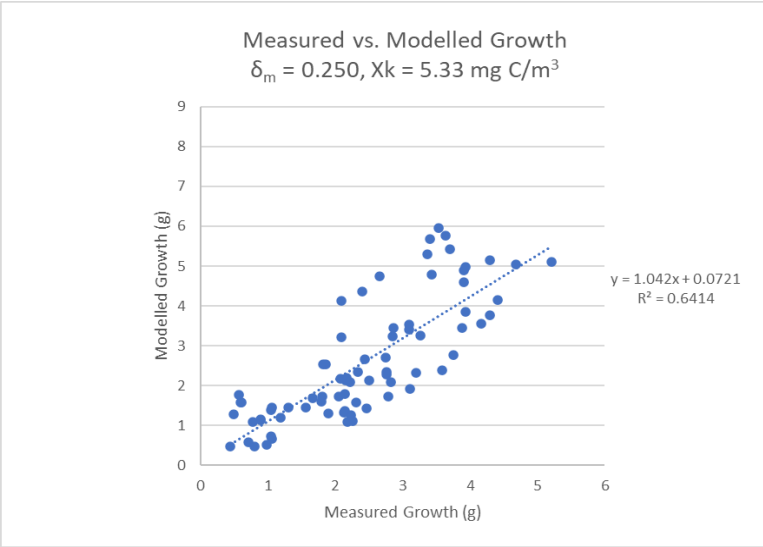

Figure 35: Accuracy assessment of adjusted DEB model executed in Excel and using 75 GCPs.

To investigate whether the model accuracy could be further ameliorated, a second OAT-analysis was performed with the adjusted DEB model (Figure 36). The results showed that chl

a was the parameter causing the largest change in modelled growth (3.8105 g), followed by $[\dot{p}_M]_m$ (1.3782), δ_m (0.9033), T_H (0.6360) and finally SST (0.0163). Only δ_m caused a change in measured growth (2.99 g).

These values are to be compared to the total range of modelled growth, which is 5.4747. The minimum, mean and maximum modelled growths are 0.4711 g, 2.6037 g and 5.9458 g, respectively. In addition, the minimum, mean, and maximum measured growths are 0.4436 g, 2.4297 g and 5.2089 g, respectively.

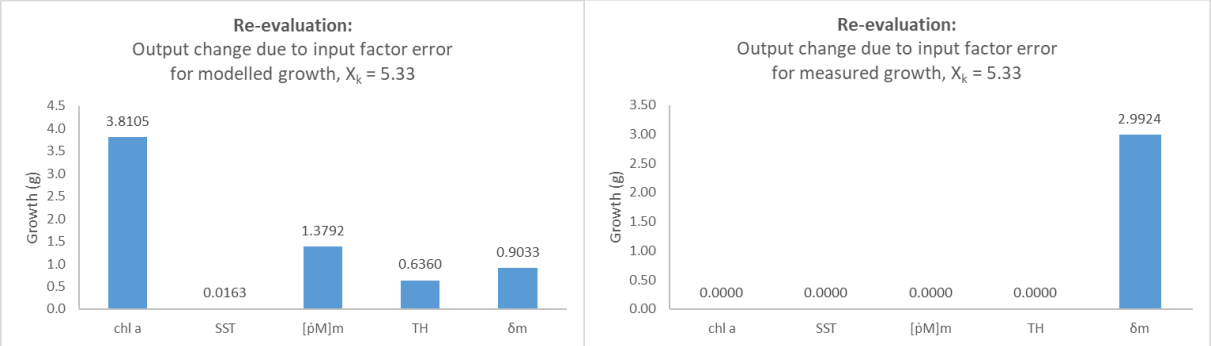

Figure 36: Change in growth due to input factor sensibility.

Although important for model precision, chl *a* is derived from reliable third party raster data and cannot be calibrated. SST causes very little change in model output and need no further investigation. The impact of changes in $[\dot{p}_M]_m$ and δ_m on model accuracy was investigated and the results presented in Figure 37.

A high value for T_H resulted in worsened R^2 (0.6162), slope (1.3917) and intercept (-0.1418). A high value for δ_m resulted in worsened R^2 (0.6375), slope (1.6195) and intercept (4.4184). A low value for $[\dot{p}_M]_m$ resulted in an improved R^2 (0.6534) but worsened slope (1.234) and intercept (0.8111). A high value for $[\dot{p}_M]_m$ resulted in a worsened R^2 (0.6388) but improved slope (1.0133) and intercept (-0.0318).

Thus, ambiguous impacts were found for high and low $[\dot{p}_M]_m$ values, whereas negative impact was found for a high values of δ_m and T_H.

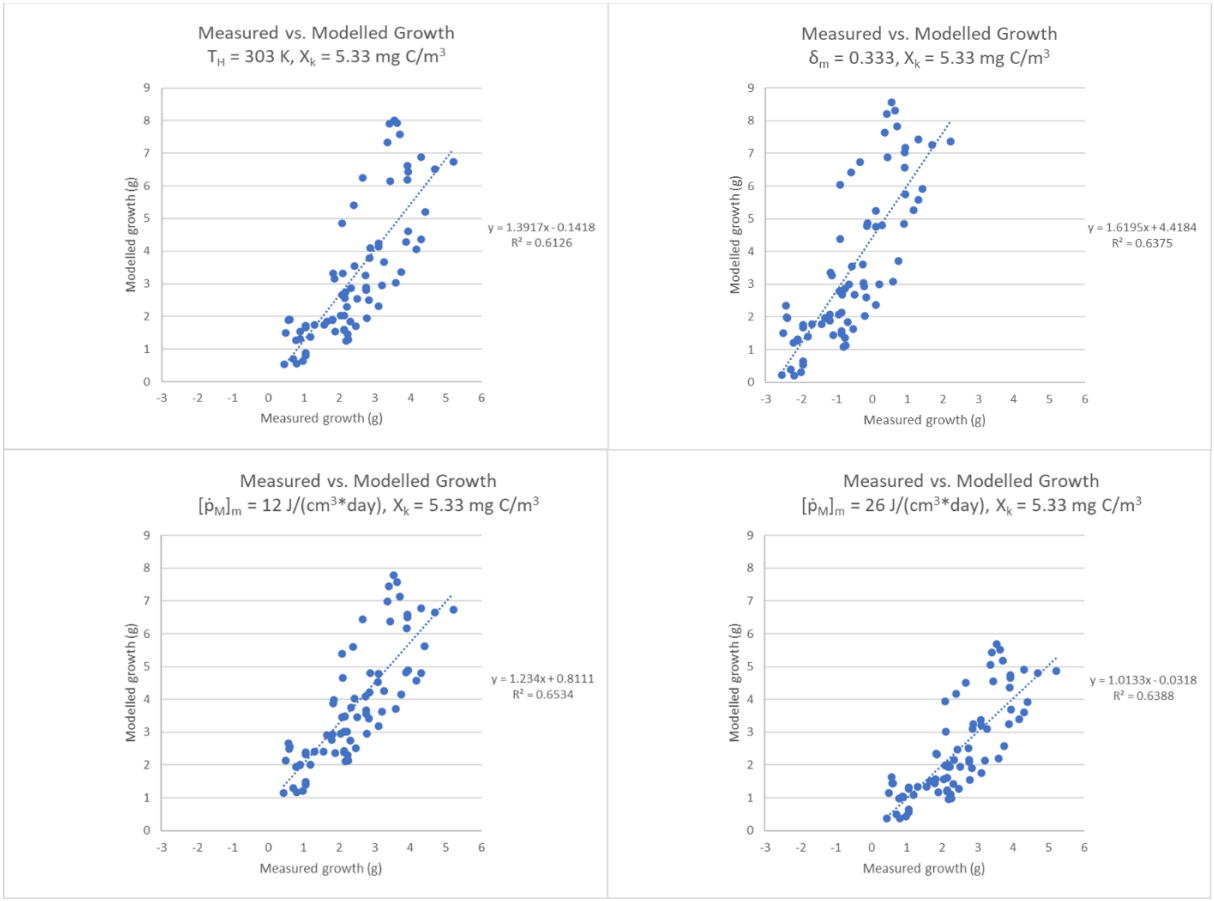

Figure 37: Accuracy assessments for the OAT-analysis parameter changes based on 75 GCPs.

The impact of $[\dot{p}_M]_m$ and δ_m on measured growth vs. growth modelled with the adjusted DEB model was investigated. For $[\dot{p}_M]_m$ (Figure 38), R^2 changes little but is at its highest (0.7060) at $[\dot{p}_M]_m$ value 12, the intercept is closest to 0 (0.0271) at a $[\dot{p}_M]_m$ value of 22 and the slope is closest to 1 (0.9937) at a $[\dot{p}_M]_m$ value of 30.

The baseline value of $[\dot{p}_M]_m$ is 24. Increasing it would result in a superior slope but an inferior intercept. Decreasing it slightly would result in an inferior slope but a superior intercept. Decreasing it more than slightly would result in inferior slope and intercept. Adjusting $[\dot{p}_M]_m$ would hence not result in an unambiguous improvement of the model accuracy and the parameter was therefore not adjusted.

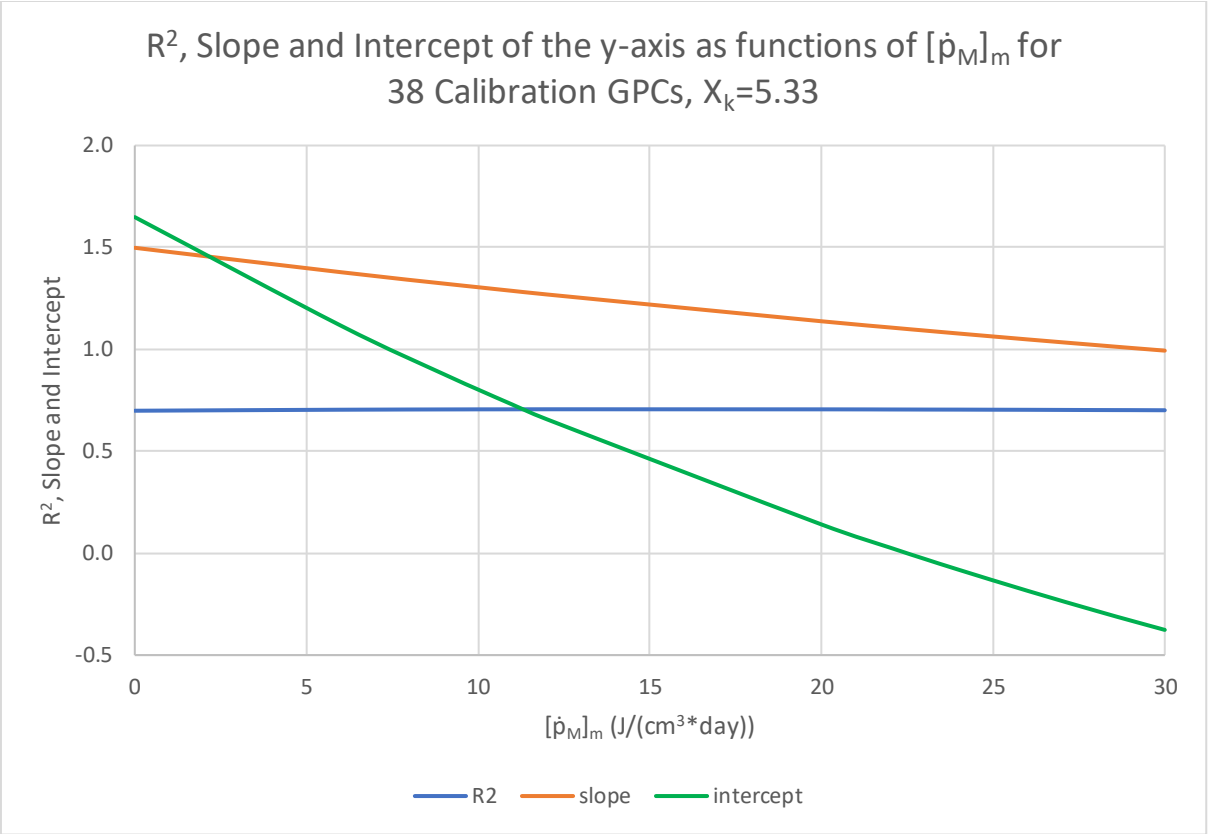

Figure 38: R^2, slope and intercept of the y-axis as functions of different values for $[\dot{p}_M]_m$, based on the 38 randomly chosen GCPs used for the alternative calibration.

For δ_m (Figure 39), the value for R^2 changes little throughout the graph but reaches a maximum of 0.7071 at shape coefficient value 0.333. The change in slope is slightly steeper than for R^2, starts at 0.7818 at shape coefficient value 0, then increases to 1.0021 for shape coefficient value 0.238, and continues to rise to 1.7339 at shape coefficient value 0.340. The intercept has the steepest curve of the three. It has value -0.784 at a shape coefficient value of 0, increases to 0 (-0.0063) at shape coefficient value 0.253, then continues to increase to a value of 5.0068 at shape coefficient value 0.340.

The baseline value for δ_m is 0.250. Decreasing it slightly would result in a superior slope but an inferior intercept. Decreasing it more than slightly would result in inferior slope and intercept. Increasing it slightly would result in an inferior slope and a superior intercept. Increasing it more than slightly would result in inferior slope and intercept. Adjusting δ_m would hence not result in an unambiguous improvement of the model accuracy and the parameter was therefore not adjusted.

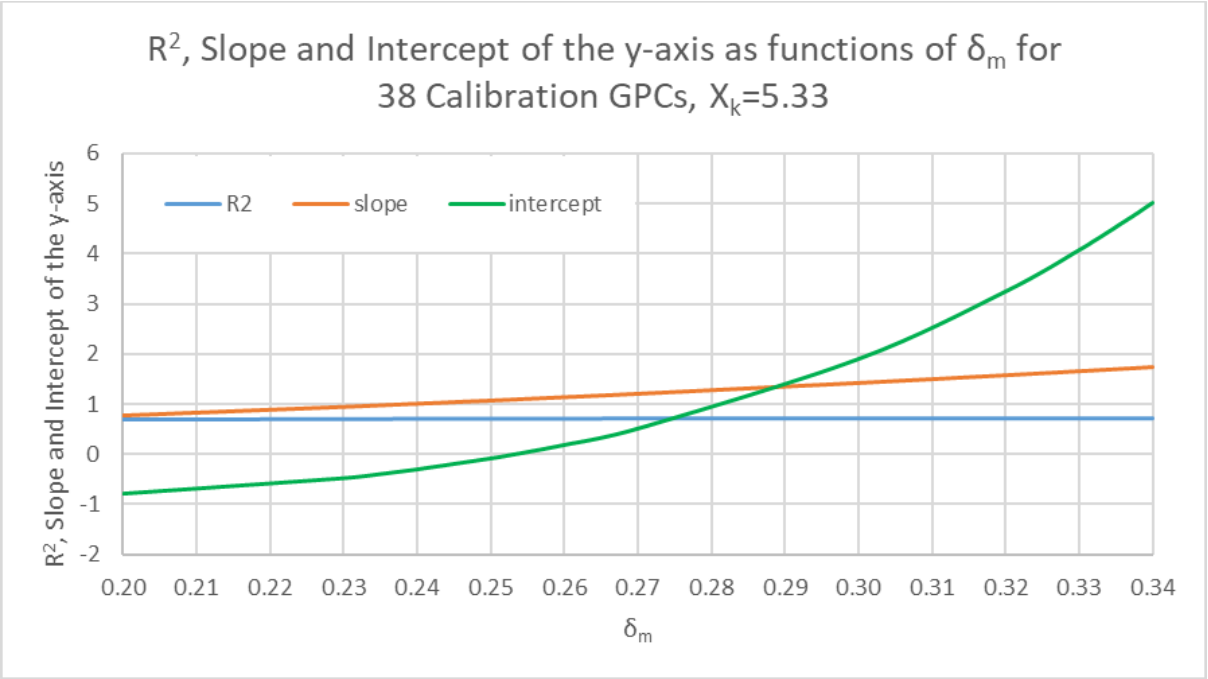

Figure 39: R^2, slope and intercept of the y-axis as functions of different values for δ_m, based on the 38 randomly chosen GCPs used for the alternative calibration.

For T_H (Figure 40), the value for R^2 changes little throughout the graph but reaches a maximum of 0.6530 at T_H value 293 K, with decreasing values for lower and higher T_H. The slope increases from 0.4623 at 290 K, to 1.3917 at 303 K. It is closest to one (1.042) at 296 K. The intercept decreases from 0.2446 at 290 K, to -0.1418 at 303 K. It is closest to zero (-0.0178) at 298 K. Whereas the R^2 curb is almost flat, the curbs for slope and intercept are steep in opposite directions.

The baseline value for T_H is 296 K. Decreasing it slightly improves the R^2 but worsens the slope and the intercept. Decreasing it more than slightly worsens the R^2, the slope and the intercept. Increasing it slightly worsens the R^2 and the slope but improves the intercept. Increasing it more than slightly worsens the R^2, the slope and the intercept. Adjusting T_H would hence not result in an unambiguous improvement of the model accuracy and the parameter was therefore not adjusted.

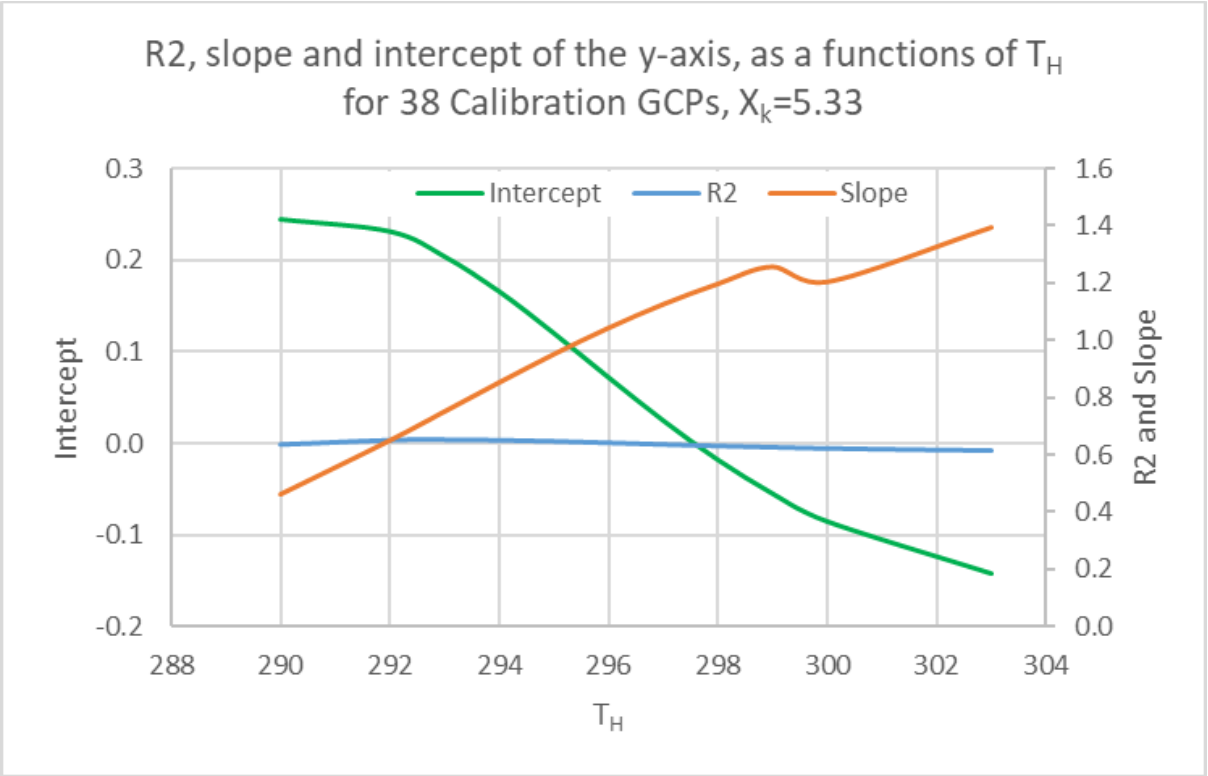

Figure 40: R^2, slope and intercept of the y-axis as functions of different values for T_H based on the 38 randomly chosen GCPs used for the alternative calibration.

4.2. Historical Growth

The mean growth rate for each year 2011 - 2020 for 5 and 8 cm mussels are presented in Figure 41 and Figure 42. Both figures, or sets of maps, present their highest mean growth rates in the GoL, notably in the vicinity of the river Rhône, and the lowest mean growth rates around Corsica. Both sets display their highest mean growth rates in years 2014 and 2016 (0.057 g / day for 5 cm mussels and 0.119 - 0.120 g / day for 8 cm mussels). The two sets exhibit similar minimum mean growth rates (0.014 - 0.017 g / day for 5 cm mussels vs. 0.012 - 0.020 g / day for 8 cm mussels) but 8 cm mussels have twice as high maximum mean growth rates compared to 5 cm mussels (0.113 - 0.120 g / day vs. 0.054 - 0.057 g / day).

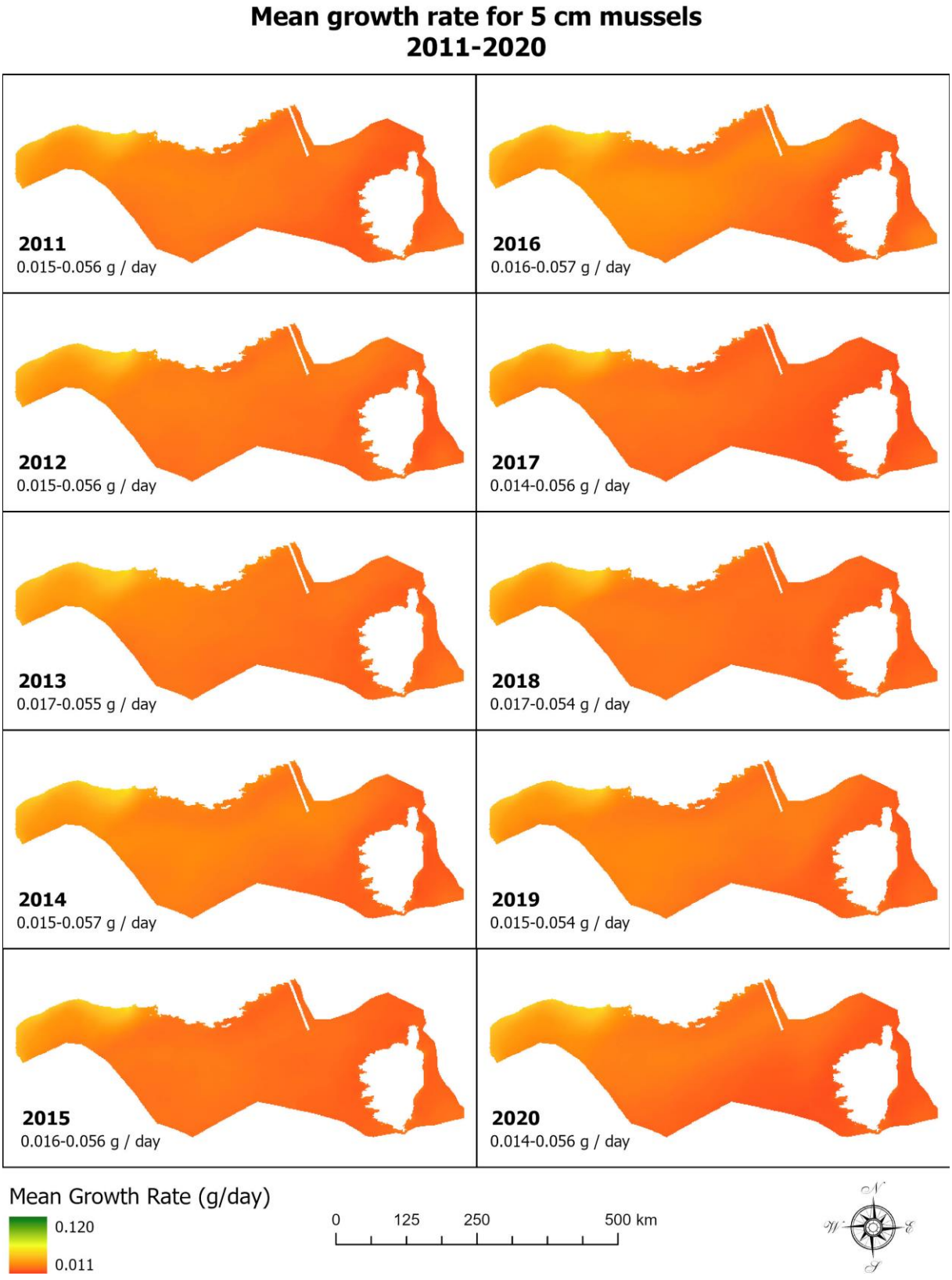

Figure 41: Mean growth rate for 5 cm mussels in 2011 - 2020. Modelled with an adjusted Dynamic Energy Budget (DEB) equation for 5 cm mussels. The colour significance is indicated in the lower left corner of the figure. The range specific for each individual map is indicated in the lower left corner of each individual map.

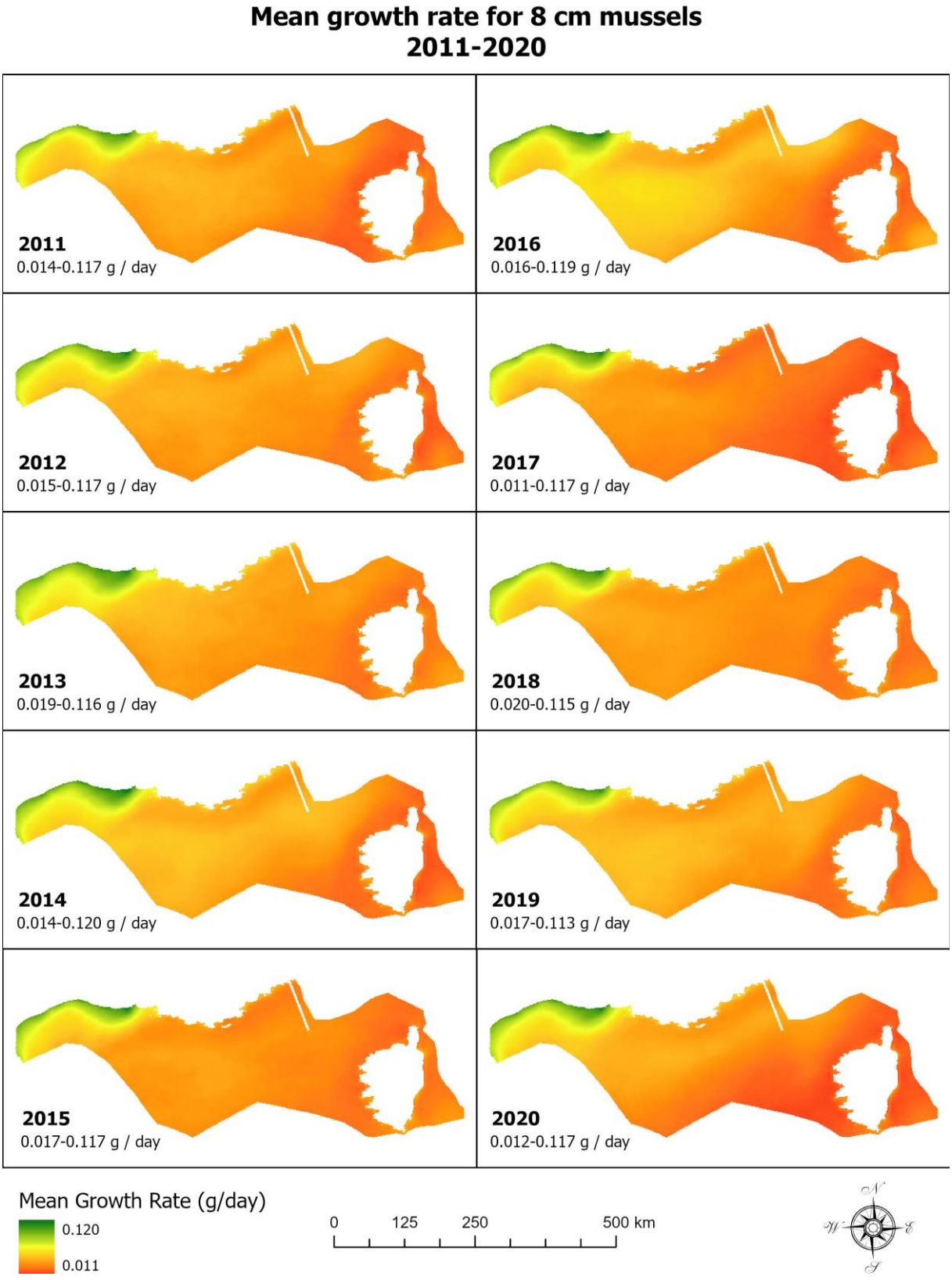

Figure 42: Mean growth rate for 8 cm mussels 2011 - 2020. Modelled with an adjusted Dynamic Energy Budget (DEB) equation, for 8 cm mussels. The colour significance is indicated in the lower left corner of the figure. The range specific for each individual map is indicated in the lower left corner of each individual map.

As seen in Figure 43 and Figure 44, the north-western parts of the offshore French Mediterranean Exclusive Economic Zone (EEZ) exhibit more suitable farming areas than its southwestern parts. For both sets of maps, 2017 is the year with the smallest suitable area. Maps for 8 cm mussels have vastly more suitable area than those for 5 cm mussels. For 5 cm mussels, 2014 and 2016 have more suitable areas than other years, especially southeast of the GoL towards the Corso-Ligurian basin, whereas 2015 and 2019 have almost as little suitable area as 2017. For 8 cm mussels, 2015 and 2020 are years with less suitable area although not as little as 2017.

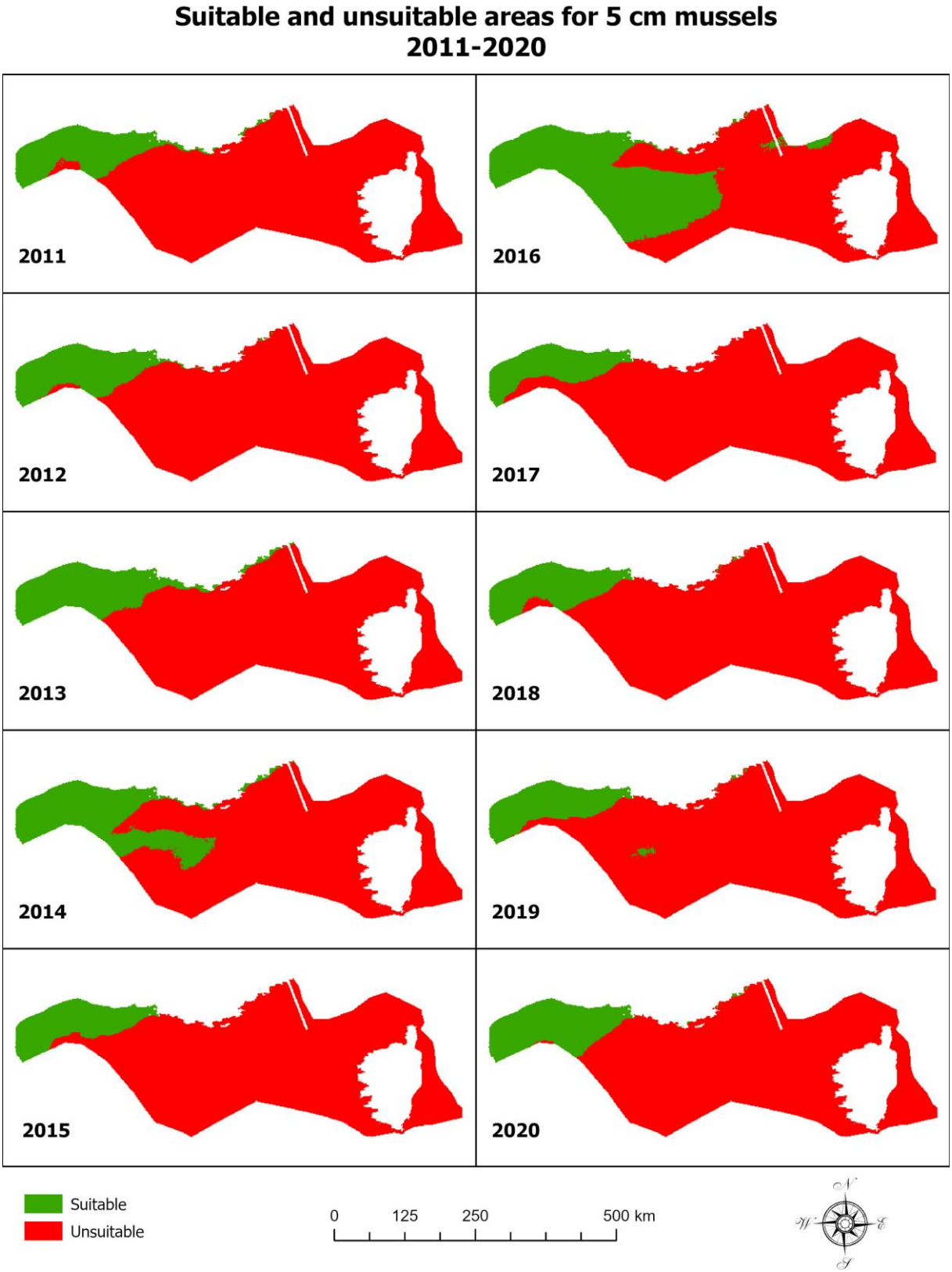

Figure 43: Suitable and unsuitable areas for 5 cm mussels 2011 - 2020. Cells with a mean growth rate ≥ 0.028 g / day were considered suitable for mussel cultivation and cells with a mean growth rate < 0.028 g / day were considered unsuitable for mussel cultivation.

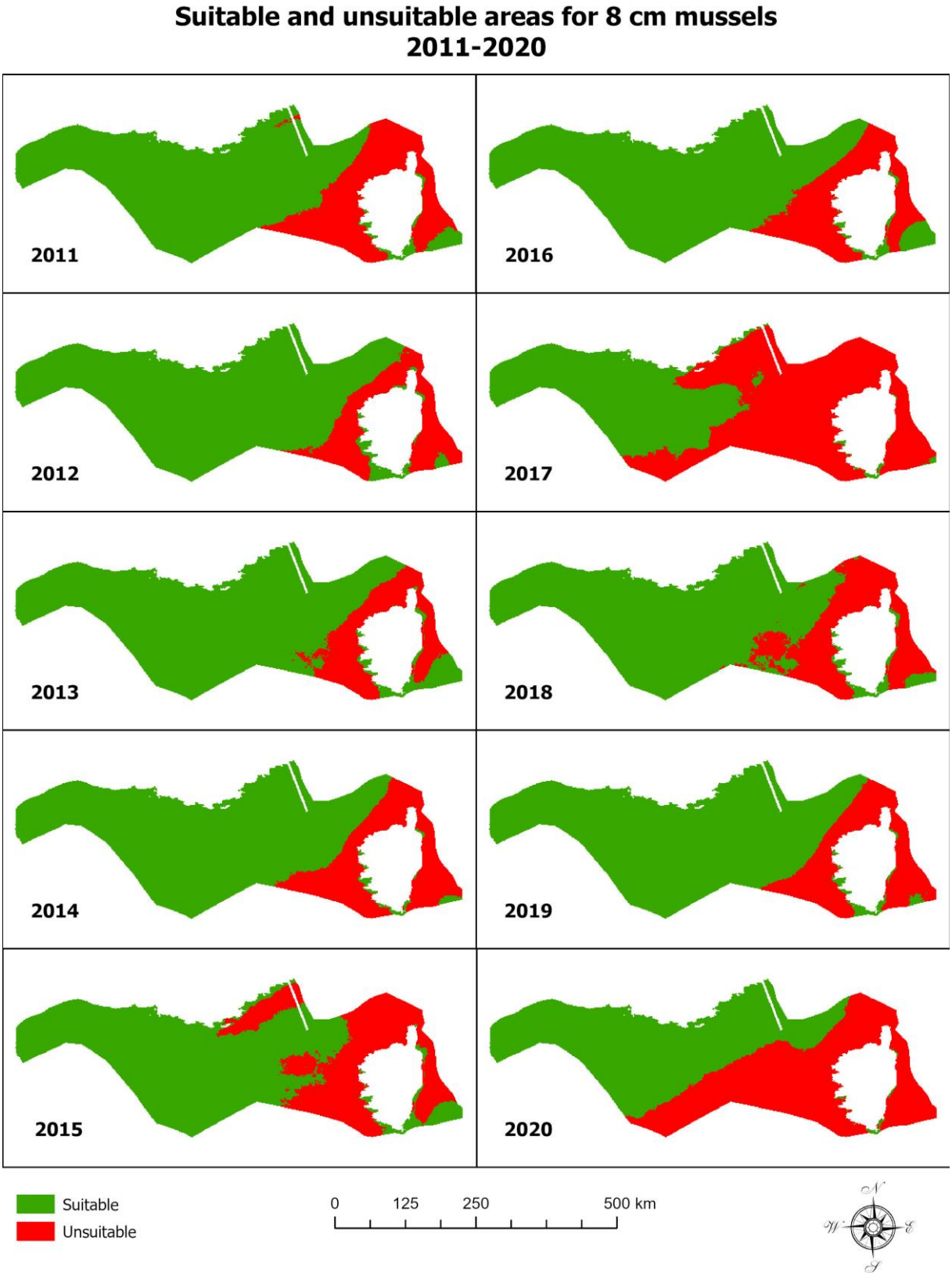

Figure 44: Suitable and unsuitable areas for 8 cm mussels 2011 - 2020. Cells with a mean growth rate ≥ 0.028 g / day were considered suitable for mussel cultivation and cells with a mean growth rate < 0.028 g / day were considered unsuitable for mussel cultivation.

In Figure 45, the areas known to be suitable for mussel cultivation (i.e., the conservative estimation based on the yearly mean growth rate of 5 cm mussels), the areas known to be unsuitable for mussel cultivation (i.e., where even the mean yearly growth rate of 8 cm mussels would not suffice for farming) and the potentially suitable areas in between are presented.

The potentially suitable area is largest in 2019 (due to small suitable and unsuitable areas that year) and at its smallest in 2016 (due to a large suitable area that year) but the main pattern with suitable areas in the northwest and unsuitable in the southeast remains.

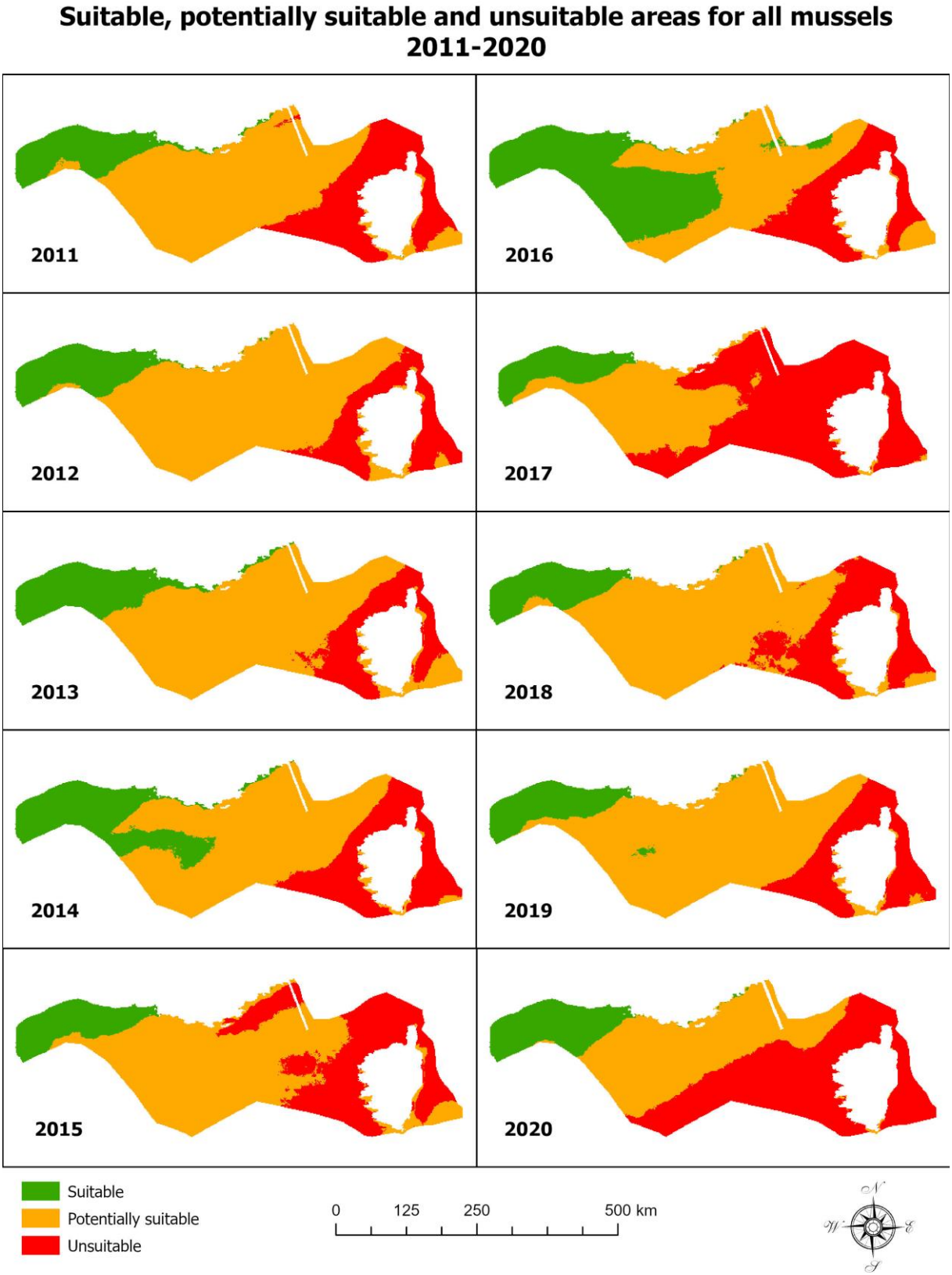

Figure 45: Yearly distribution of suitable, potentially suitable and unsuitable areas for mussel cultivation 2011 - 2020. Green areas are suitable for 5 cm mussels as well as for 8 cm mussels, orange areas are unsuitable for 5 cm mussels but suitable for 8 cm mussels, and red areas are unsuitable for 5 cm mussels as well as for 8 cm mussels.

As seen in Figure 46, most of the GoL, from Spain to Marseille, was considered suitable for mussel growth every year 2011 - 2020. The waters around Corsica, most of the French Riviera and the eastern part of the Corso-Ligurian basin were considered unsuitable for mussel farming. The waters in the western Corso-Ligurian basin were potentially suitable. In line with the objective to provide a conservative estimate of prime mussel farming areas in the French Mediterranean, only areas that were suitable every year 2011 - 2020 will be considered for final proposition.

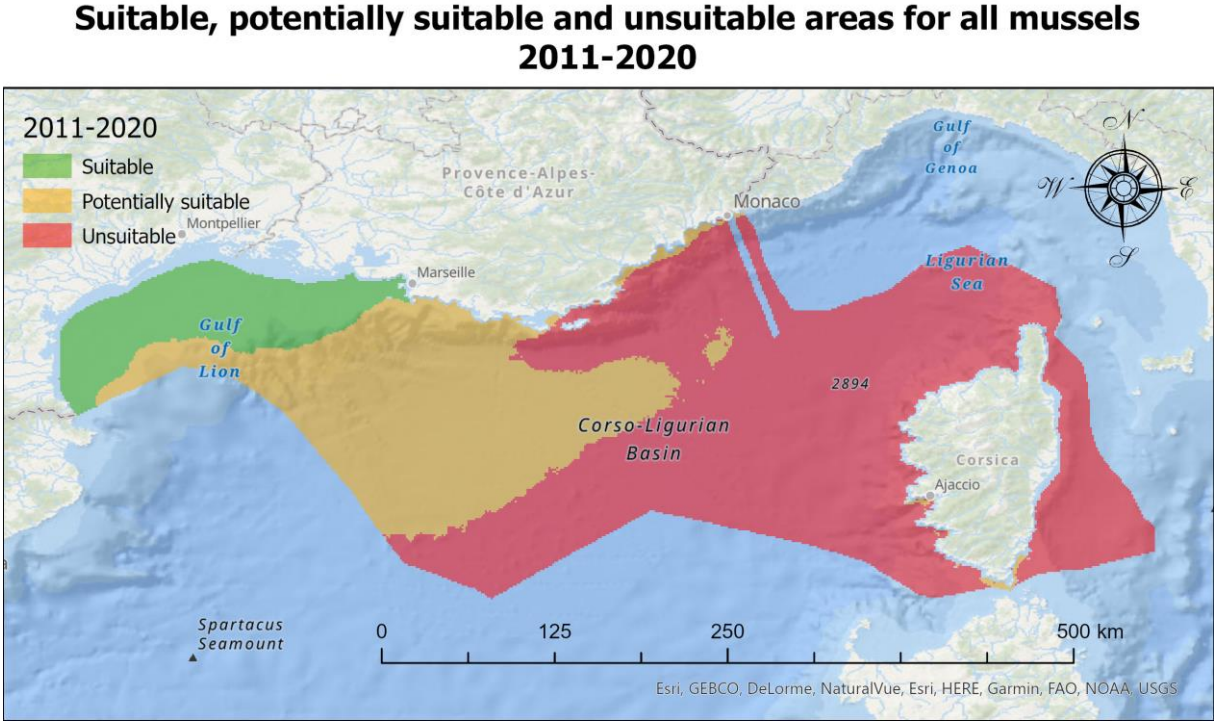

Figure 46: Decennial distribution of suitable, potentially suitable and unsuitable areas for mussel cultivation 2011 - 2020. Suitable areas (in green) areas had a mean yearly growth rate of ≥ 0.028 g / day for 5 cm mussels as well as for 8 cm mussels every year 2011 - 2020. Potentially suitable areas (in orange) had a mean yearly growth rate of < 0.028 g / day for 5 cm mussels at least one year 2011 - 2020 but ≥ 0.028 g / day for 8 cm mussels every year 2011 - 2020. Unsuitable areas (in red) had a mean yearly growth rate of < 0.028 g / day for 5 cm mussels as well as for 8 cm mussels at least one year (per size) 2011 - 2020.

4.3. Climate Change Scenarios

4.3.1. SST

As seen in Figure 47, growth rate as a function of SST starts at 0 g / day and rises slightly at temperatures just sub-zero. This is possible in part thanks to the fact that sea water freezes at a lower temperature than fresh water. The growth rate then increases with increasing temperatures until it peaks at 19 °C, after which the growth rate once again decreases, slightly faster than it previously increased, until it reaches 0 g / day just after 40 °C.

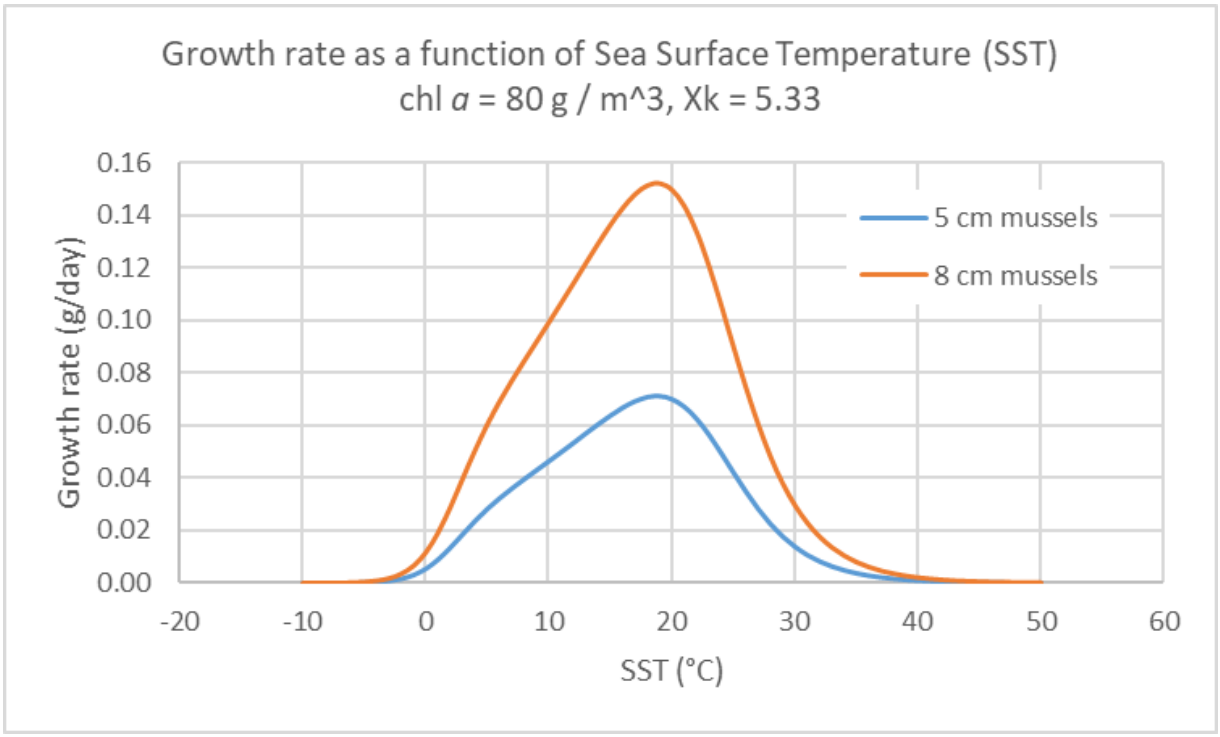

Figure 47: Growth rate as a function of SST, modelled with an adjusted DEB equation.

As shown in Table 2, the optimal level of SST (i.e., where all mussels can grow at least 0.028 g / day) is 5 °C - 27 °C. Less than optimal SST values for mussel growth are < 5 °C and > 27 °C – < 31 °C. SSTs ≥ 31 °C are, in coherence with laboratory experiments documented in published scientific journals, considered deadly for the mussels.

Table 2: SST.

	SST (°C)		
	5 cm mussels	8 cm mussels	All mussels
Optimal:	5-27	2-30	5-27
Less than optimal:	< 5 and > 27 - < 31	< 2 and > 30 - < 31	< 5 and > 27 - < 31
Deadly (from literature):	≥ 31	≥ 31	≥ 31

As seen in Figure 48, 2014 was the year during the IPCC reference period with the highest mean SST and was therefore used as baseline for modelling SSTs in scenario RCP 8.5 Long Term.

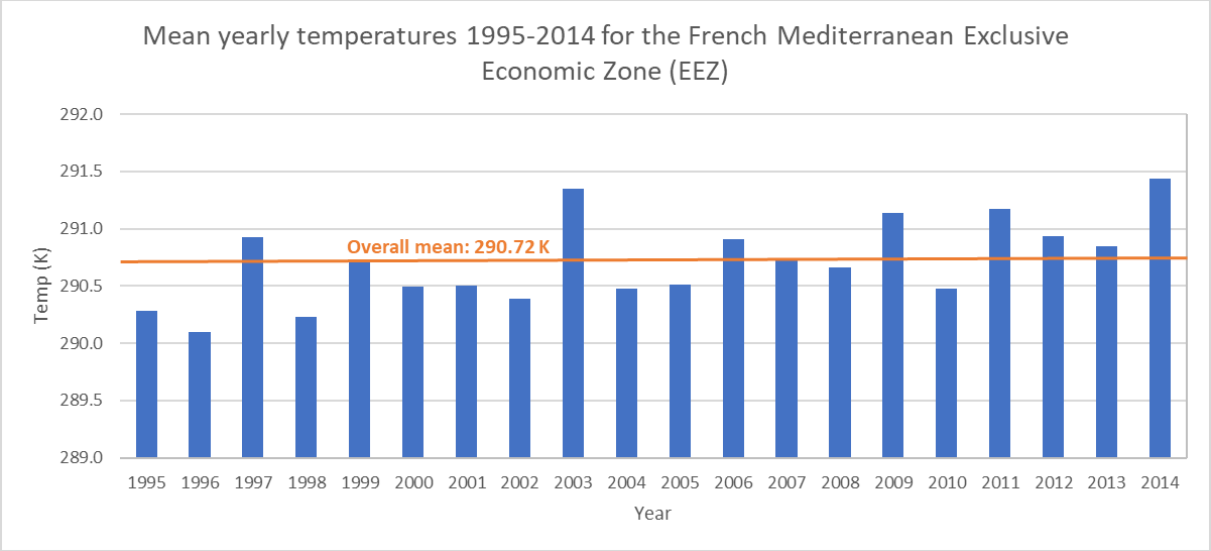

Figure 48: Mean yearly temperatures 1995-2014.

Mean monthly prospective SST is presented in Figure 49. The coldest SSTs are present in February and March, followed by an increase in SSTs until a peak is reached in August and September, after which the SSTs once again decreases. The coldest temperatures are generally found in the GoL or further south in the western Corso-Ligurian basin, whereas the warmest temperatures are generally located off the French Riviera, around Corsica and in the south-eastern parts of the Corso-Ligurian basin.

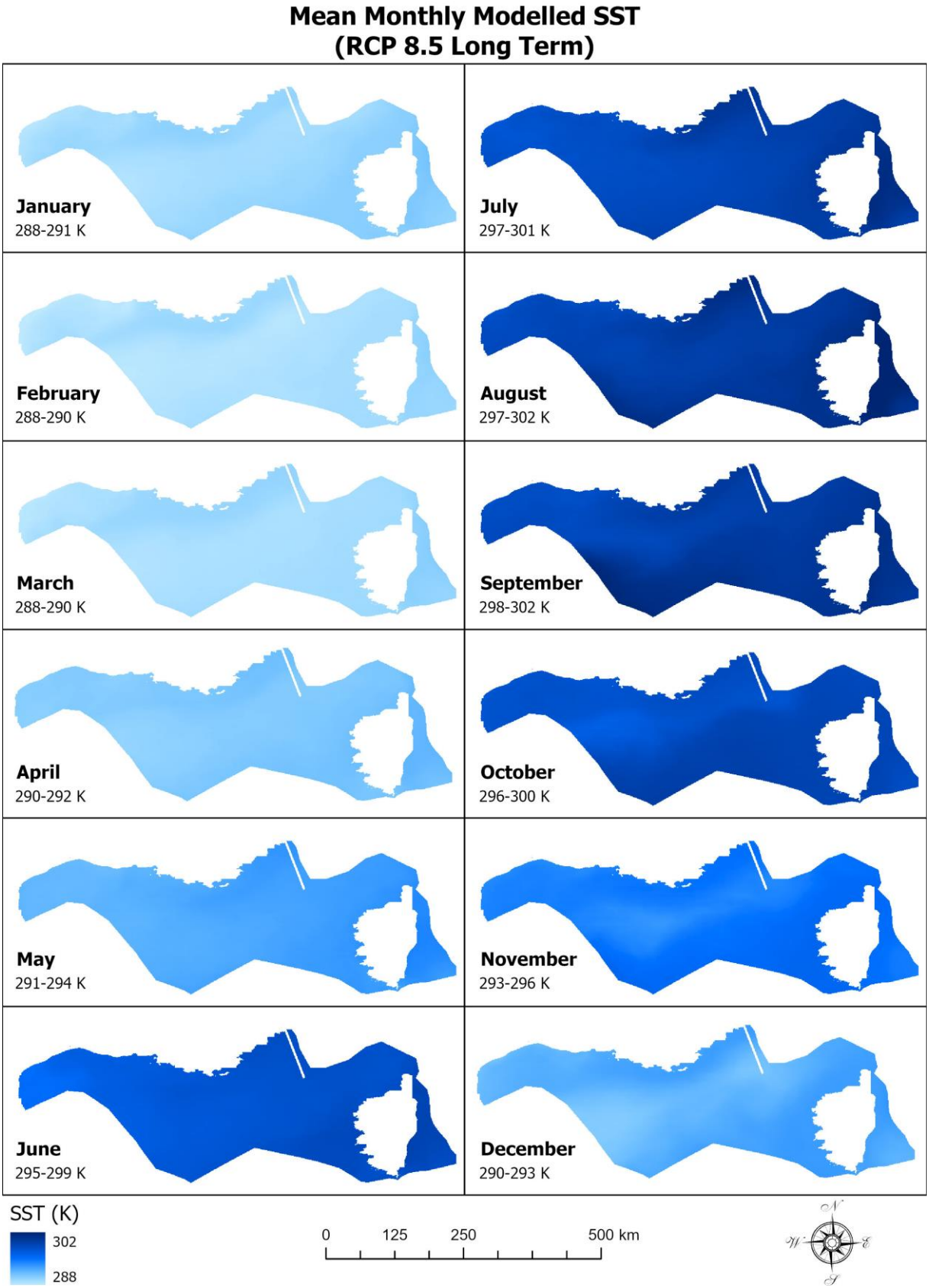

Figure 49: Mean monthly SST for RCP 8.5 Long Term. Colour indications are found in the lower left corner of the figure. Values specific for each individual map is found in the lower left corner of each map.

The mean prospective SST for the entire year is presented in Figure 50. The lowest mean SSTs for the year is found in the GoL as well as in the western Corso-Ligurian basin. The highest mean SSTs were found east of Corsica as well as off the French Riviera and in the south-eastern Corso-Ligurian basin.

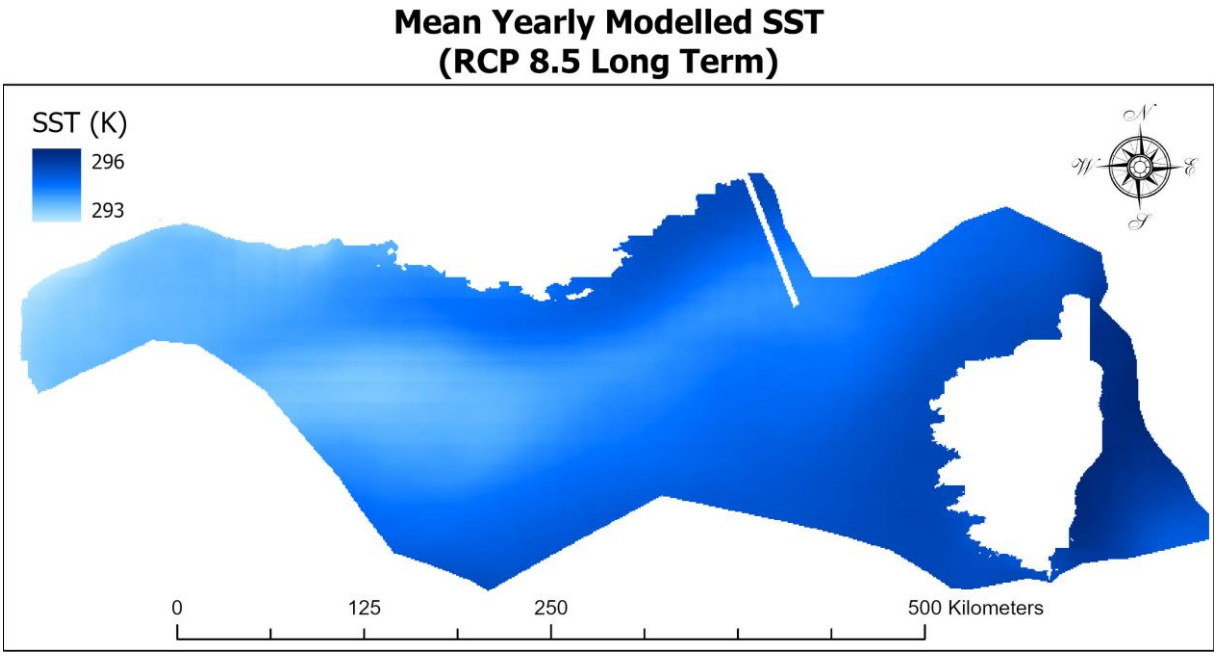

Figure 50: Mean SST for the warmest year in climate change scenario RCP 8.5 Long Term.

As seen in Figure 51, SST modelling for climate change scenario RCP 8.5 Long Term indicated that nowhere offshore in the French Mediterranean EEZ will there be, until at least the end of the 21st century, SSTs ≥ 31 °C. It is noteworthy that several areas off the Italian coastline, although not visible in the maps presented here, experience days with SSTs above 31 °C for climate change scenario RCP 8.5 Long Term. Mussels are thus not expected to die in the study area due to high SSTs.

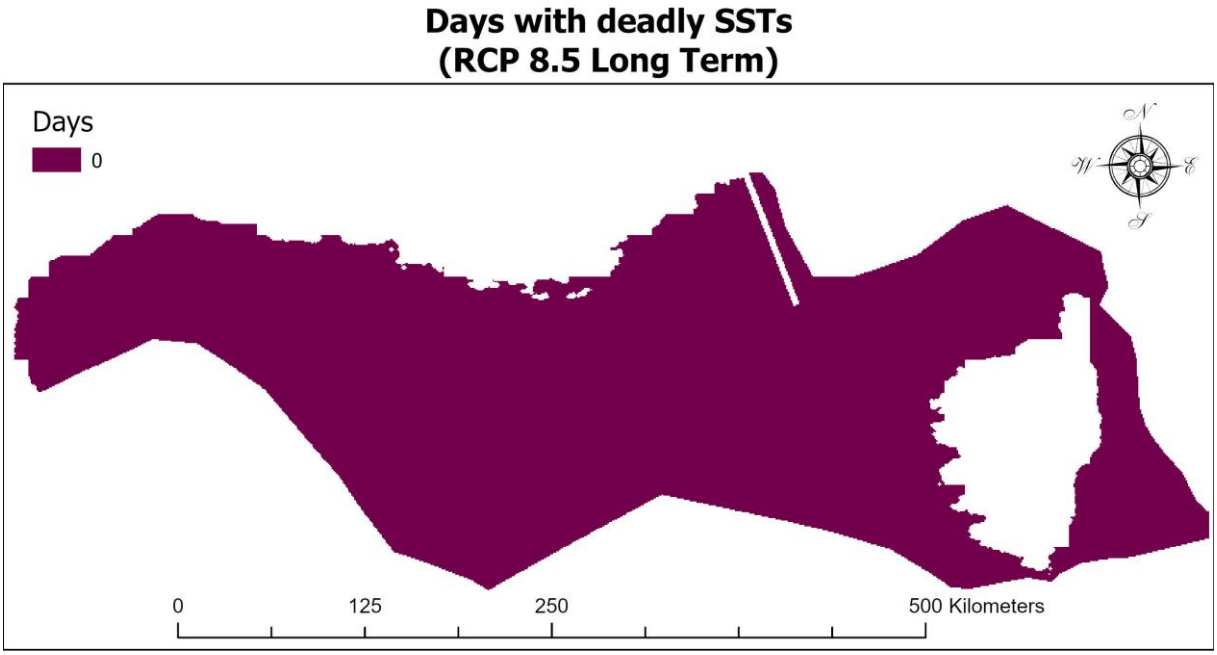

Figure 51: Number of days when SST is predicted to be ≥ 31 °C, a temperature that is deadly for mussels, in the warmest year of climate change scenario RCP 8.5 Long Term.

As can be seen in Figure 52 and Figure 53, the two months with most days of less than optimal SSTs were August and September, whereas January through May as well as November and December had exclusively days with optimal SSTs. When less than optimal SSTs were present, they were most common east of Corsica, followed by off the French Riviera and in the southern and south-eastern Corso-Ligurian basin.

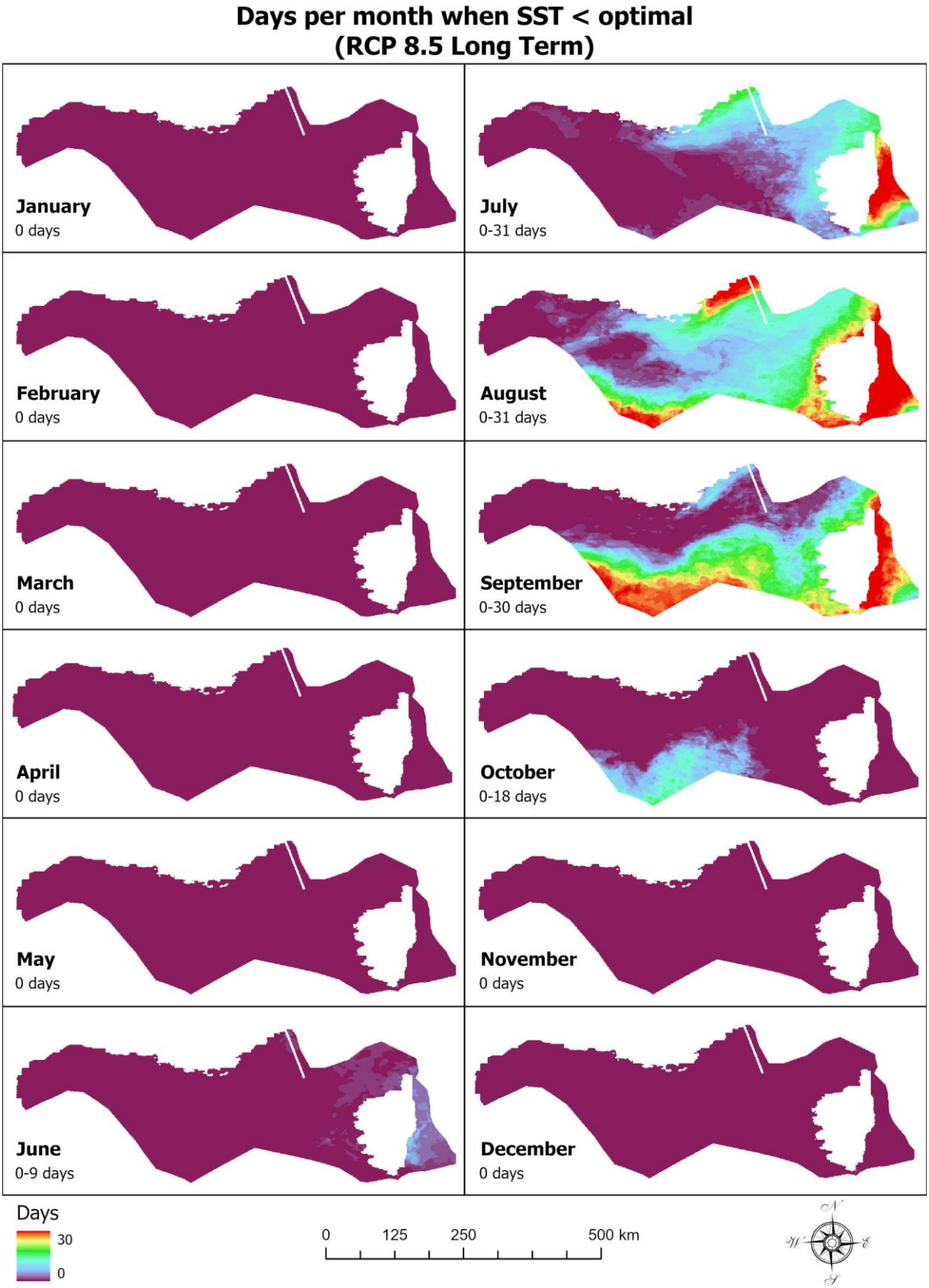

Figure 52: Days per month with less than optimal SSTs for mussel growth in climate change scenario RCP 8.5 Long Term. SSTs < 5 °C and SSTs > 27 °C – < 31 °C are considered less than optimal. SSTs ≥ 31 °C were not present. Colour indications are found in the lower left corner of the figure. Values specific for each individual map is found in the lower left corner of each map.

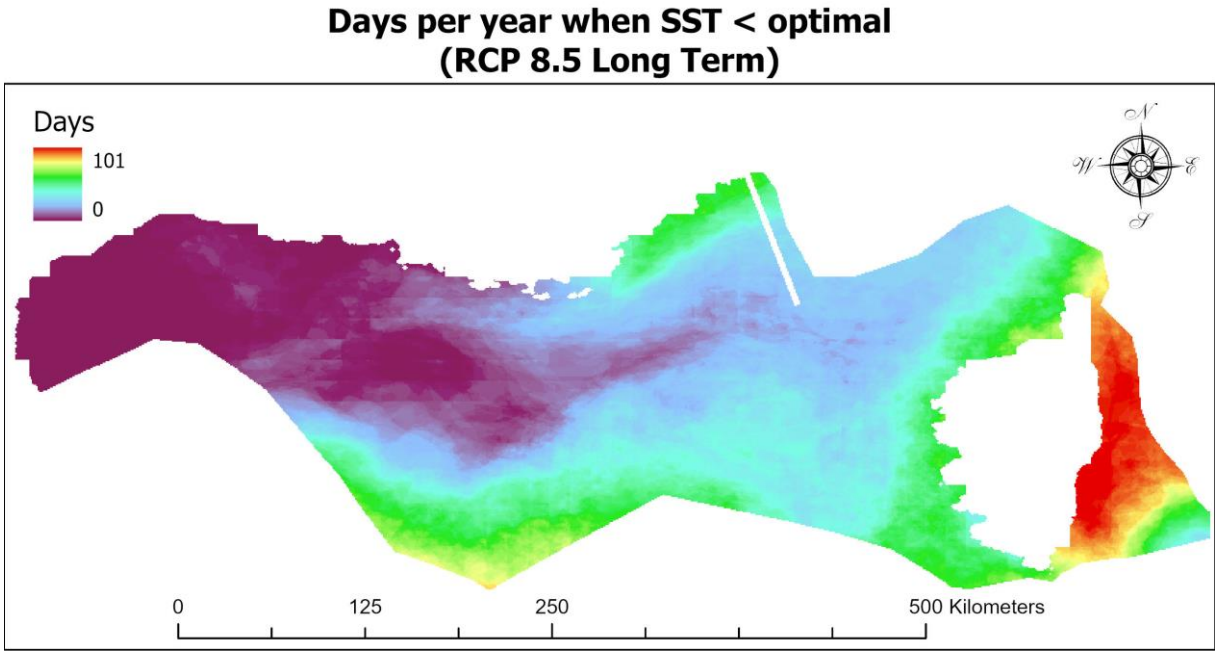

Figure 53: Days with less than optimal SSTs for the warmest year in climate change scenario RCP 8.5 Long Term. SSTs 5 - 27 °C were considered optimal and SSTs < 5 °C or > 27 - < 31 °C less than optimal. SSTs ≥ 31 °C were not present.

Figure 54 presents areas where the SST conditions are *i*) always optimal (green) or *ii*) less than optimal at least one day during the year (red) during the warmest year between 2018 and 2100 in climate change scenario RCP 8.5. SSTs 5 - 27 °C are considered optimal whereas < 5 °C or > 27 - < 31 °C are considered less than optimal. SSTs ≥ 31 °C were not present in the dataset. Optimal areas are located in the western half of GoL as well as by the outflow of river Rhône and a small area in the western Corso-Ligurian basin.

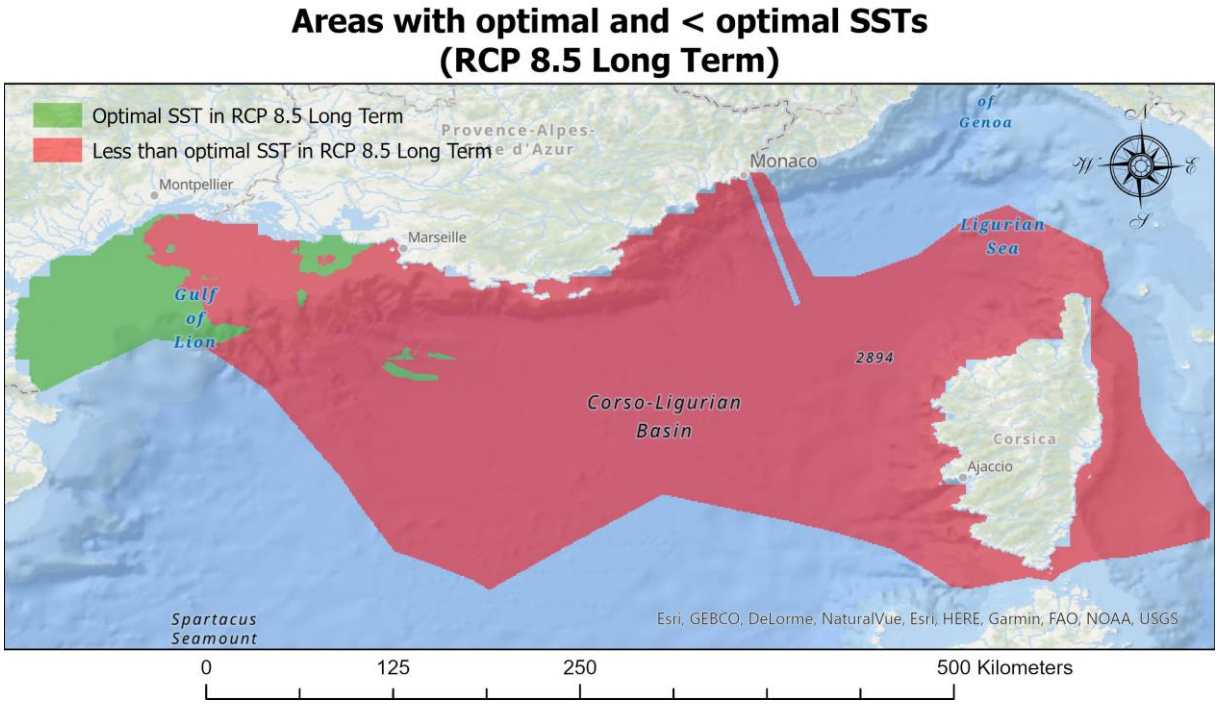

Figure 54: Areas with optimal and less than optimal SSTs in climate change scenario RCP 8.5 Long Term. Green areas are always optimal and red areas are less than optimal at least one day during the during the warmest year between 2081 and

2100 in climate change scenario RCP 8.5. SSTs between 5 °C and 27 °C were considered optimal and SSTs < 5 °C or > 27 - < 31 °C less than optimal. SSTs ≥ 31 °C were not present.

4.3.2. Chl *a*

Growth rate as a function of chl *a* at a stable optimal SST of 292.15 K (19 °C) for 5 and 8 cm mussels, respectively, are presented in Figure 55 and Figure 56. The two graphs depict the same data but with different ranges of chl *a*, where the first graph depicts chl *a* values 0 - 100 mg / m^3 and the second graph is a clarification of the curves for chl *a* values 0.0 - 1.0 mg / m^3.

Both 5 cm mussels and 8 cm mussels experience rapidly increasing growth rates for chl *a* values 0.0 - 0.1 mg / m^3, followed by a slightly less rapid increase in growth rate for chl *a* values 0.1 - 1.0 mg / m^3. The increase in growth rate further decelerates until it reaches a relatively stable state around 5 mg chl *a* / m^3. The stable growth rate for 5 cm mussels ensues at 0.07 g chl *a* / m^3 and for 8 cm mussels at 0.15 g chl *a* / m3. As shown in Table 3, the optimal level of chl *a* (i.e., where all mussels can grow at least 0.028 g / day) is ≥ 0.119 mg chl *a* / m^3 (≥ 0.119 mg chl *a* / m^3 for 5 cm mussels and ≥ 0.095 mg chl *a* / m^3 for 8 cm mussels). Chl *a* levels < 0.119 mg / m^3 are thus to be considered less than optimal.

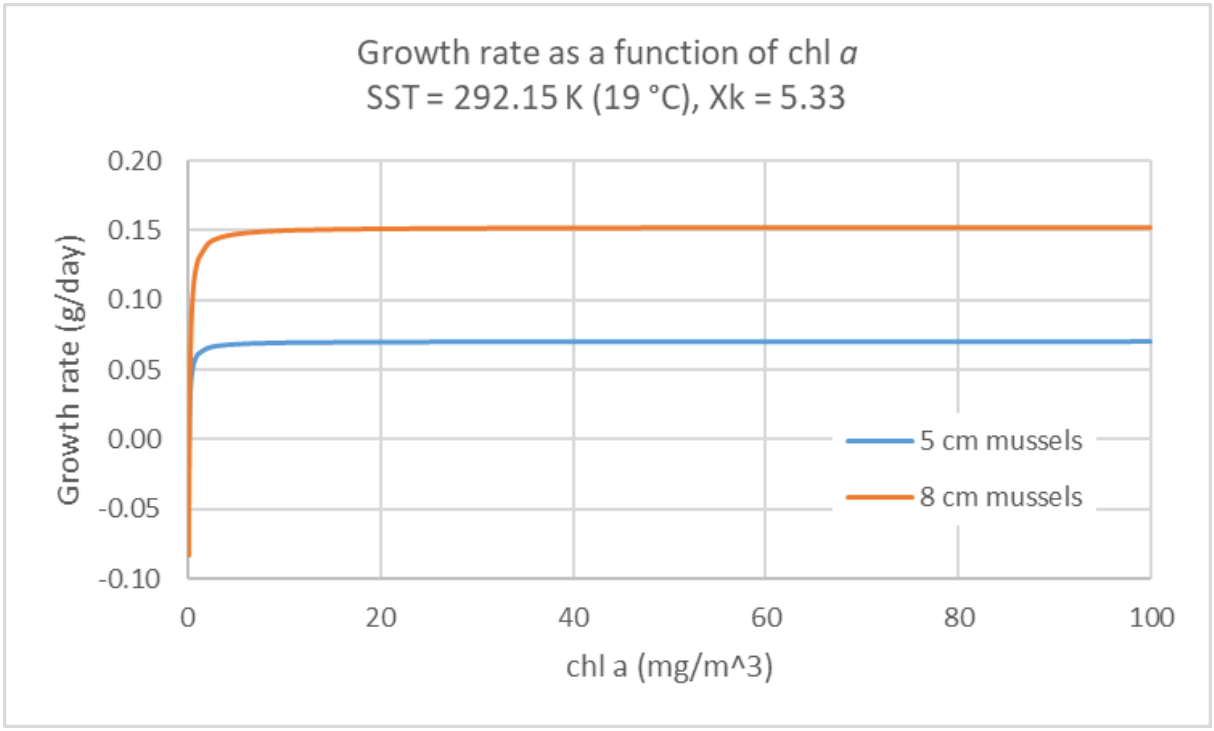

Figure 55: DEB modelled growth rate as a function of chl a 0 - 100 mg / m^3.

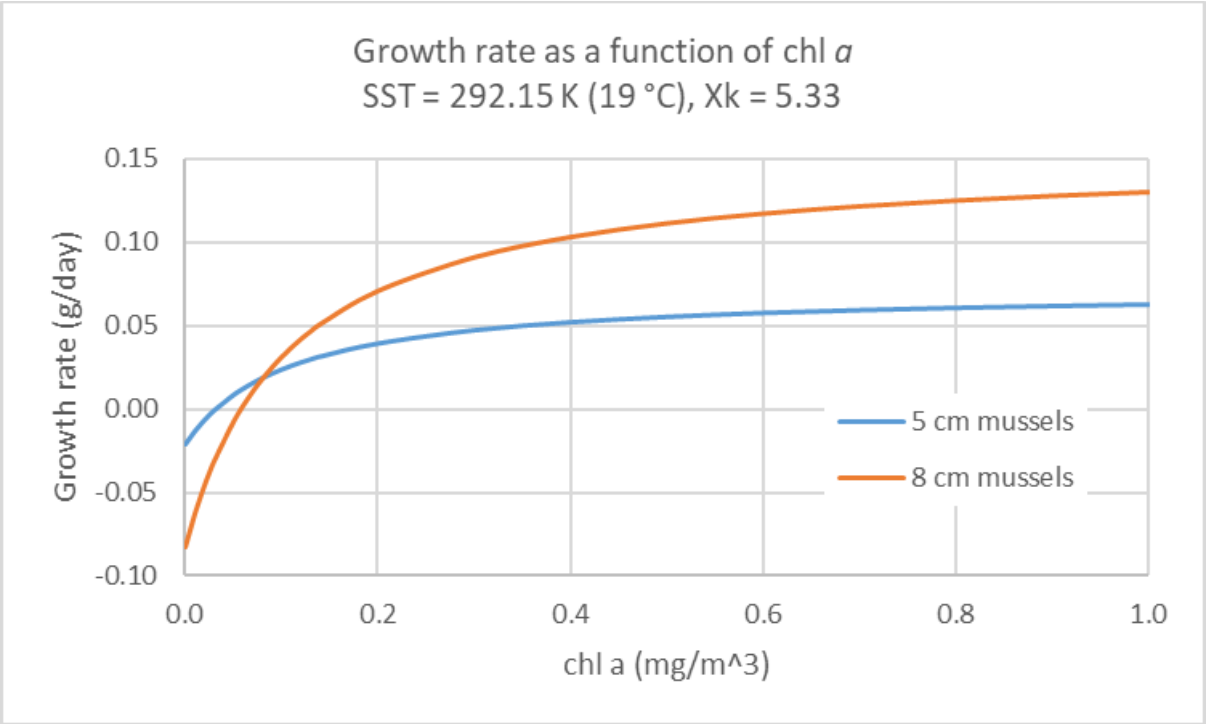

Figure 56: DEB modelled growth rate as a function of chl a 0 - 1 mg / m³.

Table 3: Chl a.

chl *a* (mg/m^3)			
	5 cm mussels	8 cm mussels	All mussels
Optimal:	≥ 0.119	≥ 0.095	≥ 0.119
Less than optimal:	< 0.119	< 0.095	< 0.119

During 2011 - 2020, all recorded SSTs in the French Mediterranean were within the limits for optimal SST. Hence, any area considered optimal for mussel growth during 2011 - 2020 inherently exhibits optimal chl *a* levels (it's a requirement for optimal growth) and historical chl *a* data has thus already been examined.

Nevertheless, the mean number of days per year during the period 1998-2020 when chl *a* levels exceeded 0.119 mg / m^3 are presented in Figure 57. The GoL exhibits superior chl *a* conditions with 0 - 90 suboptimal days per year, whereas the conditions around Corsica and, to some extent, off the French Riviera, are inferior with over 300 suboptimal days per year.

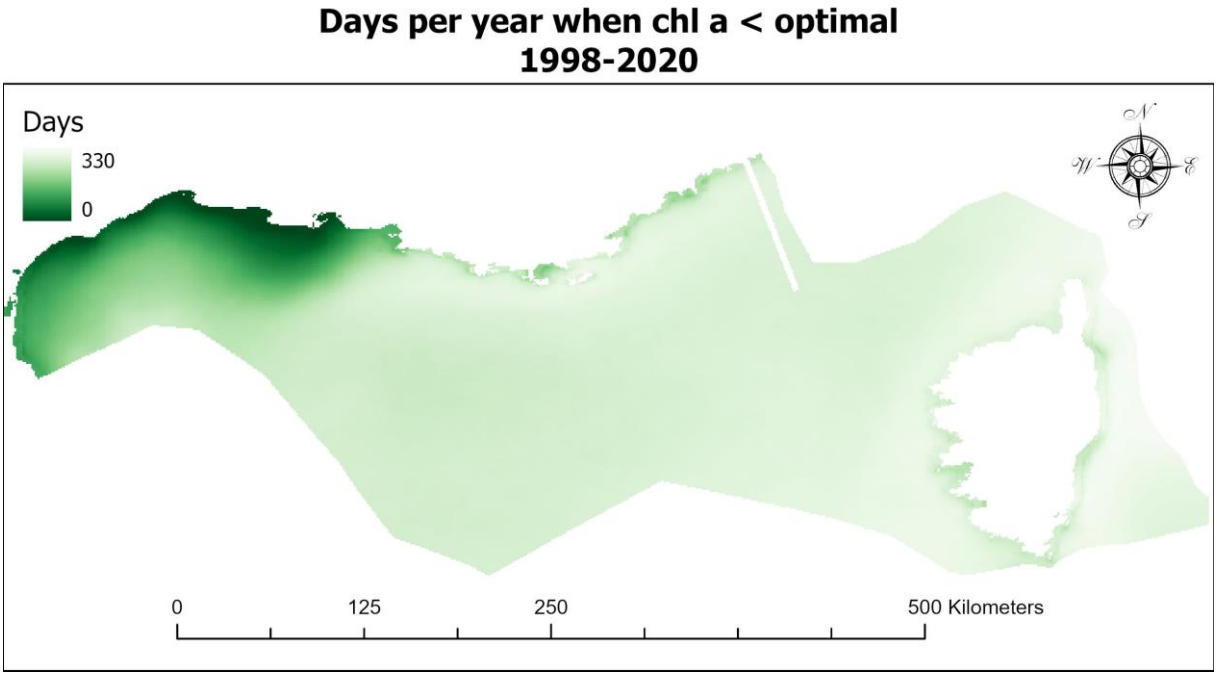

Figure 57: Days per year 1998-2020 when chl a was less than optimal for mussel farming.

4.4. IMTA Scenario

The resulting map for modelled mean yearly growth of mussels in proximity to a hypothetic fish farm (Phyto-C set to 0.578 mg C / m^3) is presented in Figure 58.

Mean growth is highest in the western parts of GoL and gradually decreases towards the southeast. The western Corso-Ligurian Basin has a slightly higher growth compared to its eastern parts. The lowest rates of mean growth are found along entire coast of Corsica as well as in the waters off the French Riviera.

The growth rate interval is between 0.044 g / day and 0.051 g / day. Hence, DEB-modelling of an IMTA scenario results in growth rates that are consistently higher than 0.028 g / day. As can be seen in Figure 59, the entirety of the study area was considered suitable for mussel growth in an IMTA scenario every year 2011 - 2020.

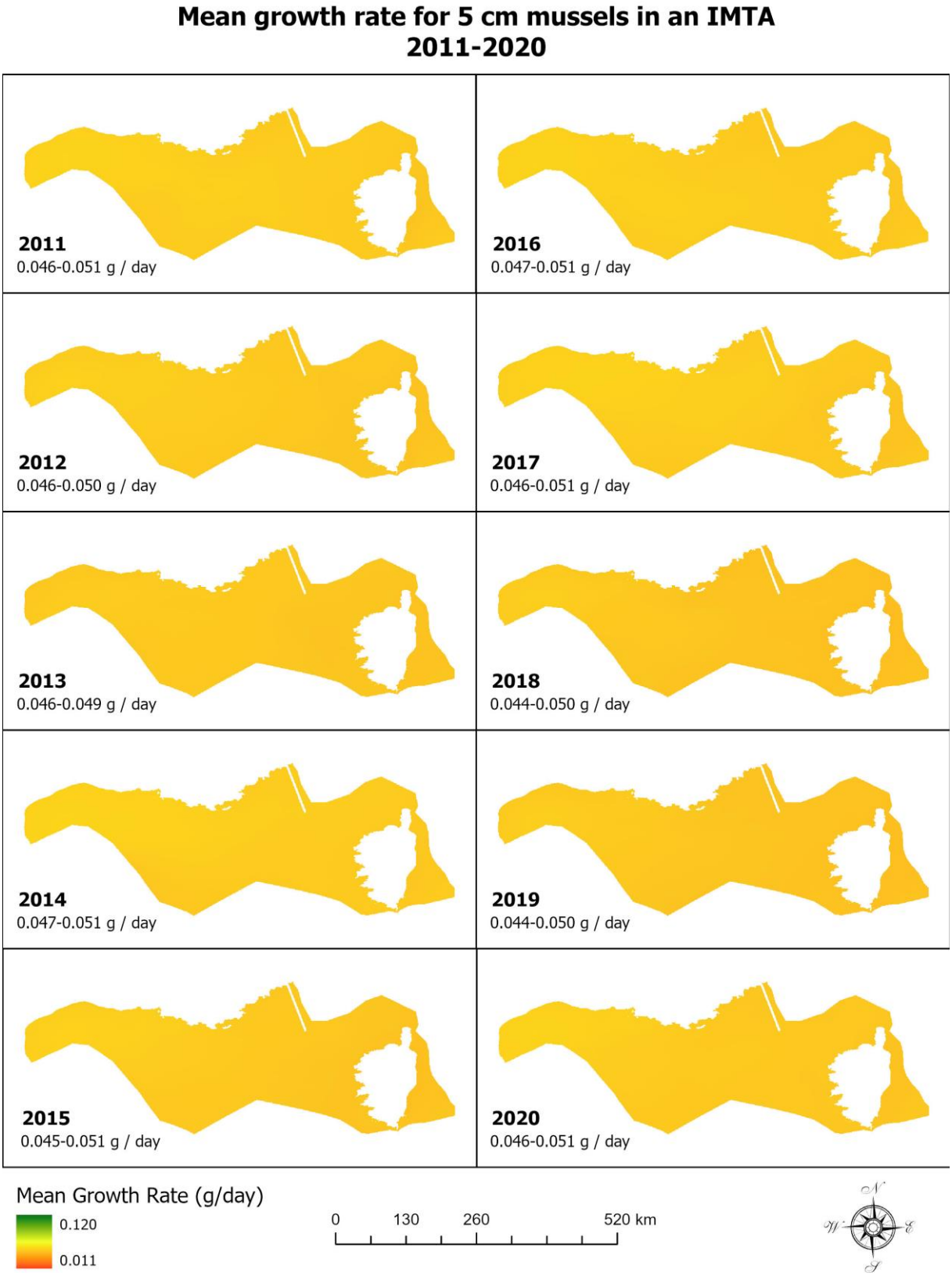

Figure 58: Mean yearly growth rate 2011 - 2020 for an IMTA scenario. The colour range is indicated in the lower left corner of the figure. The range specific for each individual map is indicated in respective maps' lower left corner.

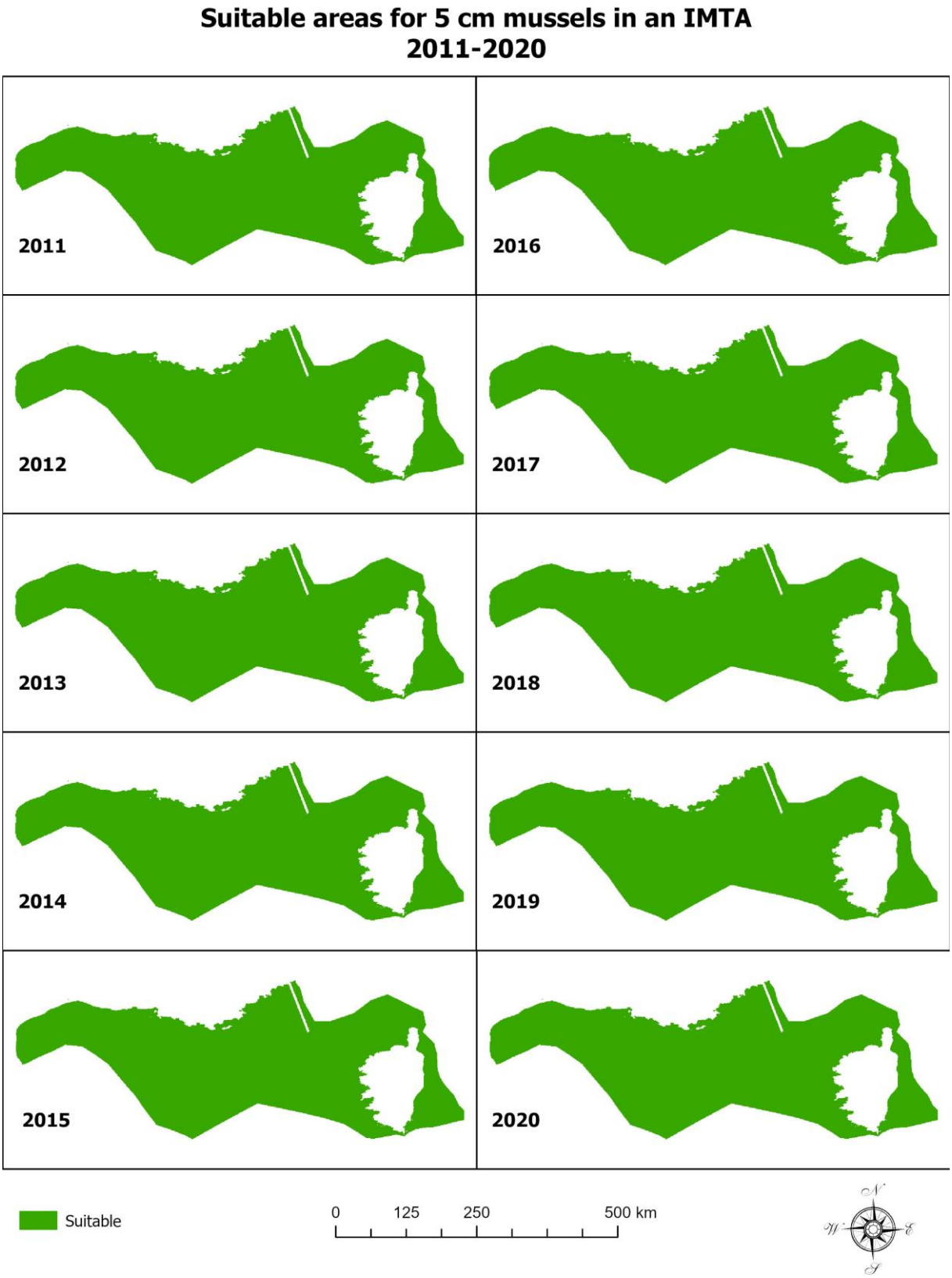

Figure 59: Yearly presentation of suitable areas for mussel growth in an IMTA scenario 2011 - 2020. Unsuitable areas were not present.

4.5. Combined Scenarios

4.5.1. Historical Growth and RCP 8.5 Long Term

Locations that *i*) were considered suitable for cultivation during period 2011 - 2020 and *ii*) are expected to stay within the range for optimal SST for another 80 years, even for the climate change predictions with the largest temperature change, are presented in Figure 60 c. The locations in question are concentrated to the output zone for River Rhône in addition to the western half of the GoL.

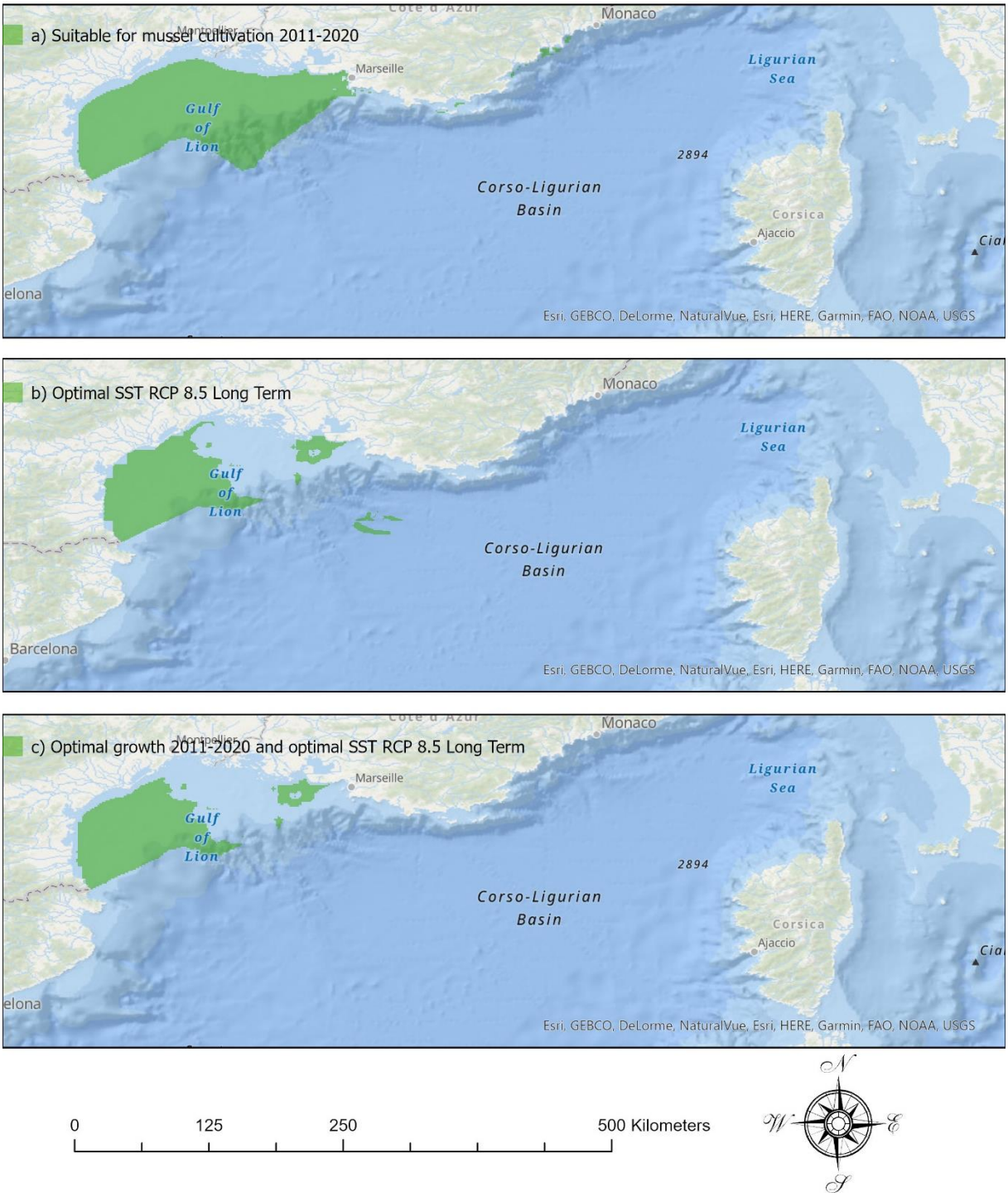

Figure 60: Optimal growth areas 2011 - 2020 (a), optimal SST for RCP 8.5 Long Term (b), and both together (c).

4.5.2. IMTA and RCP 8.5 Long Term

Mean monthly growth rate for mussels in a combined IMTA- and climate change scenario is presented in Figure 61. The mean growth rate is higher (0.049 – 0.056 g / day) from January through May, decreases somewhat in June (0.023 – 0.049 g / day), is at its lowest in July through September (0.014 – 0.041 g / day), starts to increase again in October (0.026 – 0.044 g / day) to reach its higher levels again in November and December (0.046 – 0.057 g / day).

Suitable and unsuitable areas, month per month in the warmest year in climate change scenario RCP 8.5, for mussels in a combined IMTA- and climate change scenario is presented in Figure 62. The study area is exclusively suitable January through June as well as November through December. August and September have the largest cover of unsuitable areas, followed by July and October. When unsuitable areas are present, they are located in the southeast of the study area, whereas the northwest (including the GoL) remains suitable.

Mean yearly growth rate for mussels in a combined IMTA- and climate change scenario is presented in Figure 63. Mean yearly growth rates present are 0.041 – 0.048 g / day. Hence, all cells exhibit a mean yearly growth rate that exceeds 0.028 g / day and, as is visible in Figure 64, the entirety of the study area exhibits exclusively suitable areas for mussels in an IMTA during the entirety of the warmest year in climate change scenario RCP 8.5 Long Term.

Figure 61: Mean monthly growth rate (g / day) for a combined IMTA- and climate change scenario. Modelled using SSTs from RCP 8.5 Long Term and a constant chl a of 28.9 mg C / m^3 (i.e., 0.578 mg chl a / m^3). The colour range for all maps is indicated in the lower left corner of the figure. The range specific for each individual map is indicated in the maps' lower left corners.

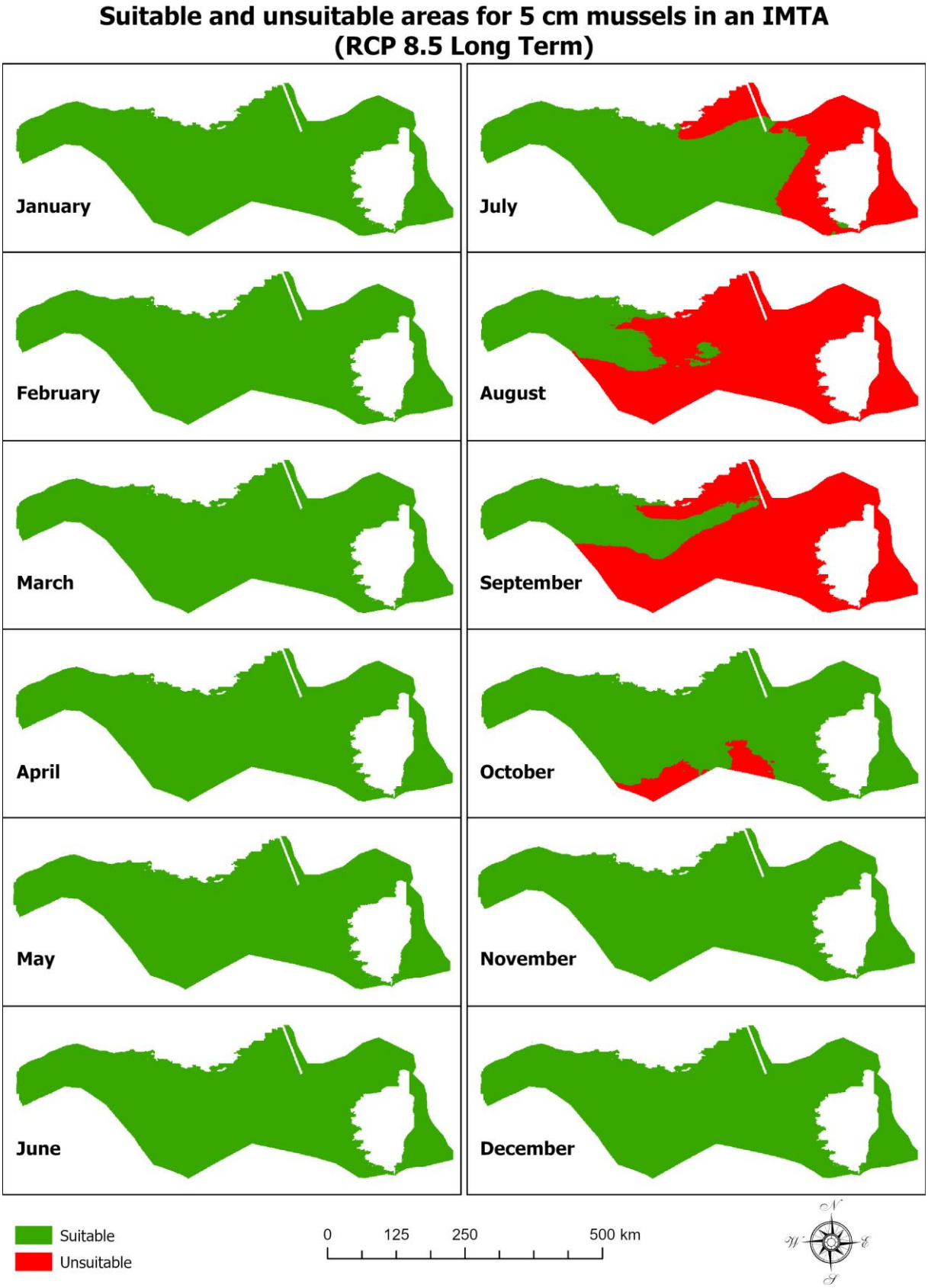

Figure 62: Suitable and unsuitable areas for mussel growth, per month, for a combined IMTA- and climate change scenario. Modelled using SST from climate change scenario RCP 8.5 Long Term and 28.9 mg C /m^3.

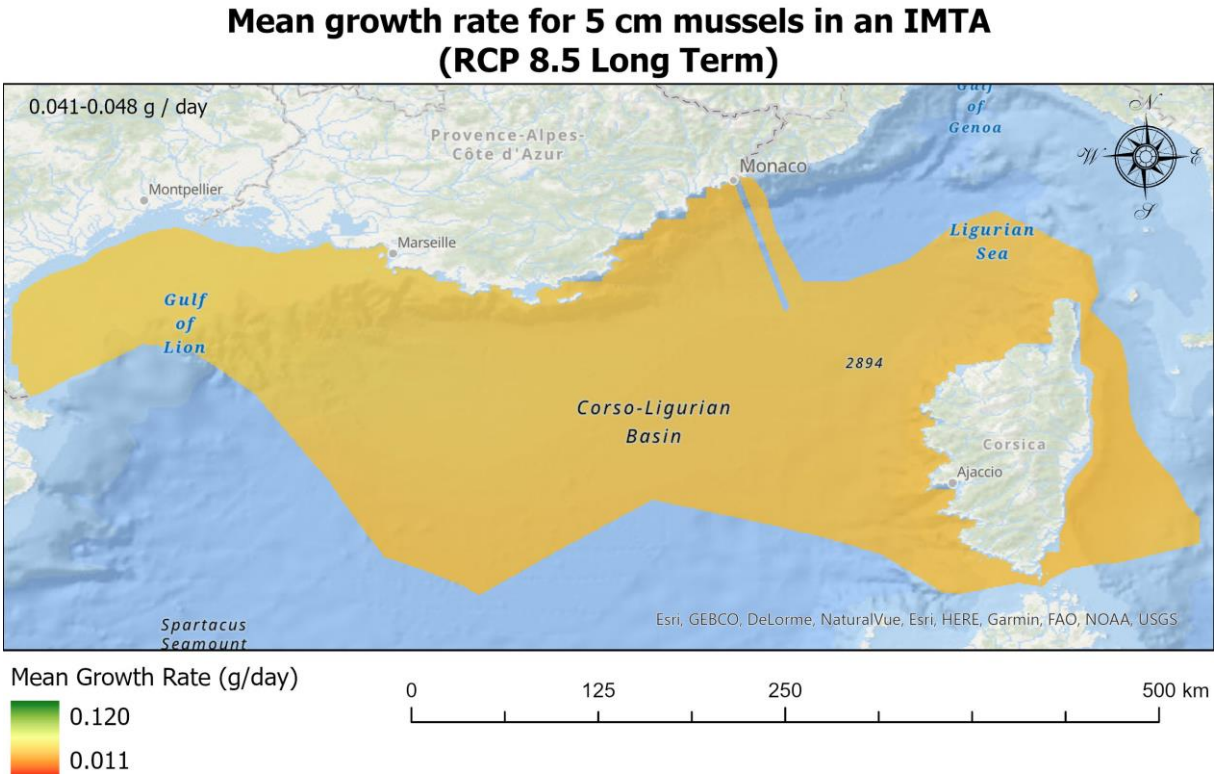

Figure 63: Yearly mean growth rate for the combined IMTA- and climate change scenario. Modelled with SSTs from climate change scenario RCP 8.5 Long Term and a constant chl a level of 28.9 mg C / m³. The color range is the same as for other maps with mean growt, and is indicated in the lower left corner. The range specific to the current map is indicated in numbers in the upper left corner

.

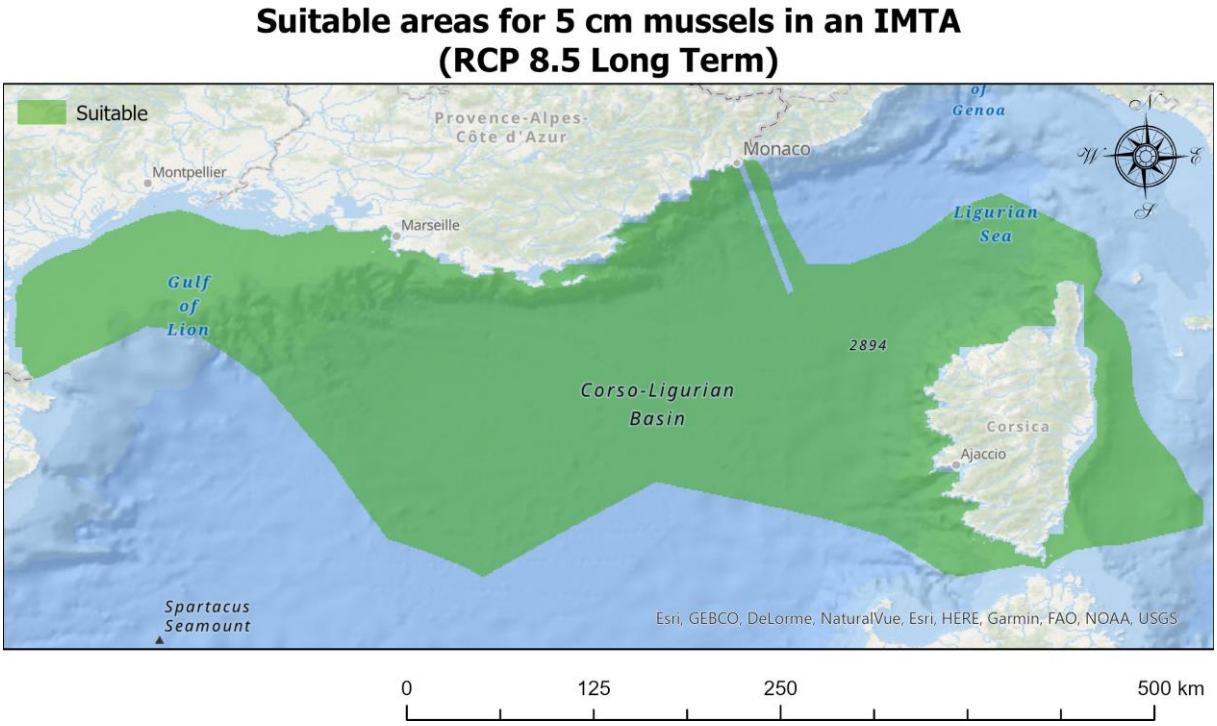

Figure 64 : Areas suitable for mussel growth, per year, for a combined IMTA- and climate change scenario. Areas where the yearly growth rate was ≥ 0.028 g / day were considered suitable. No unsuitable areas were found.

4.6. Growth Rate Variability in the Optimal Zone

The growth rate variability in the optimal zone (Figure 60 c) during years 2011 - 2020 for 5- and 8 cm mussels, respectively is presented in Figure 65. Annual variations are present with one high growth rate period and one low growth rate period per annual circle. The values for highest and lowest growth rates remain similar over the decade but whereas the lowest value remain approximately the same for 5- and 8 cm mussels, the growth rate tops for 8 cm mussels are approximately twice as high as those of 5 cm mussels.

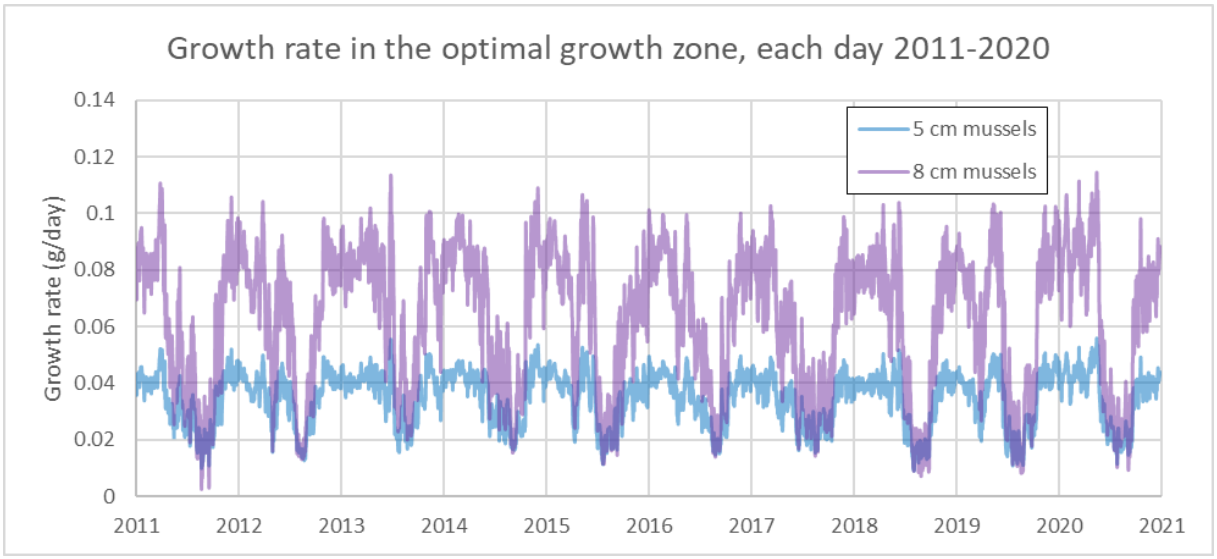

Figure 65: Growth rate in optimal zone each day 2011 - 2020.

The monthly variability is presented in Figure 66 and Figure 67. Whereas some interannual variability is present, so is a clearly discernible pattern with lower growth rates in summer and higher growth rates in winter.

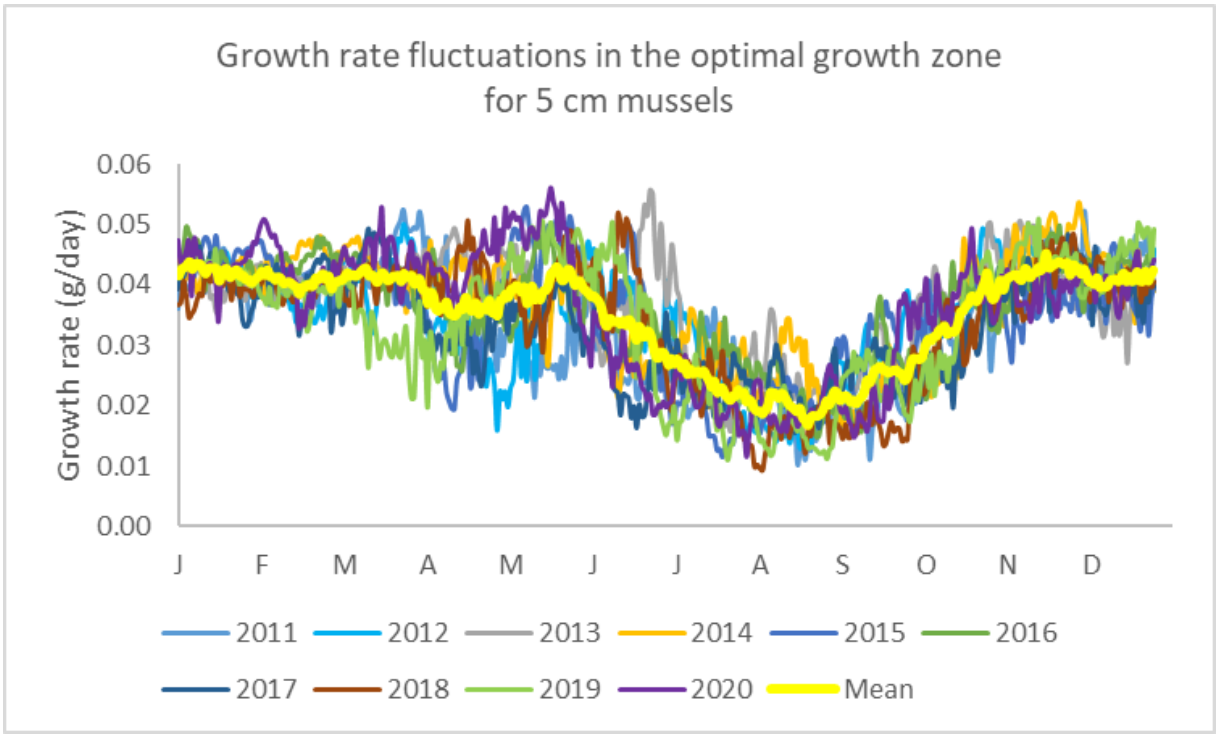

Figure 66: Growth rate fluctuations 5 cm mussels in the optimal zone for years 2011-2020.

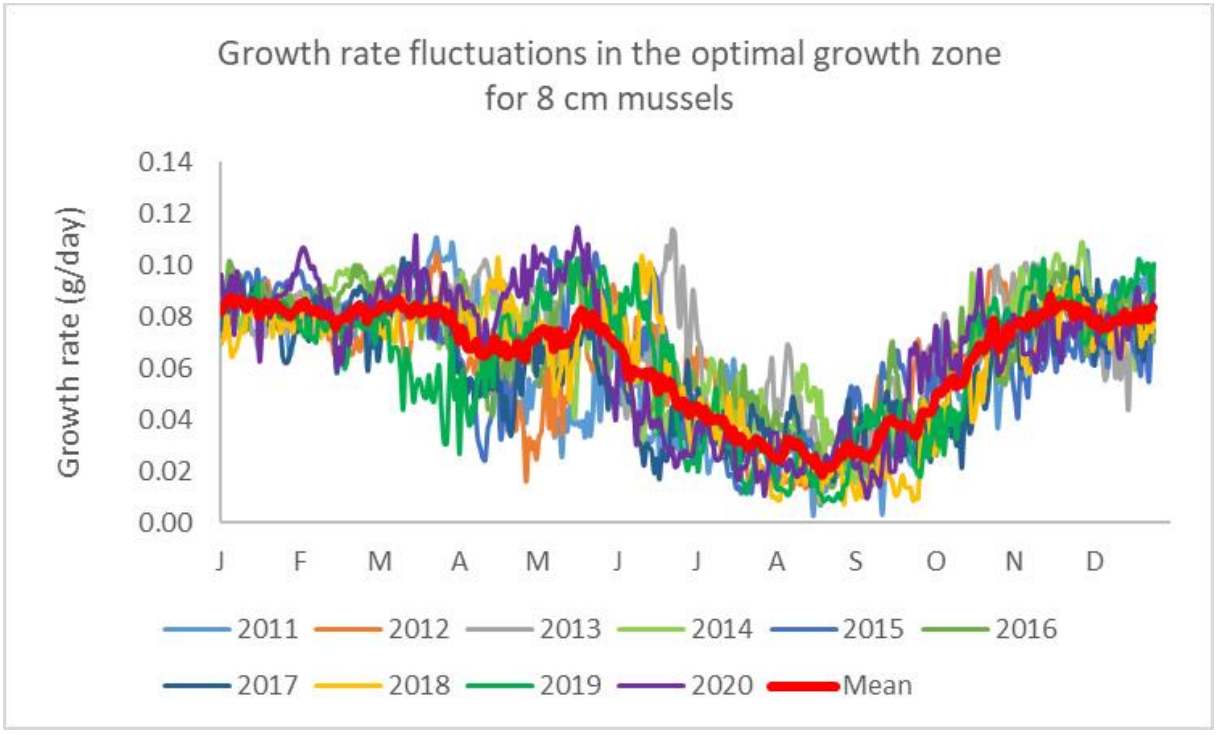

Figure 67: Growth rate fluctuations 8 cm mussels in the optimal zone for years 2011-2020.

As can be seen in the graph of decennial means for 5- and 8 cm mussels, presented in Figure 68, the low growth season spans from June to October, with growth rates < 0.028 g / day present from July to September.

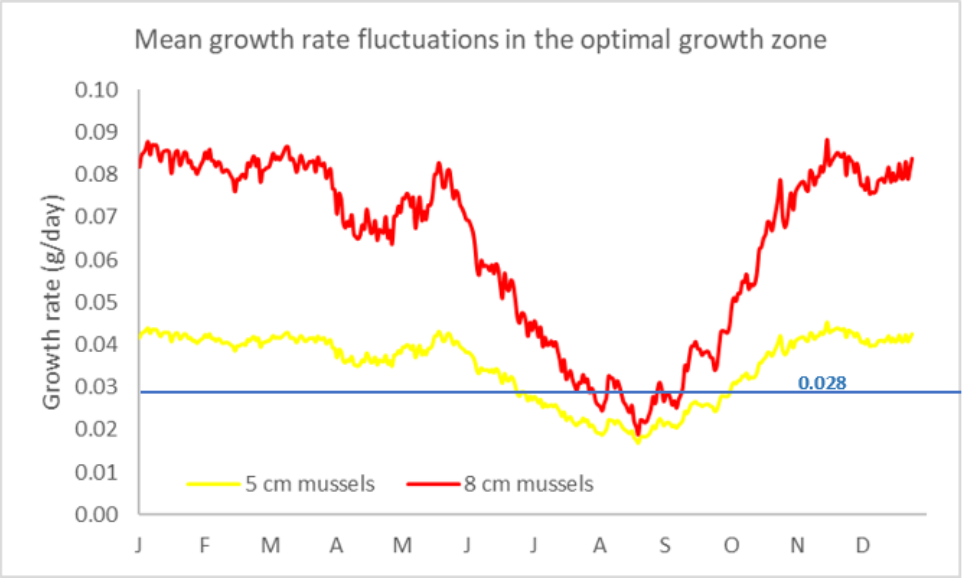

Figure 68: Mean growth rate fluctuations in the optimal zone for years 2011-2020.

5. Discussion

5.1. Calibration

Six parameters (T_H, X_k, δ_m, SST, chl *a* and $[\dot{p}_M]_m$) were calibrated (i.e., their accuracy and precision investigated) but only one parameter was adjusted, namely X_k. The value for X_k that created the best fit between the modelled and the measured values in the method validation was lower than values found in literature: 5.33 mg C / m^3, to be compared to 194 mg C / m^3 for Casas and Bacher (2006), in addition to 28 mg C / m^3 and 36 mg C / m^3 for Hatzonikolakis et al. (2017). The large difference between the two earlier studies, in addition to X_k being a commonly calibrated and adjusted parameter, perhaps the most commonly calibrated and adjusted DEB parameter, indicates that a X_k of 5.33 may be plausible even though it is lower than X_k values found before. A higher X_k is expected where primary production is generally higher. Perhaps a lower X_k on the French Riviera in 2015 - 2018 compared to 2006 is due to less eutrophication of coastal waters following improved wastewater treatment. In addition, the X_k calibrated in the present study was based on 48 sample spots, whereas Casas and Bacher (2006) only used 3. The oligotrophic conditions off the French Riviera and around Corsica most likely influenced X_k towards a much lower value. Ideally, X_k should be based on proxies or sample spots that are truly representative for the modelled area. Perhaps different X_k are necessary for a study area as large as the French Mediterranean EEZ. It is imaginable to have one X_k each for the GoL, the Corso-Ligurian basin, the Ligurian Sea, the coast of Corsica and the French Riviera.

The model accuracy for the validation of the new value for X_k was slightly different than the calibration one. The R^2 and the intercept were better in the calibration, but the slope was better in the validation. Some difference in accuracy between calibration and validation is to be expected since they are based on different GCPs. In addition, the two were sufficiently similar for the calibration to be validated.

The calibration of T_H did not result in an indication that adjusting the parameter would increase model accuracy, which is consistent with Hatzonikolakis et al. (2017) and Casas and Bacher (2006), who successfully applied the baseline value for *M. galloprovincialis*. However, literature indicates that the growth rate of *M. galloprovincialis* should increase with increasing SST up to at least 24 °C, whereas the growth rate, as modelled using the DEB model, increases with increasing SST up to 19 °C, after which the growth rate starts to decline. More research is needed regarding the DEB model temperature parameters for *M. galloprovincialis* acclimated to Mediterranean conditions.

Error for input factor δ_m was the only input factor whose error had an impact on output for measured growth (Figure 36). The output for measured growth is impacted since the DEB theory uses δ_m to estimate initial mussel wet weight from mussel length.

The input variable SST has little impact on model precision since its RMSD constant, 0.408 °C (the same number as when measured in K), is smaller by three orders of magnitude compared to the actual values for SST in the area, which for the years 2011 - 2020 range from 9.390 -

29.730 °C, and has a mean of 18.093 °C. It is therefore not surprising that output variability due to SST error is small.

The input variable chl *a*, on the other hand, has a more important impact. Its RMSD of 0.266 mg / m^3 is in the same order of magnitude as the mean values of chl *a*, which for the years 2011 - 2020 was 0.209 mg / m^3. The range of chl *a* values for the same period was 0.005 - 654.073 mg / m^3. As can be seen in Figure 55 and Figure 56, the impact of chl *a* level diminished drastically for chl *a* values above 1 mg / m^3 to eventually cease completely when the mussels reach their maximum feeding level. In addition, the uncertainty for chl a is a constant and the error is therefore large when the measured value for chl a is low. This is in line with the growth modelling by Rosland et al. (2009), which corresponded well with in situ measurements when chl *a* was abundant but not in laboratory experiments when food was scarce. Chl *a* error is therefore likely to impact model precision in areas with low chl *a*.

Hence, even though the range of values for chl *a* is wide, indeed wider than the range of values for SST, the impact on growth rate will be high only for the approximate range of chl *a* values from 0 – 1 mg / m^3. Considering that mean value for chl *a* is low, even though the maximum is approximately $2*10^3$ times higher, an important part of the actual cell values for chl *a* are expected to fall within the range for which its error has a noticeable impact on growth rate. It is therefore not surprising that potential error in chl *a* decreases the model accuracy more than the potential error for SST.

In the primary OAT-analysis, the potential change in output due to error in chl *a* was 0.4140 whereas in the re-evaluation, the corresponding value was 3.8105. The difference between the two values for potential change, where the re-evaluation value is 9.2041 times larger than the corresponding value for the initial analysis, seems large but they are not to be compared directly. To better evaluate the difference, it is useful to compare the potential output change to the span of the actual output. The span of output values in the initial OAT-analysis was 1.9058. The span of the output in the re-evaluation was 5.4747, i.e., 2.8727 times larger than for the initial analysis. The potential change in output relative to the output span is thus 3.2040 times larger for the re-evaluation than for the initial OAT-analysis.

The remaining difference between the two is considerable as well as logical. One of the changes imposed by a lower X_k is that the model output becomes more influenced by chl *a* fluctuations, whereas a higher X_k results in a model output that is more influenced by SST fluctuations. Hence, any potential error in chl *a* will have a stronger influence on model output for lower values of X_k.

In the initial OAT-analysis, an important change in output due to error for input factor $[\dot{p}_M]_m$ was detected. As seen in Figure 36, a higher value for $[\dot{p}_M]_m$ made the model more accurate whereas a lower value made the model less accurate. This may be an effect of the high temperatures in the Mediterranean. The values for $[\dot{p}_M]_m$ ranges from 12 to 26 within the temperature span of 10 °C to 20 °C. The constant value used in the present study is 24. However, waters close to shore in the French Mediterranean are often 25 °C in summertime and 16 °C in

wintertime. It is possible that a $[\dot{p}_M]_m$ value of 24 is too low for the conditions of the RINBIO in situ points. This would also explain why the model accuracy is not clearly ameliorated by an adjusted $[\dot{p}_M]_m$ in the re-evaluation since, a lower X_k diminishes the effects of fluctuating SSTs on model output.

Based on the accuracy results from the re-evaluation, i.e., the evaluation of the adjusted DEB equation, the model, as conducted in the present study, is deemed to be an adequate tool for discerning suitable and less suitable areas for mussel cultivation. This is supported by the R^2, slope and intercept of the y-axis of the scatter plot comparing measured growth and growth modelled with a calibrated and adjusted DEB model in Excel (Figure 35).

In previous studies, growth modelled using the DEB theory has been shown to be highly accurate. Several studies have found that, after calibration, the modelled values all fall within 10 % of the measured ones. In the present study, the precision was much lower, including modelled values more than twice as high as the corresponding measured ones. The main difference between previous studies and the present one is that earlier articles researched one or a small number of spots and collected GCP data themselves, whereas the present study analysed a large continuous area with GCP data from a third party.

In situ measurements are a valuable tool to test the exactitude of a model but often requires large investments of time and money. In an attempt to efficiently validate the model within the allotted time frame and budget, in situ measurements from a third party were compared to the model results. While majorly reducing the workload, an inherent disadvantage of using pre-existing sampling data is that it cannot be adapted according to the needs of subsequently planned and executed research. For example, no sample spots were located offshore, which was the main interest for the analyses. If conditions onshore and offshore are very different, a calibration using only onshore measurements may be misleading.

The mussels used for the in situ data were measured differently before versus after submersion. Values for the initial RINBIO mussel parameters (weight, E, R) are based on the assumption that planted mussels were all homogenous and 50 mm long when first put in the water. It is not described in the data how the selection of initial mussels is done (e.g., if they are measured by hand or selected by a machine) nor what the margin of error is (e.g., the range of lengths accepted in the samples). In addition, no dry weight or dry matter were tested on a subsample of the mussels before submersion. Once the mussels are taken out of the water, their length was not recorded but dry weight and dry matter was analysed. This means that a conversion equation is needed to compare the initial length with the resulting dry weight. The quality of the in situ values hence depends on the quality of the initial measurements as well as the quality of the conversion equation, both of which are unknown.

The RINBIO mussels were submerged approximately three months. It is a reasonable assumption that there is a time of adjustment for the mussels when they are transferred to a new area. The exact length of the adjustment period is unknown but may have contributed to the difference in modelled vs measured growth.

A mentioned, the field work, time and organisation required to observe mussel growth in situ is extensive, especially for larger areas such as the French Mediterranean. The need for input data such as in situ measurements are one of the reasons that the DEB theory had been criticized for being complicated to apply (Jager et al. 2014). An alternative to in situ observations may be proxies for the parameters that are site specific. Such proxies are currently not available but constitute an interesting topic for future research.

The parameter δ_m defines the relationship between the length of the mussel's shell and the volume of its soma. While δ_m varies greatly between species, it also varies within the same species, seemingly depending on the wave action present in its growth area (Steffani and Branch 2003). The more waves, the more hydrodynamic and flatter the mussels develop to be and δ_m subsequently decreases. More research regarding the link between δ_m and wave action (i.e., turbidity) is useful for finding a proxy for δ_m and simplifying the use of DEB theory in Mediterranean mussels.

The ratio of chl *a* : Phyto-C (relevant for the IMTA scenario) is important to the use of chl *a* as a proxy for phytoplankton density and constitutes another parameter that may change depending on the specific site where it is used. Graff et al. (2015) compared ratios between Phyto-C and chl *a* in various seawater conditions, from oligotrophic gyres to upwelling systems and temperate spring conditions in the Atlantic and Pacific Oceans. The authors found a large spread in ratio values, with the maximum ratio value being ten times larger than the minimum ratio value. This is likely due to the fact that different species of phytoplankton contain different levels of carbon and chl *a*. For example, Kormas et al. (2002) studied phytoplankton species composition and contribution to POC and chl *a* in the Malaikos Gulf in Greece and found that the smaller fractions pico- and nanoplankton were important contributors to the POC levels but added little to the chl *a* concentrations. Further investigations should be conducted to estimate the Phyto-C : chl *a* ratio based on environmental variables such as phytoplankton species composition (Filgueira et al. 2011). Such a model could be applied to different ecosystems without the need for calibration and constitute an appropriate tool to predict exact mussel growth over a large area with varying chl *a* levels.

In addition to phytoplankton, mussels may obtain sustenance from other sources, such as suspended detritus. Therefore, chl *a* alone may not be a sufficient proxy for food availability and including detritus may increase model accuracy. Detritus wasn't considered since Hatzonikolakis et al. (2017) found very little difference between his models that did vs. did not simulate POC (which can be considered a rough approximation of detritus when measured in parallel with chl *a*). In the light of the relatively low correlation between measured and modelled growth in the present study, detritus and thus the POC concentration may have a more important effect on mussel growth on the French Mediterranean coast compared to the Greek sites surveyed by Hatzonikolakis et al. (2017).

This is in line with the results of Rosland et al. (2009), which indicate that chl *a* has limitations as a food proxy for blue mussels. It is also in line with Handa et al. (2011), who used the DEB model to study the fit of different food proxies (Total Particulate Matter, POM, Organic Content

and chl *a*) at three longline mussel (*M. edulis*) farms in central Norway and concluded that the optimal food proxy depended on location. While proxies at the two farms further away from shore showed only minor differences in fit, the farm closest to shore experienced the best fit between modelled and measured growth when the food proxy used was organic content whereas chl *a* gave the poorest fit. Similarly, Page and Hubbard (1987) found that variation in mussel (*M. edulis*) growth at a depth of 9 meters under an offshore platform in the Santa Barbara Channel in California was more closely associated with POC concentrations than with chl *a*. More research is needed to understand the complex relations between, and find better proxies for, mussel food availability vs. chl *a*- and POC concentrations.

In homogenous areas offshore, where bathymetry does not influence turbidity, and where inorganic matter from river runoff does not interfere with filter feeding, X_k and δ_m should be stable and any uncertainty caused by them could be either avoided or reduced to insignificant levels, largely increasing the predictability of mussel growth even in the absence of proxies and using only a few in situ observation sites. The fieldwork and testing needed for model calibration and validation would be less extensive than for coastal sites where bathymetry-driven turbidity and POC complicates the growth pattern. During such circumstances, an SST- and chl *a* driven DEB-model for offshore mussel cultivation has the potential to accurately predict mussel growth over a large area without proxies and with few in situ observations.

5.2. Historical Growth

Based on the adjusted DEB model, calibrated and applied as described in previous sections, a conservative estimation of what area in the offshore French Mediterranean EEZ was suitable for mussel cultivation every year during the decade 2011 - 2020 is most of the GoL, as visible in Figure 46. This is in line with the location of most current mussel farms, which are also placed in the GoL. Whereas mussel cultivations are currently present and functional off the coast of Corsica, they are located in ponds on the coastline in waters that are much shallower than 30 m. The mussel farming on Corsica is therefore located outside of the study area and its presence hence does not contradict the results indicating that the offshore area around Corsica is considered unsuitable for mussel farming.

The suitability in the GoL coincides with the bay's bathymetry: suitable areas are located on the shallower ocean bottom shelf and unsuitable areas begin as the shelf ends and the sea depth rapidly increases. These higher growth rates and shallow bathymetry detectable in the Gulf of Lion compared to the Ligurian Sea are likely co-dependent via the creation of dense water formation and subsequent mixing of the water column in the shallower Gulf of Lion. The river Rhône brings nutrients from land that allows for growth at its outflow and thus adds to the more favourable conditions.

5.3. Climate Change Scenario

5.3.1. Chl a

Whereas, given the currently available scientific literature, it is difficult to say how climate change will affect chl *a* levels in the French Mediterranean, the best analyses available indicate that the change will be small. Nevertheless, a potential decrease in chl *a* should be considered

when choosing a location for mussel cultivation. Given the current limitations in data availability for chl *a* in climate change predictions, this is best done by restricting spots to areas where chl *a* is currently abundant. The best analysis for what areas will exhibit sufficient chl *a* in the future is thus to look at historical data. As seen in Figure 45, where different areas are due to chl *a* fluctuations, data from 2011 - 2020 indicate that such areas are found in the GoL. This is in line with chl *a* data from 1998-2020 in Figure 56, which clearly indicated that GoL has vastly less days with chl *a* levels that are lower than what is needed for optimal mussel growth, compared to the rest of the study area.

5.3.2. SST

Predictions for SST variations due to climate change, on the other hand, are readily available and were used to model climate change impact on mussel growth. As can be seen in Figure 54, the climate change modelling, conducted as described in previous sections, indicate that the best areas for mussel cultivation at the end of this century, with respect to SST and with respect to climate change scenario RCP 8.5 Long Term, will mainly be located in the western half of the GoL. This is likely due to the colder waters entering the GoL from upwelling and river output. The colder waters offset the negative impact of higher SSTs, which impair mussel growth when too high.

It is important to note that, although the model includes more daily variability than the original IPCC rasters, the predicted SSTs are based on SST increase data that was added to historical data and the SST increase data are in the form of monthly means. Thus, the modelling entails an exclusion of some daily variability since it is possible that the SST increase is not evenly distributed over the entire month. For example, warmer days may have a higher SST increase than colder days, or vice versa. Investigating the possible variability in SST increase by applying it in proportion to the baseline SST may have resulted in further insights but was decided against due to time restrictions.

Ideally, the historical SST rasters from 1995-2014 would be used. A more time efficient alternative was opted for; namely, to model the warmest year during the IPCC reference period, allowing for a conservative estimation of future viability and suitability of cultivation areas, albeit at a loss of variation information. Since only one baseline year (2014) was used, it is unknown whether the monthly distribution of suitable SSTs presented in Figure 51, with a period less suitable for growth from June to October, with July to September being particularly unsuitable, is typical or not. However, the results are in line with the findings from historical data, as is visible in the yearly growth rate fluctuations in Figure 67, which indicate declining growth rates in June with the lowest rates in August followed by an increase until pre-June levels are reached in November.

5.4. IMTA Scenario

Support was found for the hypothesis that waste from a fish farm may sustain mussel farming in its proximity. The adjusted DEB equation, modelled as described in previous sections, indicated, in a conservative estimation, that growing mussels in an IMTA scenario in otherwise

nutrient poor waters were feasible in the entire study area every year during the decade 2011 - 2020.

In addition, it is possible that waste from fish farms that are not characterised by containing chl *a* may be present and act as an additional food source. Macdonald et al. (2011) found that blue mussels (*M. edulis*) grew better in an IMTA system with Salmon even though the chl *a* remained the same around the fish farms compared to the control station further away. This was believed to be due to an increase in POM that was not reflected in primary production but that did serve as food for the mussels. More research is needed in the subject of IMTA, notably regarding the amount of mussel food a fish farm produces and finding a proxy to measure it, preferably remotely to facilitate for farmers.

5.5. Combination Scenarios

As seen in Figure 60, a conservative estimation of mussel growth, as modelled by the adjusted DEB model described in an earlier section, indicated that approximately half the area that were suitable for mussel growth every year 2011 - 2020 will continue to be suitable until at least the end of this century, even in the event of climate change scenario RCP 8.5. The half considered is the western half of the GoL and is referred to as the optimal growth zone.

Although some areas will exhibit less than optimal (although not deadly) SSTs, the entirety of the study area will continue to be suitable for mussel cultivation as part of an IMTA since the mean yearly growth rate is expected to remain above 0.028 g / day.

Growth rate fluctuates during the year. Whereas larger mussels experience greater magnitudes in their fluctuations, the timing concurs with smaller mussels: higher growth November through May, less growth in June and October, and low growth in July through September. Interestingly, the growth rate magnitude difference between mussel sizes is large when growth rate is high but small to inexistant when growth rate is low. This indicates that all mussels have a low growth rate level in common.

6. Conclusion

The adjusted DED model, as executed in the present study, indicate that the offshore areas in the French Mediterranean EEZ that are most suitable for mussel farming now and in the future is the western half of the GoL.

The proposition made (i.e., the optimal areas proposed) is conservative and does not exclude the possibility of additional areas being viable for mussel cultivation. However, the area is sufficiently large for being interesting for further examination with regards to farmers' priorities such as distance to ports, environmental priorities such as marine protected areas, and other industries' priorities such as fishing ground and shipping routes.

According to additional analyses, IMTAs may provide a solution in areas where primary production is low. In addition to increasing the cultivatable area for mussel farms, integrating

bivalves in IMTAs is promising as a mean to partially mitigate the environmental impact of pisciculture.

The use of DEB-theory in a GIS environment to find suitable areas for bivalve cultivation is a recent development in aquaculture research and has mainly been applied for oysters in the Atlantic. Barillé et al. (2020) used the DEB-model to map oyster growth in the French Atlantic and found that oyster growth corresponded well with chl *a* levels, similar to the finding that mussel growth partially corresponds to chl *a* levels in the present study. The authors also found a seaward decrease in chl *a* levels, much like the one found in the north-western Mediterranean, and less variation in areas with higher growth, which is consistent with the OAT-analysis in the present study, indicating that chl *a* was less variable for higher values.

This is the first study to use DEB-theory and GIS to map growth in the Mediterranean and for the Mediterranean mussel. The study shows that DEB-modelling of growth over large heterogenous areas is possible, something that has major implications for aquaculture in general since it facilitates cultivation activities such as site selection as well as the timing of seeding and harvest. The combined DEB/GIS method also has the potential to constitute a useful tool when calculating optimal food concentration for maximal growth in IMTAs, alternatively to calculate optimal placement and concentration of mussels to counter eutrophication from fish farms.

This first study has illustrated the potential for improvement in the DEB-model since the model, although it was judged to be sufficiently accurate, did not reach the high accuracy levels of previous research. Several method adjustments can be made to potentially increase model performance. POC should be considered as a food proxy. More research is needed to define temperature parameters (e.g., T_H) by experiments using *M. galloprovincialis* acclimatised to temperatures applicable for the Mediterranean Sea. The parameter $[\dot{p}_M]_m$ should be adapted depending on temperature and more research is needed regarding its values for temperatures above 20 °C. Modelling in R or MATLAB would facilitate using $[\dot{p}_M]_m$ as a variable dependent on SST rather than as a constant and is recommended for future projects. With regards to IMTAs, more research is needed on the issue regarding the amount of Phyto-C added to the water from Mediterranean open pen fisheries.

The study highlighted issues that spring from adapting the DEB model to a GIS environment. When modelling growth in one location or a larger homogenous area, using second hand in situ observations may decrease the accuracy of the model. To enable modelling over large heterogenous areas in a GIS environment, proxies may be needed for each parameter. Future research should focus on finding such proxies. To reach the objective of accurately modelling mussel growth offshore, in conditions where X_k, δ_m and the chl a : Phyto-C ratio may vary less, it is possible that both approaches mentioned above (parameter calibration and proxies) are valid for future research.

References

Alonso-González, I. J., J. Arístegui, J. C. Vilas, and A. Hernández-Guerra. 2009. Lateral POC transport and consumption in surface and deep waters of the Canary Current region: A box model study. *Global Biogeochemical Cycles,* 23**:** GB2007. DOI: 10.1029/2008gb003185

Alunno-Bruscia, M., Y. Bourlès, D. Maurer, S. Robert, J. Mazurié, A. Gangnery, P. Goulletquer, and S. Pouvreau. 2011. A single bio-energetics growth and reproduction model for the oyster Crassostrea gigas in six Atlantic ecosystems. *Journal of Sea Research,* 66**:** 340-348. DOI: 10.1016/j.seares.2011.07.008

Anestis, A., A. Lazou, H. O. Portner, and B. Michaelidis. 2007. Behavioral, metabolic, and molecular stress responses of marine bivalve Mytilus galloprovincialis during long-term acclimation at increasing ambient temperature. *Am J Physiol Regul Integr Comp Physiol,* 293**:** R911-921. DOI: 10.1152/ajpregu.00124.2007

Anestis, A., H. O. Portner, D. Karagiannis, P. Angelidis, A. Staikou, and B. Michaelidis. 2010. Response of Mytilus galloprovincialis (L.) to increasing seawater temperature and to marteliosis: metabolic and physiological parameters. *Comp Biochem Physiol A Mol Integr Physiol,* 156**:** 57-66. DOI: 10.1016/j.cbpa.2009.12.018

Arnott, D. L., and M. J. Vanni. 1996. Nitrogen and phosphorus recycling by the zebra mussel (Dreissena polymorpha) in the western basin of Lake Erie. *Canadian Journal of Fisheries and Aquatic Sciences,* 53**:** 646-659. DOI: 10.1139/cjfas-53-3-646

Bardot-Cambot, A., and V. Forest. 2013. Ostréiculture et mytiliculture à lépoque romaine? Des définitions modernes à l'épreuve de l'archéologie. *Presses Universitaires de France,* 2913/2**:** 367-388. DOI: 10.3917/arch.132.0367

Barillé, L., A. Le Bris, P. Goulletquer, Y. Thomas, P. Glize, F. Kane, L. Falconer, P. Guillotreau, et al. 2020. Biological, socio-economic, and administrative opportunities and challenges to moving aquaculture offshore for small French oyster-farming companies. *Aquaculture,* 521. DOI: 10.1016/j.aquaculture.2020.735045

Barnabé, G., and F. Doumenge. 2001. Mariculture of Mediterranean Species. In *Encyclopedia of Ocean Sciences,* 1567–1572. Elsevier Ltd.

Bearham, D., M. Vanderklift, R. Downie, D. Thomson, and L. Clementson. 2020. Macrophyte-derived detritus in shallow coastal waters contributes to suspended particulate organic matter and increases growth rates of Mytilus edulis. *Marine Ecology Progress Series,* 644**:** 91-103. DOI: 10.3354/meps13314

Borchardt, T. 1985. Relationships between carbon and cadmium uptake in Mytilus edulis. *Marine Biology,* 85**:** 233-244. DOI: 10.1007/bf00393243

Bouchoucha, M., C. Tomasino, I. Amouroux, B. Andral, C. Brach-Papa, M. Briand, R. Buchet, L. Delmas, et al., 2021. 20 ans de suivi de la contamination chimique des eaux côtières méditerranéennes. Résultats & perspectives. Ifremer Report 90 pp.

Bratt, J., 2013. Framtagande av lämpliga områden för musselodling med GIS. Länsstyrelsen i Västra Götalands län Report 24, (Länsstyrelsen 2013:57).

Buck, B. H., M. W. Ebeling, and T. Michler-Cieluch. 2010. Mussel cultivation as a co-use in offshore wind farms: Potential and economic feasibility. *Aquaculture Economics & Management,,* 14**:** 255-281. DOI: 10.1080/13657305.2010.526018

Casas, S., and C. Bacher. 2006. Modelling trace metal (Hg and Pb) bioaccumulation in the Mediterranean mussel, Mytilus galloprovincialis, applied to environmental monitoring. *Journal of Sea Research,* 56**:** 168-181. DOI: 10.1016/j.seares.2006.03.006

Cattaneo-Vietti, R., E. Trainito, and M. Doneddu. 2016. *Man and Shells Molluscs in the History*. Bentham Science Publishers.

Ceccherelli, V., and R. Rossi. 1984. Settlement, growth and production of the mussel Mytilus galloprovincialis. *Marine Ecology Progress Series,* 16**:** 173-184. DOI: 10.3354/meps016173

Cheney, D., R. Langan, K. Heasman, B. Friedman, and J. Davis. 2010. Shellfish Culture in the Open Ocean: Lessons Learned for Offshore Expansion. *Marine Technology Society Journal,* 44**:** 55-67. DOI: 10.4031/mtsj.44.3.6

Chever, T., A. G. Herry, and S. SOUIDI, 2021. Etude sur le marché de la moule fraîche en France et spécifiquement sur la filière francaise moule de bouchot. FranceAgriMer Etablissement Naional des Produits de l'Agriculture et de la Mer Report 55 pp.

Copernicus. 2021a. Mediterranean Sea High Resolution and Ultra High Resolution Sea Surface Temperature Analysis. Retrieved 10/11/2021 2021, from. https://resources.marine.copernicus.eu/product-download/SST_MED_SST_L4_NRT_OBSERVATIONS_010_004

Copernicus. 2021b. Mediterranean Sea Monthly and Daily Reprocessed Surface Chlorophyll Concentration from Multi Satellite observations + SeaWiFS daily climatology. Retrieved 10/11/2021 2021, from. https://resources.marine.copernicus.eu/product-detail/OCEANCOLOUR_MED_CHL_L4_REP_OBSERVATIONS_009_078/INFORMATION

Cordex. 2021. WCRP CORDEX Coordinated Regional Climate Downscaling Experiment. Retrieved 10/11/2021 2021, from. https://cordex.org/

CRCM. 2022. Comité Régional de Conchyliculture de Méditerranée. Retrieved Jan 17, 2022 2022, from. https://www.huitresdemediterranee.fr/

Creative Commons. 2022. Creative Commons Licenses. Retrieved May 17th 2022 2022, from. https://creativecommons.org/

Crosetto, M., and S. Tarantola. 2010. Uncertainty and sensitivity analysis: tools for GIS-based model implementation. *International Journal of Geographical Information Science,* 15**:** 415-437. DOI: 10.1080/13658810110053125

Danovaro, R., C. Gambi, G. M. Luna, and S. Mirto. 2004. Sustainable impact of mussel farming in the Adriatic Sea (Mediterranean Sea): evidence from biochemical, microbial and meiofaunal indicators. *Marine Pollution Bulletin,* 49**:** 325-333. DOI: 10.1016/j.marpolbul.2004.02.038

Dauda, A. B., A. Ajadi, and A. S. Tola-Fabunmi. 2020. Waste in aquaculture: Part 1 Global Aquaculture Qdvocate. Retrieved 01/12/2021 2021, from. https://www.globalseafood.org/advocate/waste-in-aquaculture-part-1/

Dauda, A. B., A. Ajadi, A. S. Tola-Fabunmi, and A. O. Akinwole. 2019. Waste production in aquaculture: Sources, components and managements in different culture systems. *Aquaculture and Fisheries,* 4**:** 81-88. DOI: 10.1016/j.aaf.2018.10.002

Department of Fisheries Government of Kerala. 2021. *Package of Aquaculture practices*. Thiruvananthapuram: Government of Kerala.

ArcGIS Pro 2.7.3. Redlands, California, the United States of America.

European Commission. 2022. European Marine Observation and Data Network (EMODnet). Retrieved Jan 15th 2020 2022, from. https://emodnet.ec.europa.eu/en

European Commission Joint Research Centre. 2022. European Commission Joint Research Centre Homepage. Retrieved May 17th 2022 2022, from. https://ec.europa.eu/info/departments/joint-research-centre_en

Falconer, L., T. C. Telfer, and L. G. Ross. 2016. Investigation of a novel approach for aquaculture site selection. *Journal of Environmental Management,* 181**:** 791-804. DOI: 10.1016/j.jenvman.2016.07.018

FAO. 2012. Vue générale du secteur aquacile national France. Retrieved 01/12/2021 2021, from. https://www.fao.org/fishery/countrysector/naso_france/fr

FAO, 2018. Strategy for the sustainable development of Mediterranean and Black Sea aquaculture – Three targets, Selected outputs, Proposed activities. Food and Agriculture Organization of the United Nations (FAO), General Fisheries Commission for the Mediterranean (GFCM), Report, Rome, 20 pp.

FAO. 2020. *The State of World Fisheries and Aquaculture 2020*.

FAO, 2021a. GLOBEFISH European Price Report. BLOBEFISH Trade and Marked Tean (NFIMT) Fisheries and Agriculture Division Food and Agriculture Organization of the United Nations, Report, Italy.

FAO. 2021b. Mytilus galloprovincialis. Cultured Aquatic Species Information Programme. Text by Figueras, A. Fisheries and Aquaculture Division. [Online]. Rome. Retrieved 13/12/2021 2021, from.

https://www.fao.org/fishery/docs/DOCUMENT/aquaculture/CulturedSpecies/file/en/en_mediterraneanmussel.htm
FAO. 2022. Mussel farming: a food system with minimal greenhouse gas emissions. Retrieved Jan 15th, 2022 2022, from. https://www.fao.org/climate-smart-agriculture-sourcebook/production-resources/module-b4-fisheries/b4-case-studies/case-study-b4-3/en/
Filgueira, R., R. Rosland, and J. Grant. 2011. A comparison of scope for growth (SFG) and dynamic energy budget (DEB) models applied to the blue mussel (Mytilus edulis). *Journal of Sea Research,* 66**:** 403-410. DOI: 10.1016/j.seares.2011.04.006
Flanders Marine Institute. 2019. Maritime Boundaries Geodatabase: Maritime Boundaries and Exclusive Economic Zones (200NM), version 11. Retrieved 2021-11-25 2021, from. https://www.marineregions.org/
French Ministry of Ecology. 2013. Aquaulture. DICOM-CGDD/CRE/13040. In *Assises de la mer et du littoral: Une ambition francaise pour la politique maritime intégrée*, 3. Commissariat général au développement durable (CGDD).
Froehlich, H. E., A. Smith, R. R. Gentry, and B. S. Halpern. 2017. Offshore Aquaculture: I Know It When I See It. *Frontiers in Marine Science,* 4. DOI: 10.3389/fmars.2017.00154
Fuentes-Santos, I., U. Labarta, M. J. Fernandez-Reiriz, S. Kay, S. S. Hjollo, and X. A. Alvarez-Salgado. 2021. Modeling the impact of climate change on mussel aquaculture in a coastal upwelling system: A critical assessment. *Sci Total Environ,* 775**:** 145020. DOI: 10.1016/j.scitotenv.2021.145020
Geider, R. J., and T. Platt. 1986. A mechanistic model of photoadaptation in microalgae. *Marine Ecology Progress Series,* 30**:** 85-92.
Godfray, H. C. J., J. R. Beddington, I. R. Crute, L. Haddad, D. Lawrence, J. F. Muir, J. Pretty, S. Robinson, et al. 2010. Food Security: The Challenge of Feeding 9 Billion People. *Science,* 327**:** 812-818. DOI: 10.1126/science.1185383
Gosling, E. M. 1984. The systematic status of Mytilus Galloprovincialis in Western Europe: a review. *Malacologia,* 25**:** 551-568.
Graff, J. R., T. K. Westberry, A. J. Milligan, M. B. Brown, G. Dall'Olmo, V. V. Dongen-Vogels, K. M. Reifel, and M. J. Behrenfeld. 2015. Analytical phytoplankton carbon measurements spanning diverse ecosystems. *Deep Sea Research Part I: Oceanographic Research Papers,* 102**:** 16-25. DOI: 10.1016/j.dsr.2015.04.006
Haamer, J. 1996. Improving water quality in a eutrophied fjord system with mussel farming. *Ambio,* 25**:** 356-362.
Handa, A., M. Alver, C. V. Edvardsen, S. Halstensen, A. J. Olsen, G. Oie, K. I. Reitan, Y. Olsen, et al. 2011. Growth of farmed blue mussels (Mytilus edulis L.) in a Norwegian coastal area; comparison of food proxies by DEB modeling. *Journal of Sea Research,* 66**:** 297-307. DOI: 10.1016/j.seares.2011.05.005
Handa, A., H. J. E. Min, X. X. Wang, O. J. Broch, K. I. Reitan, H. Reinertsen, and Y. Olsen. 2012. Incorporation of fish feed and growth of blue mussels (Mytilus edulis) in close proximity to salmon (Salmo salar) aquaculture: Implications for integrated multi-trophic aquaculture in Norwegian coastal waters. *Aquaculture,* 356**:** 328-341. DOI: 10.1016/j.aquaculture.2012.04.048
Hatzonikolakis, Y., K. Tsiaras, J. A. Theodorou, G. Petihakis, S. Sofianos, and G. Triantafyllou. 2017. Simulation of mussel Mytilus galloprovincialis growth with a dynamic energy budget model in Maliakos and Thermaikos Gulfs (Eastern Mediterranean). *Aquaculture Environment Interactions*, 9**:** 371-383. DOI: 10.3354/aei00236
Higueras, M., P. Kerhervé, A. Sanchez-Vidal, A. Calafat, W. Ludwig, M. Verdoit-Jarraya, S. Heussner, and M. Canals. 2014. Biogeochemical characterization of the riverine particulate organic matter transferred to the NW Mediterranean Sea. *Biogeosciences,* 11**:** 157-172. DOI: 10.5194/bg-11-157-2014
Holling, C. S. 1959. Some Characteristics of Simple Types of Predation and Parasitism. *The Canadian Entomologist,* 91**:** 385-398. DOI: 10.4039/ent91385-7
IFREMER. 2011. Quels types de pêche pratiquent-ils? Classification officielle. Retrieved 26/11/2021 2021, from. https://wwz.ifremer.fr/peche/Le-monde-de-la-peche/La-peche/Laquelle
IFREMER. 2021. Quadrige^2. Retrieved October 10 2021, from. https://wwz.ifremer.fr/surval/

Institute of Medicine. 2007. *Seafood Choices: Balancing Benefits and Risks*. Washington, DC: The National Academies Press.
IPCC. 2021a. IPCC WGI Interactive Atlas: Regional information (Advanced). Retrieved 10/11/2021 2021, from. https://interactive-atlas.ipcc.ch/regional-information
IPCC, 2021b. Summary for Policymakers. Report 42 pp.
Jager, T., A. Barsi, N. T. Hamda, B. T. Martin, E. I. Zimmer, and V. Ducrot. 2014. Dynamic energy budgets in population ecotoxicology: Applications and outlook. *Ecological Modelling,* 280**:** 140-147. DOI: 10.1016/j.ecolmodel.2013.06.024
Jansen, H. M., S. Van Den Burg, B. Bolman, R. G. Jak, P. Kamermans, M. Poelman, and M. Stuiver. 2016. The feasibility of offshore aquaculture and its potential for multi-use in the North Sea. *Aquaculture International,* 24**:** 735-756. DOI: 10.1007/s10499-016-9987-y
Jansen, J. M., H. Hummel, and S. W. Bonga. 2009. The respiratory capacity of marine mussels (Mytilus galloprovincialis) in relation to the high temperature threshold. *Comp Biochem Physiol A Mol Integr Physiol,* 153**:** 399-402. DOI: 10.1016/j.cbpa.2009.03.013
Keskin, İ., A. Ekici, and S. Serdar. 2020. Determination of the growth performance of Mytilus galloprovincialis in nets at Gökçeada Island. *The European Zoological Journal,* 87**:** 559-570. DOI: 10.1080/24750263.2020.1818856
Kooijman, B., A. Starrlight, M. Kearney, D. Lika, N. Marn, G. Marques, L. Pecquerie, and E. Zimmer. 2022. Add-my-Pet. Retrieved May 14th 2022 2002, from. https://www.bio.vu.nl/thb/deb/deblab/
Kooijman, S. A. L. M. 1986. Energy Budgets Can Explain Body Size Relations. *J. theor. Biol.,* 121**:** 269-282.
Kooijman, S. A. L. M. 2010. *Dynamic energy budget theory for metabolic organisation third edition*. Cambridge: Cambridge University Press.
Kormas, K., V. Garametsi, and A. Nicolaidou. 2002. Size-fractionated phytoplankton chlorophyll in an Eastern Mediterranean coastal system (Maliakos Gulf, Greece). *Helgoland Marine Research,* 56**:** 125-133. DOI: 10.1007/s10152-002-0106-2
Kotta, J., M. Futter, A. Kaasik, K. Liversage, M. Rätsep, F. R. Barboza, L. Bergström, P. Bergström, et al. 2020. Cleaning up seas using blue growth initiatives: Mussel farming for eutrophication control in the Baltic Sea. *Science of The Total Environment,* 709**:** 136144. DOI: 10.1016/j.scitotenv.2019.136144
Kroeker, K. J., B. Gaylord, T. M. Hill, J. D. Hosfelt, S. H. Miller, and E. Sanford. 2014. The role of temperature in determining species' vulnerability to ocean acidification: a case study using Mytilus galloprovincialis. *PLoS One,* 9**:** e100353. DOI: 10.1371/journal.pone.0100353
L., A. D. 2012. Marine Aquaculture in the Mediterranean. In *Encyclopedia of Sustainability Science and Technology,* ed. R. A. Meyers, 529-564. New York: Springer.
Langan, R. 2013. Mussel Culture mussels culture , Open Ocean Innovations. 1229-1239 pp.: Springer New York.
Larsen, P. S., R. Filgueira, and H. U. Riisgård. 2014. Somatic growth of mussels Mytilus edulis in field studies compared to predictions using BEG, DEB, and SFG models. *Journal of Sea Research,* 88**:** 100-108. DOI: 10.1016/j.seares.2014.01.006
Lindahl, O., R. Hart, B. Hernroth, S. Kollberg, L.-O. Loo, L. Olrog, A.-S. Rehnstam-Holm, J. Svensson, et al. 2005. Improving Marine Water Quality by Mussel Farming: A Profitable Solution for Swedish Society. 34**:** 131. DOI: 10.1639/0044-7447(2005)034[0131:imwqbm]2.0.co;2
Lockwood, B. L., and G. N. Somero. 2011. Invasive and native blue mussels (genus Mytilus) on the California coast: The role of physiology in a biological invasion. *Journal of Experimental Marine Biology and Ecology,* 400**:** 167-174. DOI: 10.1016/j.jembe.2011.02.022
Macdonald, B. A., S. M. C. Robinson, and K. A. Barrington. 2011. Feeding activity of mussels (Mytilus edulis) held in the field at an integrated multi-trophic aquaculture (IMTA) site (Salmo salar) and exposed to fish food in the laboratory. *Aquaculture,* 314**:** 244-251. DOI: 10.1016/j.aquaculture.2011.01.045
Macias, D. M., E. Garcia-Gorriz, and A. Stips. 2015. Productivity changes in the Mediterranean Sea for the twenty-first century in response to changes in the regional atmospheric forcing. *Frontiers in Marine Science,* 2. DOI: 10.3389/fmars.2015.00079

Malone, T. C., and M. B. Chervin. 1979. The production and fate of phytoplankton size fractions in the plume of the Hudson River, New York Bight1. *Limnology and Oceanography,* 24**:** 683-696. DOI: 10.4319/lo.1979.24.4.0683

Many, G., C. Ulses, C. Estournel, and P. Marsaleix. 2021. Particulate organic carbon dynamics in the Gulf of Lion shelf (NW Mediterranean) using a coupled hydrodynamic–biogeochemical model. *Biogeosciences,* 18**:** 5513-5538. DOI: 10.5194/bg-18-5513-2021

Mazzola, A., and G. Sarà. 2001. The effect of fish farming organic waste on food availability for bivalve molluscs (Gaeta Gulf, Central Tyrrhenian, MED): stable carbon isotopic analysis. *Aquaculture,* 192**:** 361-379. DOI: 10.1016/s0044-8486(00)00463-4

Microsoft Excel 2204. Microsoft Ireland Operations Limited., Dublin, Ireland.

Notepad Version 21H2. Dublin, Ireland.

Modica, A., D. Scilipoti, R. La Torre, A. Manganaro, and G. Sarà. 2006. The effect of mariculture facilities on biochemical features of suspended organic matter (southern Tyrrhenian, Mediterranean). *Estuarine, Coastal and Shelf Science,* 66**:** 177-184. DOI: 10.1016/j.ecss.2005.08.007

Montalto, V., M. Martinez, A. Rinaldi, G. Sara, and S. Mirto. 2017. The effect of the quality of diet on the functional response of Mytilus galloprovincialis (Lamarck, 1819): Implications for integrated multitrophic aquaculture (IMTA) and marine spatial planning. *Aquaculture,* 468**:** 371-377. DOI: 10.1016/j.aquaculture.2016.10.030

OSPAR, 2009. Assessment of impacts of mariculture. OSPAR Commission Report, London, 64 pp.

Page, H. M., and D. M. Hubbard. 1987. Temporal and spatial patterns of growth in mussels Mytilus edulis on an offshore platform – Relationships to water temperature and food availability. *Journal of Experimental Marine Biology and Ecology,* 111**:** 159-179. DOI: 10.1016/0022-0981(87)90053-0

Palmer, S. C. J., P. M. Gernez, Y. Thomas, S. Simis, P. I. Miller, P. Glize, and L. Barillé. 2020. Remote Sensing-Driven Pacific Oyster (Crassostrea gigas) Growth Modeling to Inform Offshore Aquaculture Site Selection. *Frontiers in Marine Science,* 6. DOI: 10.3389/fmars.2019.00802

Parappurathu, S., N. K. Sanil, P. K. Asokan, S. R. K. Sharma, M. A. Pradeep, S. Padua, S. Gangadharan, G. Mohan, et al. 2021. Green mussel (Perna viridis L.) farming in India: an analysis of major growth milestones, recent decline due to disease incidence, and prospects for revival. *Aquaculture International,* 29**:** 1813-1828. DOI: 10.1007/s10499-021-00716-3

Peharda, M., I. Župan, L. Bavčević, A. Frankić, and T. KlanjšČek. 2007. Growth and condition index of mussel Mytilus galloprovincialis in experimental integrated aquaculture. *Aquaculture Research,* 38**:** 1714-1720. DOI: 10.1111/j.1365-2109.2007.01840.x

Pieters, H., J. H. Kluytmans, W. Zurburg, and D. I. Zandee. 1979. The Influence of Seasonal Changes on Energy Metabolism in Mytilus edulis (L.). I. Growth Rate and Biochemical Composition in relation to Environmental Parameters and Spawning. 285-292 pp.: Elsevier.

Préfecture de la région Provence-Alpes-Côte d'Azur, 2015. Schéma régional de développememnt de l'aquaculture marine Provence-Alpes-Côte d-Azur. Report 35 pp.

Prou, J., and P. Goulletquer. 2002. The French mussel industry: Present Status and Perspectives. *Bull. Aquacul. Assoc. Canada,* 102**:** 17-23.

Ribes, M., R. Coma, and J. Gili. 1999. Seasonal variation of particulate organic carbon, dissolved organic carbon and the contribution of microbial communities to the live particulate organic carbon in a shallow near-bottom ecosystem at the Northwestern Mediterranean Sea. *Journal of Plankton Research,* 21**:** 1077-1100. DOI: 10.1093/plankt/21.6.1077

Rosland, R., Ø. Strand, M. Alunno-Bruscia, C. Bacher, and T. Strohmeier. 2009. Applying Dynamic Energy Budget (DEB) theory to simulate growth and bio-energetics of blue mussels under low seston conditions. *Journal of Sea Research,* 62**:** 49-61. DOI: 10.1016/j.seares.2009.02.007

Rubino, M., 2008. Offshore Aquaculture in the United States: Economic Considerations, Implications & Opportunities. U.S. Department of Commerce Report, Silver Spring, MD; USA, 263 pp.

Rubino, M. 2011. What is aquaculture? Retrieved January 14 2022, from. https://www.noaa.gov/stories/what-is-aquaculture

Sarà, G., M. Kearney, and B. Helmuth. 2011a. Combining heat-transfer and energy budget models to predict thermal stress in Mediterranean intertidal mussels. *Chemistry and Ecology,* 27**:** 135-145. DOI: 10.1080/02757540.2011.552227

Sarà, G., M. Lo Martire, M. Sanfilippo, G. Pulicanò, G. Cortese, A. Mazzola, A. Manganaro, and A. Pusceddu. 2011b. Impacts of marine aquaculture at large spatial scales: Evidences from N and P catchment loading and phytoplankton biomass. *Marine Environmental Research,* 71**:** 317-324. DOI: 10.1016/j.marenvres.2011.02.007

Sarà, G., A. Manganaro, G. Cortese, A. Pusceddu, and A. Mazzola. 1998. The relationship between food availability and growth in Mytilus galloprovincialis in the open sea (southern Mediterranean). *Aquaculture,* 167**:** 1-15. DOI: 10.1016/s0044-8486(98)00281-6

Sarà, G., A. Zenone, and A. Tomasello. 2009. Growth of Mytilus galloprovincialis (mollusca, bivalvia) close to fish farms: a case of integrated multi-trophic aquaculture within the Tyrrhenian Sea. *Hydrobiologia,* 636**:** 129-136. DOI: 10.1007/s10750-009-9942-2

Saraiva, S., M. Van Der M, S. Kooijman, R. Witbaard, C. Philippart, D. Hippler, and R. Parker. 2012. Validation of a Dynamic Energy Budget (DEB) model for the blue mussel Mytilus edulis. *Marine Ecology Progress Series,* 463**:** 141-158. DOI: 10.3354/meps09801

Shaltout, M., and A. Omstedt. 2014. Recent sea surface temperature trends and future scenarios for the Mediterranean Sea. *Oceanologia,* 56**:** 411-443. DOI: 10.5697/oc.56-3.411

Śmietanka, B., A. Burzyński, H. Hummel, and R. Wenne. 2014. Glacial history of the European marine mussels Mytilus, inferred from distribution of mitochondrial DNA lineages. *Heredity,* 113**:** 250-258. DOI: 10.1038/hdy.2014.23

Steffani, C., and G. Branch. 2003. Growth rate, condition, and shell shape of Mytilus galloprovincialis: responses to wave exposure. *Marine Ecology Progress Series,* 246**:** 197-209. DOI: 10.3354/meps246197

Tamburini, E., E. Turolla, E. A. Fano, and G. Castaldelli. 2020. Sustainability of Mussel (Mytilus Galloprovincialis) Farming in the Po River Delta, Northern Italy, Based on a Life Cycle Assessment Approach. *Sustainability,* 12**:** 3814. DOI: 10.3390/su12093814

Tammi, I., and R. Kalliola. 2014. Spatial MCDA in marine planning: Experiences from the Mediterranean and Baltic Seas. *Marine Policy,* 48**:** 73-83. DOI: 10.1016/j.marpol.2014.03.015

Troell, M., A. Joyce, T. Chopin, A. Neori, A. H. Buschmann, and J.-G. Fang. 2009. Ecological engineering in aquaculture — Potential for integrated multi-trophic aquaculture (IMTA) in marine offshore systems. *Aquaculture,* 297**:** 1-9. DOI: 10.1016/j.aquaculture.2009.09.010

Troost, T. A., J. W. Wijsman, S. Saraiva, and V. Freitas. 2010. Modelling shellfish growth with dynamic energy budget models: an application for cockles and mussels in the Oosterschelde (southwest Netherlands). *Philos Trans R Soc Lond B Biol Sci,* 365**:** 3567-3577. DOI: 10.1098/rstb.2010.0074

United Nations' Department of Economic and Social Affairs Population Division, 2019. World Population Prospects 2019: Highlights (ST/ESA/SER.A/423). United Nations Report.

Van der Veer, H. W., J. F. M. F. Cardoso, and J. van der Meer. 2006. The estimation of DEB parameters for various Northeast Atlantic bivalve species. *Journal of Sea Research,* 56**:** 107-124. DOI: 10.1016/j.seares.2006.03.005

Van Haren, R. J. F., and S. A. L. M. Kooijman. 1993. Application of a dynamic energy budget model to Mytilus edulis (L.). *Netherlands Journal of Sea Research,* 31**:** 119-133. DOI: 10.1016/0077-7579(93)90002-a

Willer, D., and D. C. Aldridge. 2017. Microencapsulated diets to improve bivalve shellfish aquaculture. *Royal Society Open Science,* 4**:** 171142. DOI: 10.1098/rsos.171142

World Bank Data. 2017. CO2 Emissions.

Zaldívar, J.-M., 2008. A general bioaccumulation DEB model for mussels. The Institute for Health and Consumer Protection at the European Union Joint Research Centre Report, Luxembourg.

Appendix A: Figures

Table A 1 : DEB-model constants.

Constants	**Symbol**	**Unit**	**Value**	**Source**
Maximum surface-area specific assimilation rate	$\dot{p}_{Am}$	J/d cm^2	147.6	Van der Veer et al. (2006)
Half saturation coefficient	X_k	MgC/m^3	194 Calib.	Casas and Bacher (2006) Present study
Arrhenius temperature	T_A	K	5800	Van der Veer et al. (2006)
Reference temperature	T_I	K	293	Van der Veer et al. (2006)
Lower boundary of tolerance range	T_L	K	275	Van der Veer et al. (2006)
Upper boundary of tolerance range	T_H	K	296	Van der Veer et al. (2006)
Arrhenius temperature for the rate of decrease at the lower boundary	T_{AL}	K	45430	Van der Veer et al. (2006)
Arrhenius temperature for the rate of decrease at the upper boundary	T_{AH}	K	31376	Van der Veer et al. (2006)
Fraction of utilized energy spent on maintenance/growth	κ	-	0.7	Van der Veer et al. (2006)
Volume specific costs of growth	$[E_G]$	J/cm^3	1900	Van der Veer et al. (2006)
Maximum energy density	$[E_M]$	J/cm^3	2190	Van der Veer et al. (2006)
Volume specific maintenance costs	$[\dot{p}_M]_m$	J/d cm^3	24	Van der Veer et al. (2006)
Specific density	d	g/cm^3	1	Kooijman (2010)
Minimum reproductive volume	V_p	cm^3	0.060	Van der Veer et al. (2006)
Energy content of reserves	μ_E	J/g	6750	Casas and Bacher (2006)
Shape coefficient	δ_m	N/A	0.250	Casas and Bacher (2006)
Conversion factor from chl *a* to X	X:chl *a*	N/A	50	Hatzonikolakis et al. (2017)

Table A 2 : DEB-model variables (Hatzonikolakis et al. 2017).

Variable	**Description**	**Unit**
V	Structural volume	cm^3
E	Energy reserves	J
R	Energy allocated to development and reproduction	J
$\dot{p}_a$	Assimilation energy rate	J / d
$\dot{p}_c$	Energy utilization rate	J / d
F	Functional response function	-
X	Food density	mg C / m^3
$[\dot{p}_M]$	Maintenance costs	J / cm^3 d
T	Temperature	K
k(T)	Temperature dependence	-
L	Shell length	cm
W	Fresh tissue mass	g

Table A 3 : DEB method equations (Hatzonikolakis et al. 2017).

$$\frac{dE}{dt} = \dot{p}_a - \dot{p}_c \quad \text{(a)}$$

$$\frac{dV}{dt} = \frac{\kappa * \dot{p}_c - [\dot{p}_M] * V}{E_G} \quad \text{(b)}$$

$$\frac{dR}{dt} = (1-\kappa) * \dot{p}_c - \left[\frac{1-\kappa}{\kappa}\right] * V_p * [\dot{p}_M] \quad \text{(c)}$$

$$\dot{p}_a = \dot{p}_{Am} * f * k(T) * V^{2/3} \quad \text{(d)}$$

$$f = \frac{X}{X + X_k} \quad \text{(e)}$$

$$\dot{p}_c = \frac{[E]}{[E_G] + \kappa * [E]} * \left(\frac{[E_G] * \dot{p}_{Am} * k(T) * V^{2/3}}{[E_m]} + [\dot{p}_M] * V\right) \quad \text{(f)}$$

$$[E] = \frac{E}{V} \quad \text{(g)}$$

$$[\dot{p}_M] = k(T) * [\dot{p}_M]_m \quad \text{(h)}$$

$$k(T) = \frac{\exp\left(\frac{T_A}{T_I} - \frac{T_A}{T}\right)}{1 + \exp\left(\frac{T_{AL}}{T} - \frac{T_{AL}}{T_L}\right) + \exp\left(\frac{T_{AH}}{T_H} - \frac{T_{AH}}{T}\right)} \quad \text{(i)}$$

$$L = \frac{V^{1/3}}{\delta_m} \quad \text{(j)}$$

$$W = d * \left(V + \frac{E}{E_G}\right) + \frac{R}{\mu_E} \quad \text{(k)}$$

$$E = \frac{V}{cm^3} * 300 * 0.7\ J \quad \text{(l)}$$

$$R = \frac{V}{cm^3} * 300 * 0.3\ J \quad \text{(m)}$$

Series from Lund University

Department of Physical Geography and Ecosystem Science

Master Thesis in Geographical Information Science

1. *Anthony Lawther:* The application of GIS-based binary logistic regression for slope failure susceptibility mapping in the Western Grampian Mountains, Scotland (2008).

2. *Rickard Hansen:* Daily mobility in Grenoble Metropolitan Region, France. Applied GIS methods in time geographical research (2008).

3. *Emil Bayramov:* Environmental monitoring of bio-restoration activities using GIS and Remote Sensing (2009).

4. *Rafael Villarreal Pacheco:* Applications of Geographic Information Systems as an analytical and visualization tool for mass real estate valuation: a case study of Fontibon District, Bogota, Columbia (2009).

5. *Siri Oestreich Waage:* a case study of route solving for oversized transport: The use of GIS functionalities in transport of transformers, as part of maintaining a reliable power infrastructure (2010).

6. *Edgar Pimiento:* Shallow landslide susceptibility – Modelling and validation (2010).

7. *Martina Schäfer:* Near real-time mapping of floodwater mosquito breeding sites using aerial photographs (2010).

8. *August Pieter van Waarden-Nagel:* Land use evaluation to assess the outcome of the programme of rehabilitation measures for the river Rhine in the Netherlands (2010).

9. *Samira Muhammad:* Development and implementation of air quality data mart for Ontario, Canada: A case study of air quality in Ontario using OLAP tool. (2010).

10. *Fredros Oketch Okumu*: Using remotely sensed data to explore spatial and temporal relationships between photosynthetic productivity of vegetation and malaria transmission intensities in selected parts of Africa (2011).

11. *Svajunas Plunge:* Advanced decision support methods for solving diffuse water pollution problems (2011).

12. *Jonathan Higgins:* Monitoring urban growth in greater Lagos: A case study using GIS to monitor the urban growth of Lagos 1990 - 2008 and produce future growth prospects for the city (2011).

13. *Mårten Karlberg:* Mobile Map Client API: Design and Implementation for Android (2011).

14. *Jeanette McBride:* Mapping Chicago area urban tree canopy using color infrared imagery (2011).

15. *Andrew Farina:* Exploring the relationship between land surface temperature and vegetation abundance for urban heat island mitigation in Seville, Spain (2011).

16. *David Kanyari*: Nairobi City Journey Planner: An online and a Mobile Application (2011).

17. *Laura V. Drews:* Multi-criteria GIS analysis for siting of small wind power plants - A case study from Berlin (2012).

18. *Qaisar Nadeem:* Best living neighborhood in the city - A GIS based multi criteria evaluation of ArRiyadh City (2012).

19. *Ahmed Mohamed El Saeid Mustafa:* Development of a photo voltaic building rooftop integration analysis tool for GIS for Dokki District, Cairo, Egypt (2012).

20. *Daniel Patrick Taylor*: Eastern Oyster Aquaculture: Estuarine Remediation via Site Suitability and Spatially Explicit Carrying Capacity Modeling in Virginia's Chesapeake Bay (2013).

21. *Angeleta Oveta Wilson:* A Participatory GIS approach to *unearthing* Manchester's Cultural Heritage '*gold mine'* (2013).

22. *Ola Svensson:* Visibility and Tholos Tombs in the Messenian Landscape: A Comparative Case Study of the Pylian Hinterlands and the Soulima Valley (2013).

23. *Monika Ogden:* Land use impact on water quality in two river systems in South Africa (2013).

24. *Stefan Rova:* A GIS based approach assessing phosphorus load impact on Lake Flaten in Salem, Sweden (2013).

25. *Yann Buhot:* Analysis of the history of landscape changes over a period of 200 years. How can we predict past landscape pattern scenario and the impact on habitat diversity? (2013).

26. *Christina Fotiou:* Evaluating habitat suitability and spectral heterogeneity models to predict weed species presence (2014).

27. *Inese Linuza:* Accuracy Assessment in Glacier Change Analysis (2014).

28. *Agnieszka Griffin:* Domestic energy consumption and social living standards: a GIS analysis within the Greater London Authority area (2014).

29. *Brynja Guðmundsdóttir:* Detection of potential arable land with remote sensing and GIS - A Case Study for Kjósarhreppur (2014).

30. *Oleksandr Nekrasov:* Processing of MODIS Vegetation Indices for analysis of agricultural droughts in the southern Ukraine between the years 2000-2012 (2014).

31. *Sarah Tressel:* Recommendations for a polar Earth science portal in the context of Arctic Spatial Data Infrastructure (2014).

32. *Caroline Gevaert:* Combining Hyperspectral UAV and Multispectral Formosat-2 Imagery for Precision Agriculture Applications (2014).

33. *Salem Jamal-Uddeen:* Using GeoTools to implement the multi-criteria evaluation analysis - weighted linear combination model (2014).

34. *Samanah Seyedi-Shandiz:* Schematic representation of geographical railway network at the Swedish Transport Administration (2014).

35. *Kazi Masel Ullah:* Urban Land-use planning using Geographical Information System and analytical hierarchy process: case study Dhaka City (2014).

36. *Alexia Chang-Wailing Spitteler:* Development of a web application based on MCDA and GIS for the decision support of river and floodplain rehabilitation projects (2014).

37. *Alessandro De Martino:* Geographic accessibility analysis and evaluation of potential changes to the public transportation system in the City of Milan (2014).

38. *Alireza Mollasalehi:* GIS Based Modelling for Fuel Reduction Using Controlled Burn in Australia. Case Study: Logan City, QLD (2015).

39. *Negin A. Sanati:* Chronic Kidney Disease Mortality in Costa Rica; Geographical Distribution, Spatial Analysis and Non-traditional Risk Factors (2015).

40. *Karen McIntyre:* Benthic mapping of the Bluefields Bay fish sanctuary, Jamaica (2015).

41. *Kees van Duijvendijk:* Feasibility of a low-cost weather sensor network for agricultural purposes: A preliminary assessment (2015).

42. *Sebastian Andersson Hylander:* Evaluation of cultural ecosystem services using GIS (2015).

43. *Deborah Bowyer:* Measuring Urban Growth, Urban Form and Accessibility as Indicators of Urban Sprawl in Hamilton, New Zealand (2015).

44. *Stefan Arvidsson:* Relationship between tree species composition and phenology extracted from satellite data in Swedish forests (2015).

45. *Damián Giménez Cruz*: GIS-based optimal localisation of beekeeping in rural Kenya (2016).

46. *Alejandra Narváez Vallejo:* Can the introduction of the topographic indices in LPJ-GUESS improve the spatial representation of environmental variables? (2016).

47. *Anna Lundgren:* Development of a method for mapping the highest coastline in Sweden using breaklines extracted from high resolution digital elevation models (2016).

48. *Oluwatomi Esther Adejoro:* Does location also matter? A spatial analysis of social achievements of young South Australians (2016).

49. *Hristo Dobrev Tomov:* Automated temporal NDVI analysis over the Middle East for the period 1982 - 2010 (2016).

50. *Vincent Muller:* Impact of Security Context on Mobile Clinic Activities A GIS Multi Criteria Evaluation based on an MSF Humanitarian Mission in Cameroon (2016).

51. *Gezahagn Negash Seboka:* Spatial Assessment of NDVI as an Indicator of Desertification in Ethiopia using Remote Sensing and GIS (2016).

52. *Holly Buhler:* Evaluation of Interfacility Medical Transport Journey Times in Southeastern British Columbia. (2016).

53. *Lars Ole Grottenberg*: Assessing the ability to share spatial data between emergency management organisations in the High North (2016).

54. *Sean Grant:* The Right Tree in the Right Place: Using GIS to Maximize the Net Benefits from Urban Forests (2016).

55. *Irshad Jamal:* Multi-Criteria GIS Analysis for School Site Selection in Gorno-Badakhshan Autonomous Oblast, Tajikistan (2016).

56. *Fulgencio Sanmartín:* Wisdom-volkano: A novel tool based on open GIS and time-series visualization to analyse and share volcanic data (2016).

57. *Nezha Acil:* Remote sensing-based monitoring of snow cover dynamics and its influence on vegetation growth in the Middle Atlas Mountains (2016).

58. *Julia Hjalmarsson:* A Weighty Issue: Estimation of Fire Size with Geographically Weighted Logistic Regression (2016).

59. *Mathewos Tamiru Amato:* Using multi-criteria evaluation and GIS for chronic food and nutrition insecurity indicators analysis in Ethiopia (2016).

60. *Karim Alaa El Din Mohamed Soliman El Attar:* Bicycling Suitability in Downtown, Cairo, Egypt (2016).

61. *Gilbert Akol Echelai:* Asset Management: Integrating GIS as a Decision Support Tool in Meter Management in National Water and Sewerage Corporation (2016).

62. *Terje Slinning:* Analytic comparison of multibeam echo soundings (2016).

63. *Gréta Hlín Sveinsdóttir:* GIS-based MCDA for decision support: A framework for wind farm siting in Iceland (2017).

64. *Jonas Sjögren:* Consequences of a flood in Kristianstad, Sweden: A GIS-based analysis of impacts on important societal functions (2017).

65. *Nadine Raska:* 3D geologic subsurface modelling within the Mackenzie Plain, Northwest Territories, Canada (2017).

66. *Panagiotis Symeonidis*: Study of spatial and temporal variation of atmospheric optical parameters and their relation with PM 2.5 concentration over Europe using GIS technologies (2017).

67. *Michaela Bobeck:* A GIS-based Multi-Criteria Decision Analysis of Wind Farm Site Suitability in New South Wales, Australia, from a Sustainable Development Perspective (2017).

68. *Raghdaa Eissa*: Developing a GIS Model for the Assessment of Outdoor Recreational Facilities in New Cities Case Study: Tenth of Ramadan City, Egypt (2017).

69. *Zahra Khais Shahid*: Biofuel plantations and isoprene emissions in Svea and Götaland (2017).

70. *Mirza Amir Liaquat Baig*: Using geographical information systems in epidemiology: Mapping and analyzing occurrence of diarrhea in urban - residential area of Islamabad, Pakistan (2017).

71. *Joakim Jörwall*: Quantitative model of Present and Future well-being in the EU-28: A spatial Multi-Criteria Evaluation of socioeconomic and climatic comfort factors (2017).

72. *Elin Haettner*: Energy Poverty in the Dublin Region: Modelling Geographies of Risk (2017).

73. *Harry Eriksson*: Geochemistry of stream plants and its statistical relations to soil- and bedrock geology, slope directions and till geochemistry. A GIS-analysis of small catchments in northern Sweden (2017).

74. *Daniel Gardevärn:* PPGIS and Public meetings – An evaluation of public participation methods for urban planning (2017).

75. *Kim Friberg:* Sensitivity Analysis and Calibration of Multi Energy Balance Land Surface Model Parameters (2017).

76. *Viktor Svanerud:* Taking the bus to the park? A study of accessibility to green areas in Gothenburg through different modes of transport (2017).

77. *Lisa-Gaye Greene*: Deadly Designs: The Impact of Road Design on Road Crash Patterns along Jamaica's North Coast Highway (2017).

78. *Katarina Jemec Parker*: Spatial and temporal analysis of fecal indicator bacteria concentrations in beach water in San Diego, California (2017).

79. *Angela Kabiru*: An Exploratory Study of Middle Stone Age and Later Stone Age Site Locations in Kenya's Central Rift Valley Using Landscape Analysis: A GIS Approach (2017).

80. *Kristean Björkmann*: Subjective Well-Being and Environment: A GIS-Based Analysis (2018).

81. *Williams Erhunmonmen Ojo*: Measuring spatial accessibility to healthcare for people living with HIV-AIDS in southern Nigeria (2018).

82. *Daniel Assefa*: Developing Data Extraction and Dynamic Data Visualization (Styling) Modules for Web GIS Risk Assessment System (WGRAS). (2018).

83. *Adela Nistora*: Inundation scenarios in a changing climate: assessing potential impacts of sea-level rise on the coast of South-East England (2018).

84. *Marc Seliger*: Thirsty landscapes - Investigating growing irrigation water consumption and potential conservation measures within Utah's largest master-planned community: Daybreak (2018).

85. *Luka Jovičić*: Spatial Data Harmonisation in Regional Context in Accordance with INSPIRE Implementing Rules (2018).

86. *Christina Kourdounouli*: Analysis of Urban Ecosystem Condition Indicators for the Large Urban Zones and City Cores in EU (2018).

87. *Jeremy Azzopardi*: Effect of distance measures and feature representations on distance-based accessibility measures (2018).

88. *Patrick Kabatha*: An open source web GIS tool for analysis and visualization of elephant GPS telemetry data, alongside environmental and anthropogenic variables (2018).

89. *Richard Alphonce Giliba*: Effects of Climate Change on Potential Geographical Distribution of Prunus africana (African cherry) in the Eastern Arc Mountain Forests of Tanzania (2018).

90. *Eiður Kristinn Eiðsson*: Transformation and linking of authoritative multi-scale geodata for the Semantic Web: A case study of Swedish national building data sets (2018).

91. *Niamh Harty*: HOP!: a PGIS and citizen science approach to monitoring the condition of upland paths (2018).

92. *José Estuardo Jara Alvear*: Solar photovoltaic potential to complement hydropower in Ecuador: A GIS-based framework of analysis (2018).

93. *Brendan O'Neill*: Multicriteria Site Suitability for Algal Biofuel Production Facilities (2018).

94. *Roman Spataru*: Spatial-temporal GIS analysis in public health – a case study of polio disease (2018).

95. *Alicja Miodońska*: Assessing evolution of ice caps in Suðurland, Iceland, in years 1986 - 2014, using multispectral satellite imagery (2019).

96. *Dennis Lindell Schettini*: A Spatial Analysis of Homicide Crime's Distribution and Association with Deprivation in Stockholm Between 2010-2017 (2019).

97. *Damiano Vesentini*: The Po Delta Biosphere Reserve: Management challenges and priorities deriving from anthropogenic pressure and sea level rise (2019).

98. *Emilie Arnesten*: Impacts of future sea level rise and high water on roads, railways and environmental objects: a GIS analysis of the potential effects of increasing sea levels and highest projected high water in Scania, Sweden (2019).

99. *Syed Muhammad Amir Raza*: Comparison of geospatial support in RDF stores: Evaluation for ICOS Carbon Portal metadata (2019).

100. *Hemin Tofiq*: Investigating the accuracy of Digital Elevation Models from UAV images in areas with low contrast: A sandy beach as a case study (2019).

101. *Evangelos Vafeiadis*: Exploring the distribution of accessibility by public transport using spatial analysis. A case study for retail concentrations and public hospitals in Athens (2019).

102. *Milan Sekulic*: Multi-Criteria GIS modelling for optimal alignment of roadway by-passes in the Tlokweng Planning Area, Botswana (2019).

103. *Ingrid Piirisaar*: A multi-criteria GIS analysis for siting of utility-scale photovoltaic solar plants in county Kilkenny, Ireland (2019).

104. *Nigel Fox*: Plant phenology and climate change: possible effect on the onset of various wild plant species' first flowering day in the UK (2019).

105. *Gunnar Hesch*: Linking conflict events and cropland development in Afghanistan, 2001 to 2011, using MODIS land cover data and Uppsala Conflict Data Programme (2019).

106. *Elijah Njoku*: Analysis of spatial-temporal pattern of Land Surface Temperature (LST) due to NDVI and elevation in Ilorin, Nigeria (2019).

107. *Katalin Bunyevácz*: Development of a GIS methodology to evaluate informal urban green areas for inclusion in a community governance program (2019).

108. *Paul dos Santos*: Automating synthetic trip data generation for an agent-based simulation of urban mobility (2019).

109. *Robert O' Dwyer*: Land cover changes in Southern Sweden from the mid-Holocene to present day: Insights for ecosystem service assessments (2019).

110. *Daniel Klingmyr*: Global scale patterns and trends in tropospheric NO2 concentrations (2019).

111. *Marwa Farouk Elkabbany*: Sea Level Rise Vulnerability Assessment for Abu Dhabi, United Arab Emirates (2019).

112. *Jip Jan van Zoonen*: Aspects of Error Quantification and Evaluation in Digital Elevation Models for Glacier Surfaces (2020).

113. *Georgios Efthymiou*: The use of bicycles in a mid-sized city – benefits and obstacles identified using a questionnaire and GIS (2020).

114. *Haruna Olayiwola Jimoh*: Assessment of Urban Sprawl in MOWE/IBAFO Axis of Ogun State using GIS Capabilities (2020).

115. *Nikolaos Barmpas Zachariadis*: Development of an iOS, Augmented Reality for disaster management (2020).

116. *Ida Storm*: ICOS Atmospheric Stations: Spatial Characterization of CO2 Footprint Areas and Evaluating the Uncertainties of Modelled CO2 Concentrations (2020).

117. *Alon Zuta*: Evaluation of water stress mapping methods in vineyards using airborne thermal imaging (2020).

118. *Marcus Eriksson*: Evaluating structural landscape development in the municipality Upplands-Bro, using landscape metrics indices (2020).

119. *Ane Rahbek Vierø*: Connectivity for Cyclists? A Network Analysis of Copenhagen's Bike Lanes (2020).

120. *Cecilia Baggini*: Changes in habitat suitability for three declining Anatidae species in saltmarshes on the Mersey estuary, North-West England (2020).

121. *Bakrad Balabanian*: Transportation and Its Effect on Student Performance (2020).

122. *Ali Al Farid*: Knowledge and Data Driven Approaches for Hydrocarbon Microseepage Characterizations: An Application of Satellite Remote Sensing (2020).

123. *Bartlomiej Kolodziejczyk*: Distribution Modelling of Gene Drive-Modified Mosquitoes and Their Effects on Wild Populations (2020).

124. *Alexis Cazorla*: Decreasing organic nitrogen concentrations in European water bodies - links to organic carbon trends and land cover (2020).

125. *Kharid Mwakoba*: Remote sensing analysis of land cover/use conditions of community-based wildlife conservation areas in Tanzania (2021).

126. *Chinatsu Endo*: Remote Sensing Based Pre-Season Yellow Rust Early Warning in Oromia, Ethiopia (2021).

127. *Berit Mohr*: Using remote sensing and land abandonment as a proxy for long-term human out-migration. A Case Study: Al-Hassakeh Governorate, Syria (2021).

128. *Kanchana Nirmali Bandaranayake*: Considering future precipitation in delineation locations for water storage systems - Case study Sri Lanka (2021).

129. *Emma Bylund*: Dynamics of net primary production and food availability in the aftermath of the 2004 and 2007 desert locust outbreaks in Niger and Yemen (2021).

130. *Shawn Pace*: Urban infrastructure inundation risk from permanent sea-level rise scenarios in London (UK), Bangkok (Thailand) and Mumbai (India): A comparative analysis (2021).

131. *Oskar Evert Johansson*: The hydrodynamic impacts of Estuarine Oyster reefs, and the application of drone technology to this study (2021).

132. *Pritam Kumarsingh*: A Case Study to develop and test GIS/SDSS methods to assess the production capacity of a Cocoa Site in Trinidad and Tobago (2021).

133. *Muhammad Imran Khan*: Property Tax Mapping and Assessment using GIS (2021).

134. *Domna Kanari*: Mining geosocial data from Flickr to explore tourism patterns: The case study of Athens (2021).

135. Mona Tykesson Klubien: Livestock-MRSA in Danish pig farms (2021).

136. *Ove Njøten*: Comparing radar satellites. Use of Sentinel-1 leads to an increase in oil spill alerts in Norwegian waters (2021).

137. *Panagiotis Patrinos*: Change of heating fuel consumption patterns produced by the economic crisis in Greece (2021).

138. *Lukasz Langowski*: Assessing the suitability of using Sentinel-1A SAR multi-temporal imagery to detect fallow periods between rice crops (2021).

139. *Jonas Tillman*: Perception accuracy and user acceptance of legend designs for opacity data mapping in GIS (2022).

140. *Gabriela Olekszyk*: ALS (Airborne LIDAR) accuracy: Can potential low data quality of ground points be modelled/detected? Case study of 2016 LIDAR capture over Auckland, New Zealand (2022).

141. *Luke Aspland*: Weights of Evidence Predictive Modelling in Archaeology (2022).

142. *Luís Fareleira Gomes*: The influence of climate, population density, tree species and land cover on fire pattern in mainland Portugal (2022).

143. *Andreas Eriksson*: Mapping Fire Salamander (Salamandra salamandra) Habitat Suitability in Baden-Württemberg with Multi-Temporal Sentinel-1 and Sentinel-2 Imagery (2022).

144. *Lisbet Hougaard Baklid*: Geographical expansion rate of a brown bear population in Fennoscandia and the factors explaining the directional variations (2022).

145. *Victoria Persson*: Mussels in deep water with climate change: Spatial distribution of mussel (Mytilus galloprovincialis) growth offshore in the French Mediterranean with respect to climate change scenario RCP 8.5 Long Term and Integrated Multi-Trophic Aquaculture (IMTA) using Dynamic Energy Budget (DEB) modelling (2022).